Bradley R. Johnson
115 Words

MAXIPOL: A Bolometric, Balloon-Borne Experiment for Measuring the Polarization Anisotropy of the Cosmic Microwave Background Radiation

We discuss MAXIPOL, a bolometric balloon-borne experiment designed to measure the E-mode polarization anisotropy of the cosmic microwave background radiation (CMB) on angular scales of $10'$ to 2°. MAXIPOL is the first CMB experiment to collect data with a polarimeter that utilizes a rotating half-wave plate and fixed wire-grid polarizer. We present the instrument design, elaborate on the polarimeter strategy and show data products including preliminary T, Q and U maps. Our primary data set was collected during a 26 hour turnaround flight that was launched from the National Scientific Ballooning Facility in Ft. Sumner, New Mexico in May 2003. During this flight five regions of the sky were mapped. Data analysis is in progress.

UNIVERSITY OF MINNESOTA

This is to certify that I have examined this bound copy of a doctoral thesis by

Bradley R. Johnson

and have found that it is complete and satisfactory in all respects and that any and all revisions required by the final examining committee have been made.

Professor Shaul Hanany
(Faculty Adviser)

GRADUATE SCHOOL

MAXIPOL: A Bolometric, Balloon-Borne Experiment for Measuring the Polarization Anisotropy of the Cosmic Microwave Background Radiation

A THESIS
SUBMITTED TO THE FACULTY OF THE GRADUATE SCHOOL
OF THE UNIVERSITY OF MINNESOTA
BY

Bradley R. Johnson

IN PARTIAL FULFILLMENT OF THE REQUIREMENTS
FOR THE DEGREE OF
DOCTOR OF PHILOSOPHY

August, 2004

MAXIPOL: A Bolometric, Balloon-Borne Experiment for Measuring the Polarization Anisotropy of the Cosmic Microwave Background Radiation

by Bradley R. Johnson
Under the supervision of Professor Shaul Hanany

ABSTRACT

We discuss MAXIPOL, a bolometric balloon-borne experiment designed to measure the E-mode polarization anisotropy of the cosmic microwave background radiation (CMB) on angular scales of $10'$ to $2°$. MAXIPOL is the first CMB experiment to collect data with a polarimeter that utilizes a rotating half-wave plate and fixed wire-grid polarizer. We present the instrument design, elaborate on the polarimeter strategy and show data products including preliminary T, Q and U maps. Our primary data set was collected during a 26 hour turnaround flight that was launched from the National Scientific Ballooning Facility in Ft. Sumner, New Mexico in May 2003. During this flight five regions of the sky were mapped. Data analysis is in progress.

Acknowledgements

First and foremost, I would like to thank my advisor, Shaul Hanany, for his steadfast dedication to my education and his tenacious spirit that taught me scientific pioneering can only be successful through professionalism, unwavering perseverance and hours of hard work. This thesis is the culmination of years of learning that would not have been possible without the numerous experiences and opportunities that Professor Hanany provided for me.

MAXIPOL started as a naive polarimetric experiment that diverged quickly after inception into a wonderfully complex and trying experience. I would like to thank the core experimental team, namely Huan Tran and Jeff Collins, for battling through broken transmitters, squeaky bearings and two balloon launches over three seasons in Ft. Sumner, New Mexico with me. I would also like to thank my counterpart at the University of Minnesota, Matthew Abroe, for all of the computer science and social science assistance.

My research would not have been possible without the Richards group at the University of California, Berkeley. I would be remiss if I did not thank Celeste Winant for bequeathing her knowledge base of bolometers and cryogenics to me, Paul Richards for always being the wise and distinguished scientist and Adrian Lee for acting as my surrogate advisor from time to time.

I would also like to thank NASA for the GSRP Fellowship and the tireless efforts of Danny Ball, Bill Stepp, Frank Candelaria, Mark Cobble, Robert Salter and the other members of the NSBF that helped make MAXIPOL a success.

On a personal level, I would like to thank my parents, Richard and Barbara Johnson, for their support through twenty-five consecutive years of schooling, and finally I would like to thank Jessica Kimpell for teaching me to enjoy working hard. This lesson came at a critical time for me during my graduate school career and I know whatever success I am enjoying today comes as a direct result of her wisdom.

The full MAXIPOL collaboration is listed in Appendix C.

Dedication

To Chaos, the most ancient Greek goddess of emptiness and confusion who gave birth to the universe.

Table of Contents

List of Tables

List of Figures

Chapter 1

Polarization of the Cosmic Microwave Background

1.1 Introduction

Recent measurements of the spatial temperature anisotropy of the cosmic microwave background radiation (CMB) suggest that the ΛCDM cosmological model accurately describes the evolution of our universe (Figure 1.1). Assuming this model, a distinct spatial polarization pattern should appear across the sky in the CMB arising from physical mechanisms that operated in the early universe [1]. This Ph.D. thesis is centered on MAXIPOL, a bolometric, balloon-borne experiment designed to detect the curl-free component of the CMB polarization field on angular scales of $10'$ to $2°$; polarimetric observations were made near the peak of the 2.7 K blackbody spectrum at 140 GHz [2]. To date two of MAXIPOL's contemporaries, DASI and WMAP, have detected polarization in the CMB at frequencies between 23 and 94 GHz with HEMT based observations made from the South Pole and the Earth-Sun L2 Lagrange point, respectively. The MAXIPOL observations complement DASI and WMAP in polarimeter technology and frequency coverage. In all cases, state-of-the-art receivers are sensitive enough to simply detect the small partially polarized signal – not fully characterize it. A precise characterization of the CMB polarization anisotropy will provide the energy scale of inflation or meaningful limits thereof and the values of a collection of cosmological parameters. MAXIPOL represents a first step toward this scientific end acting as a pioneering experiment and a test bed for millimeter-wave polarimeter technologies that may be used by the next generation of experiments aiming to fully characterize the anticipated polarized signals.

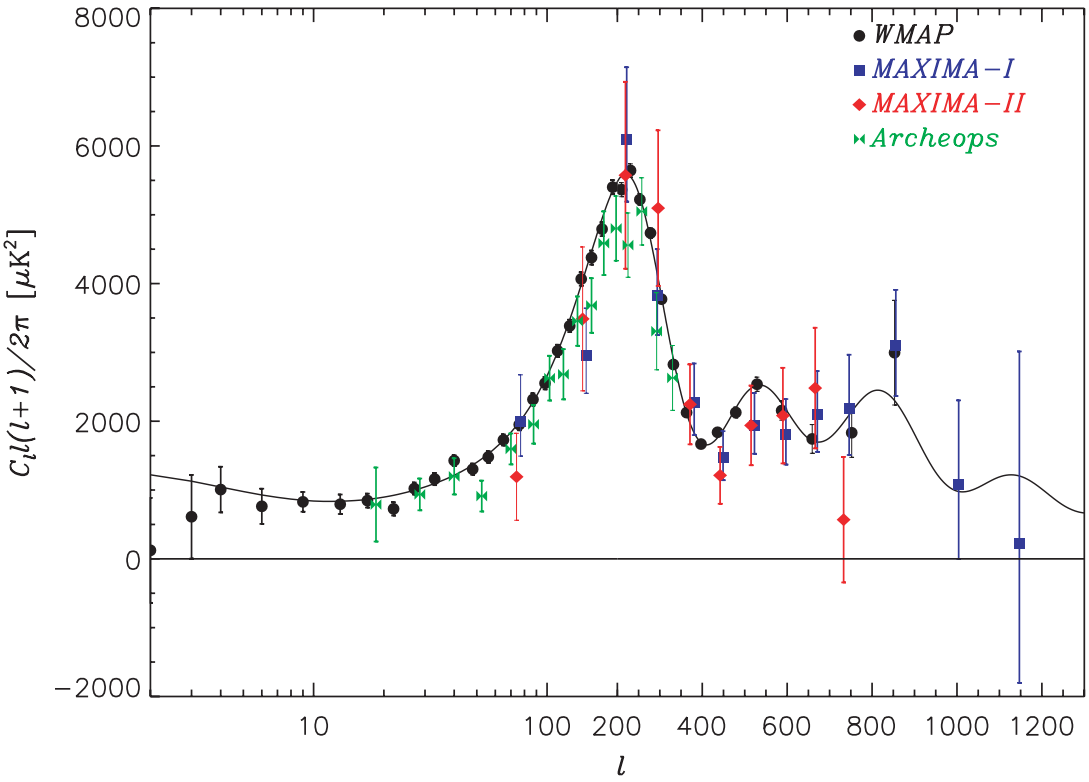

Figure 1.1: Measurements of the temperature anisotropy of the CMB. The colored points represent measurements associated with the Observational Cosmology Group at the University of Minnesota made by the MAXIMA and Archeops experiments [4, 6, 7]. The black points and curve are the WMAP measurements and best fit ΛCDM cosmological model, respectively [8]. These WMAP measurements suggest $\Omega_b = 0.044$, $\Omega_m = 0.27$, $\Omega_\Lambda = 0.73$ and $\Omega_{tot} = 1$. Note the hybrid x-axis used to elucidate the low ℓ and high ℓ measurements on the same plot [9].

CMB polarization science is reviewed in Chapter 1. The details of the MAXIPOL instrument are discussed in Chapter 2 with polarimeter specifics in Chapter 3. A record of MAXIPOL observations is presented in Chapter 4, while subsequent data analysis details are outlined in Chapter 5. Future work centered on the B-mode instrument design that the author will undertake as a PPARC and NSF IRFP Fellow at the University of Wales, Cardiff is covered in Chapter 6.

1.2 Scientific Motivation

When the universe was ∼380,000 years old, the ambient photon-baryon plasma that emerged from the Big Bang had cooled because of expansion to the point where free protons and electrons recombined to form neutral hydrogen. Photons that were once tightly coupled to the free baryons were

left to stream freely through the universe; photons originating from the surface of last scattering are observed today across the sky as the CMB. These CMB photons carried with them information about physical processes that operated in the cosmological fluid at the time of recombination. As a result, these primordial particles are an invaluable resource that can be used to study the early universe.

Over the past decade, many experiments have successfully mapped the spatial temperature anisotropy of the CMB (MAXIMA for example [3, 4, 5, 6], WMAP for state-of-the-art [8]). These measurements suggest that we live in a universe whose evolution is described by adiabatic inflationary cosmology dominated by cold dark matter and a cosmological constant. Given this fact, the CMB should be partially linearly polarized with the vector field on the sky consisting of a curl-free (E-mode) component and a divergence-free (B-mode) component. These separable constituents were produced by the same physical mechanism – Thomson scattering – but distinctly different processes in the early universe. The E-mode component was predominantly produced by bulk motion in the primordial plasma, which was driven by baryons gravitationally falling into the dark matter potential wells that were setup by scalar perturbations; the B-mode component was produced by tensor perturbations arising from gravity waves generated during inflation.

To date, the E-mode polarization anisotropy has been detected by DASI [10] but not fully characterized, the temperature-E-mode cross-correlation (TE) has been measured by WMAP [11] and the anticipated B-mode polarization anisotropy signal remains undetected – and lies at our technological horizon. The E-mode and B-mode signals are elusive because they are faint. The E-mode polarization anisotropy was detected on the order of one part in 10^6 – a factor of $\sim$10 below the temperature anisotropy signal [10]. The primordial B-mode signal is predicted to be a factor of $\sim$10 or more below the E-mode signal.

The blackbody temperature of the CMB is highly isotropic across the entire sky with primordial anisotropy appearing at the level of one part in 10^5; the horizon size on the surface of last scattering is $\sim 1^\circ$ on the sky. This situation presents a fundamental causality problem – how could causally disconnected points in the early universe have precisely the same temperature? Our current understanding of the dynamics of the very early universe is theoretical and based on the inflationary paradigm, which postulates a burst of accelerated expansion shortly after the Big Bang. During inflation, the scale size expanded through many e-foldings thereby dilating quantum fluctuations in the inflaton field to the macroscopic scales responsible for seeding large-scale structure in the universe and forcing the geometry of the universe to be flat. This evolution solves the horizon problem because causally disconnect points at last scattering were causally connected prior to the inflationary epoch.

The universe we observe today suggests inflation occurred. However, the precise time, or energy scale, at which it occurred is unknown and variable in the theory; a measurement is required to accurately constrain the inflationary epoch. To date, particle physics experiments are more than twelve orders of magnitude away from accessing the energy scales required to provide this constraint. Different inflationary models with different energy scales predict different ratios of tensor and scalar perturbations in the primordial plasma. If the energy scale of inflation lies between 1.1×10^{15} GeV and 2.6×10^{16} Gev [15, 12, 13, 14] then CMB polarization anisotropy experiments sensitive enough to measure both the E-mode and primordial B-mode power spectra will measure the tensor-to-scalar ratio and therefore the energy scale of inflation.

Figure 1.2 shows the temperature anisotropy, E-mode and B-mode polarization anisotropy power spectra computed using the WMAP ΛCDM cosmology with $\Omega_b = 0.044$, $\Omega_c = 0.226$, $\Omega_\Lambda = 0.73$, $\tau = 0.17$ and $n_s = 0.93$ [8, 16]. Over plotted is a predicted foreground signal: a non-primordial B-mode polarization anisotropy produced by the gravitational lensing of partially polarized CMB radiation as it passed by clusters of galaxies. For all solid curves, we assume the quadrupole tensor-to-scalar ratio, $r = 0.1$. The broad blue region illustrates the range of inflationary energy scales future B-mode experiments can probe: 1.1×10^{15} GeV to 2.6×10^{16} Gev. These energy scales correspond to $r_{min} \sim 10^{-6}$ and $r_{max} = 0.3$ given the expression

$$(V^*)^{1/4}/m_{pl} = 3.0 \times 10^{-3} r^{1/4} \tag{1.1}$$

where $m_{pl} = 1.2 \times 10^{19}$ GeV and $r \equiv \langle Q_T^2 \rangle / \langle Q_S^2 \rangle$ [12]. This range in energy scales is set by the current upper limit for r and the ability to cleanly separate the primordial and non-primordial B-mode signals using current data analysis techniques.

A full characterization of the E-mode polarization anisotropy power spectrum will benefit cosmology in several ways. If the signal appears as predicted, the result will further buttress the adiabatic inflationary paradigm by verifying the cosmological origin of the temperature anisotropy. In addition, we will ascertain the values of a collection of cosmological parameters to high accuracy which will strengthen the existing constraints and because the polarization anisotropy measurements are independent, break existing degeneracies between cosmological parameters.

If inflation results from Grand Unified Theory (GUT) physics, the B-mode signal amplitude should be in the range 1 to 100 nK, a few percent or less of the total polarization and some 80 dB fainter than the 2.7 K background. What is clear is that in order to fully explore all the CMB has to offer, we must build receivers with unprecedented sensitivities and, depending on the energy scale of inflation, we may need to develop techniques for cleanly separating the primordial and non-primordial B-mode signals.

MAXIPOL aims to simply detect the peaks of the E-mode curve in Figure 1.2. Toward this end,

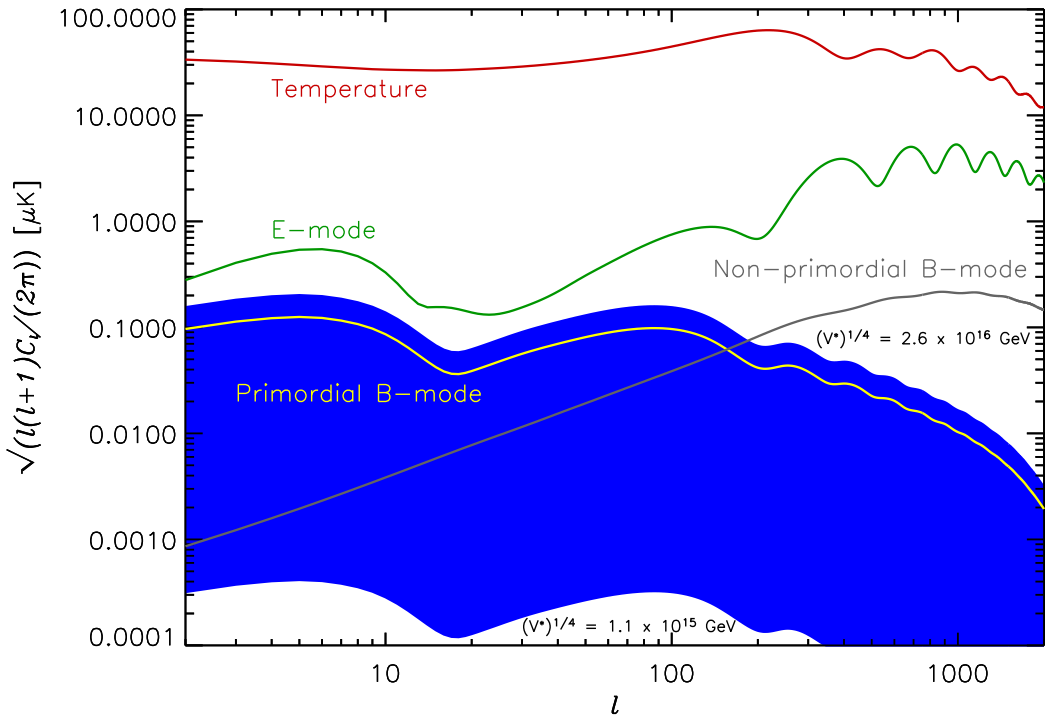

Figure 1.2: Theoretical temperature anisotropy, and E-mode, primordial B-mode and non-primordial B-mode polarization anisotropy power spectra for a ΛCDM universe with $\Omega_b = 0.044$, $\Omega_m = 0.27$, $\Omega_\Lambda = 0.73$, $\tau = 0.17$ and $r = 0.1$. The broad blue region illustrates the range of inflationary energy scales future B-mode experiments can probe (see Section 1.2) [16].

a data set was collected in May 2003 and as of July 2004, preliminary maps have been produced (see Figure 1.3). The algorithm used to compute these maps will be discussed in Chapter 5.

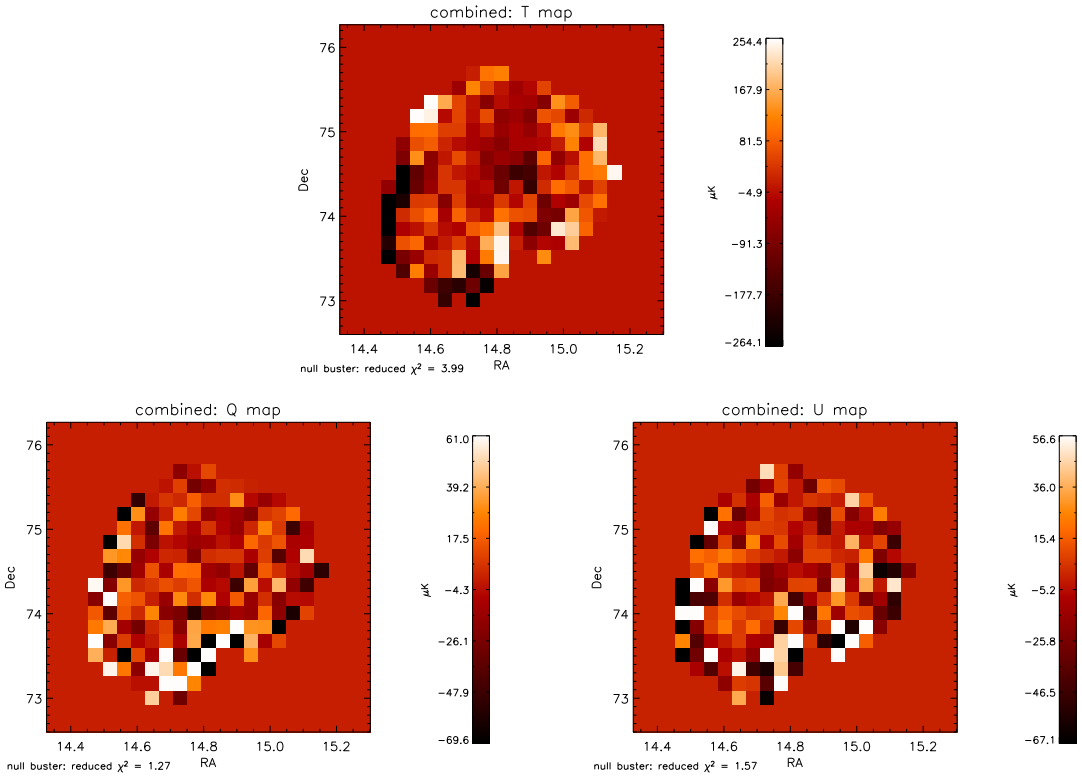

Figure 1.3: Preliminary MAXIPOL T, Q and U sky maps of the region surrounding Beta Ursae Minoris (Chapter 5).

Chapter 2

The MAXIPOL Instrument

2.1 Introduction

The MAXIPOL instrument is a reimplementation of the hardware from the successful CMB temperature anisotropy experiment MAXIMA [3, 4, 5, 6]. While the MAXIMA telescope and data electronics remained largely unchanged, the receiver was converted into a polarimeter by retrofitting it with a rotating half-wave plate (HWP) and a fixed wire-grid polarizer. MAXIPOL was launched twice from NASA's National Scientific Ballooning Facility in Ft. Sumner, New Mexico. The first flight, MAXIPOL-0, took place in September 2002 and the second, MAXIPOL-1, in May 2003. The goal of MAXIPOL is to measure the peaks in the E-mode (EE) and temperature-E-mode (TE) cross correlation power spectra between ℓ=300 and ℓ=1000 (Figure 2.1). To accomplish this goal, MAXIPOL mapped the I, Q and U Stokes parameters of 2° wide "bow tie" shaped regions of the sky with 10′ resolution.

2.2 Instrument Description

Many subsystems in the MAXIPOL instrument have already been thoroughly detailed in previous MAXIMA publications [3, 17, 19, 20, 18]. This discussion will focus primarily on the new MAXIPOL-specific hardware elements that were retrofitted into the MAXIMA instrument.

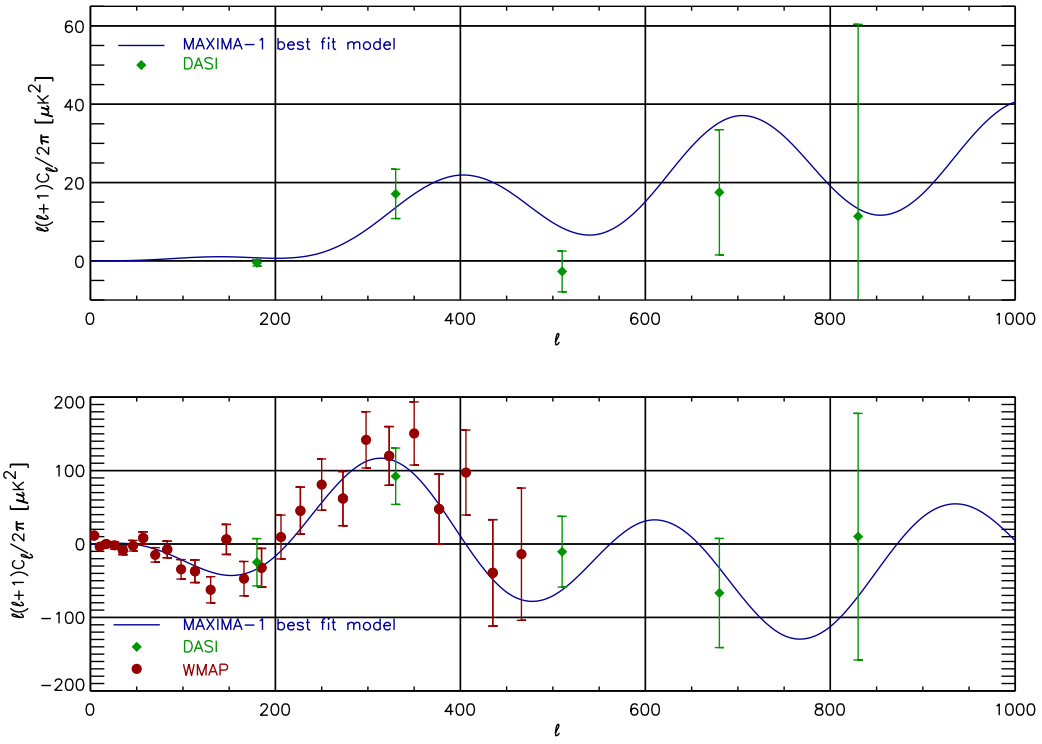

Figure 2.1: Theoretical EE and TE power spectra computed with the MAXIMA-1 best fit cosmological parameters. The current measurements from DASI and WMAP are overplotted. MAXIPOL aims to to measure the peaks in these power spectra between ℓ=300 and ℓ=1000.

2.2.1 Overview

MAXIPOL employs a three mirror, f/1 Gregorian telescope with a 1.3 m off-axis parabolic primary mirror. The elliptical secondary and tertiary reimaging mirrors (21 and 18 cm in diameter, respectively) are held at liquid helium temperatures inside the receiver to reduce radiative loading on the bolometers. To keep the instrumental polarization properties of the telescope constant, all telescope mirrors are fixed with respect to each other for all observations.[1]

Light from the sky is reimaged to a 4 × 4 array of horns at the focal plane. Observations are made in bands centered on 140 GHz and 420 GHz ($\Delta\nu \simeq 30$ GHz). The twelve 140 GHz photometers are optimized to measure the CMB and the four 420 GHz photometers are used to monitor foreground dust contamination. The 10′ FWHM Gaussian beam shape for the 140 GHz photometers is defined

[1]The primary mirror was chopped in azimuth during MAXIMA observations.

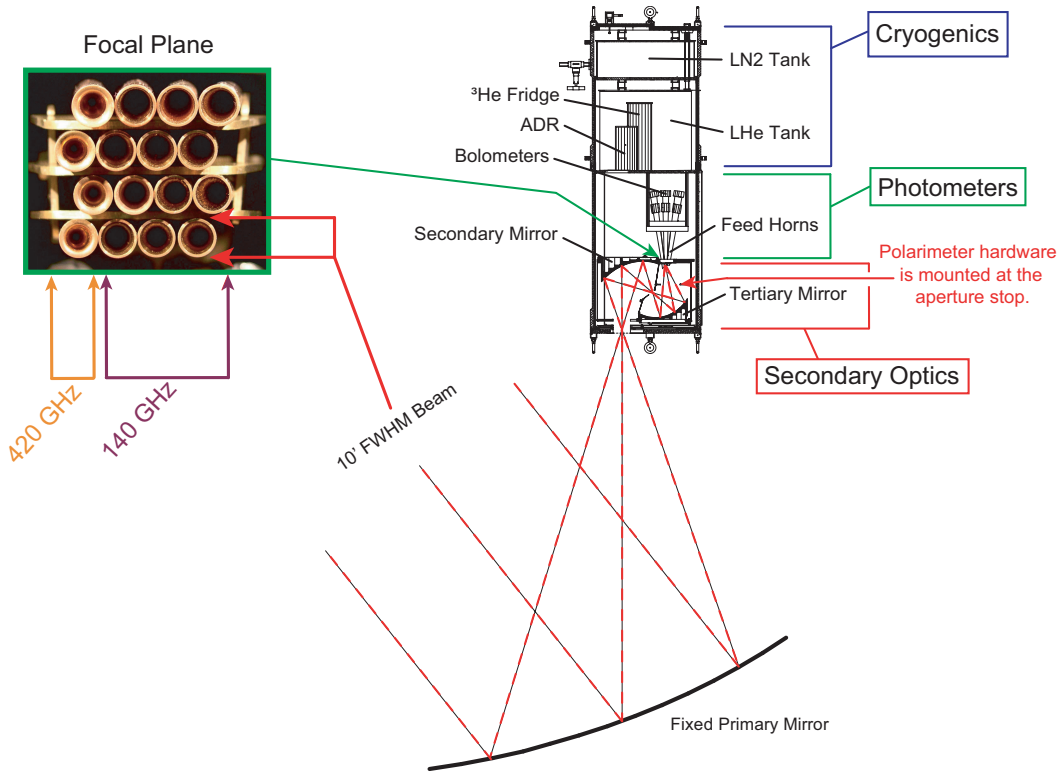

Figure 2.2: A cross-sectional view of the MAXIPOL receiver (Section 2.2).

by a smooth walled, single-mode conical horn and a cold Lyot stop; the 420 GHz photometers employ multi-mode Winston horns. The bolometers are maintained at 100 mK by an adiabatic demagnetization refrigerator [24] and a 300 mK ^{3}He refrigerator. A photograph of the focal plane and a cross-sectional view of the inside of the cryostat is shown in Figure 2.2. For reference, the HWP and wire-grid polarizer that will be discussed in Section 2.2.2 are mounted near the Lyot stop and at the focal plane, respectively.

The telescope was focused before flight by mapping the detector beams with a chopped, 100 Watt halogen filament imaged at infinity by a 38 inch on-axis parabolic mirror. In addition, the telescope sidelobe performance was ascertained by measuring the bolometer response from a chopped, polarized 150 GHz source positioned about the telescope in azimuth and elevation (Figure 2.3). An absorptive, 0.75 inch thick plug of Eccosorb MF110 was inserted in the optical path at the intermediate focus of the telescope to attenuate the intensity of warm loads during lab measurements. This attenuator was anti-reflection (AR) coated with a 0.015 inch thick sheet of etched Teflon. The calculated transmission was $\sim$1% at 140 GHz [23].

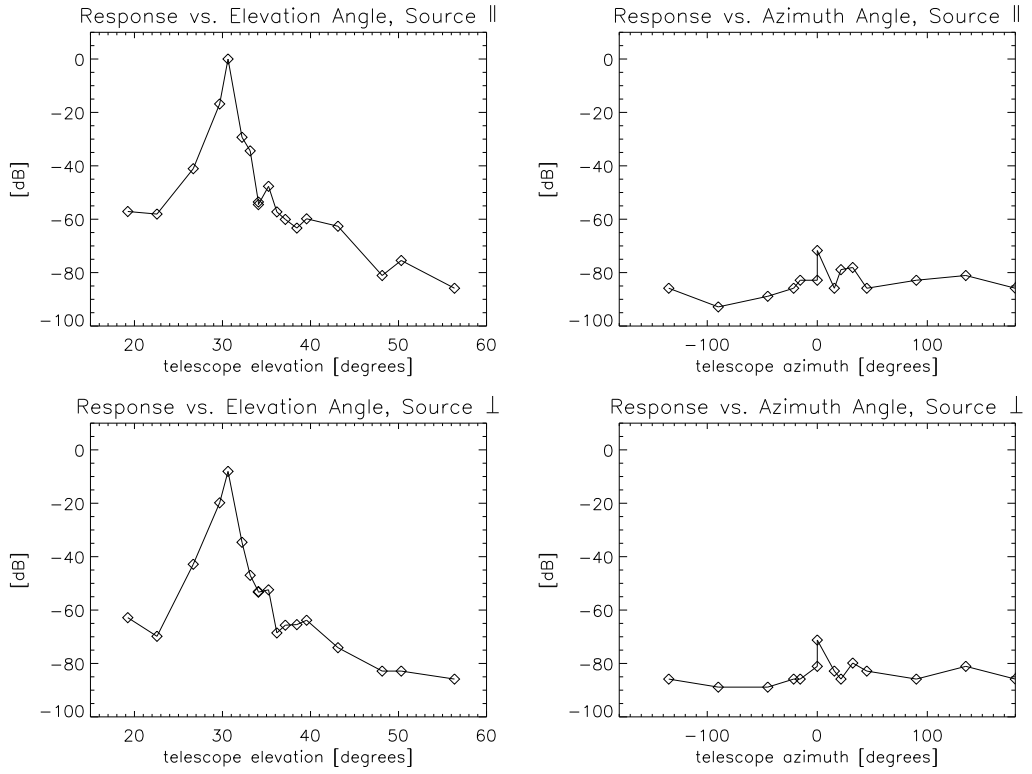

Figure 2.3: A measurement of the sidelobe performance of the MAXIPOL instrument. For this measurement, the amplitude of the bolometer response from a chopped linearly polarized 150 GHz source was measured with a lock-in amplifier. The HWP was not rotating for this test and its orientation was arbitrarily set. Data was collected for two orthogonal orientations of the source – one parallel to the transmission axis of the focal plane polarizer and one perpendicular. For the elevation measurements, the sorce was positioned at an elevation of 32°. For the azimuth measurements, the source was on the ground at an elevation of 0° and the the telsecope was pointed at an elevation of 19.2°. All data were collected with the instrument out in the open on the launch pad at the NSBF in Ft. Sumner, New Mexico to avoid spurious signals from reflections off of buildings or other structures. All data were normalized to the maximum value in the data set. The 90 dB range was possible because of tunable attenuators on the source.

A schematic of the MAXIPOL instrument can be seen in Figure 2.4. This illustration shows the payload without sun shielding so the telescope, receiver and attitude control subsystems are visible. Before flight, sun shielding was installed to protect all subsystems from solar radiation during daytime observations and to shield the telescope and receiver from spurious signals caused by sunlight and RF transmitters. The baffling was made of Celotex aluminized foam sheeting and was painted white on all Sun and Earth-facing surfaces. We selected a white paint pigmented with TiO_2 because this material has low solar absorptivity ($\sim$10%) and high infrared emissivity ($\sim$90%) – a combination that compensated for the loss of convective cooling in the low-pressure balloon environment by providing adequate radiative cooling. This sun shield design successfully maintained all instrument subsystems within nominal temperature specifications during the daytime portion of the flight. A large aluminum ground shield (also not illustrated) was mounted to the inner frame

to shield the main beam of the telescope from terrestrial emission.

Telescope attitude was feedback controlled. The flywheel mounted at the top of the gondola moved the telescope in azimuth while the elevation angle was adjusted with a linear actuator arm that nodded the entire inner frame. A second motor mounted at the very top of the gondola further assisted in moving the telescope in azimuth by torquing the payload against the balloon cabling. The azimuth feedback-loop relied on gyros and a magnetometer and the elevation feedback relied on a 16-bit optical encoder. The magnetometer was calibrated before flight; the offset was measured to within a degree and the non-linearity was mapped and stored in a lookup table that was used by the on-board pointing computer during flight for making fine corrections. A second lookup table was also implemented to account for variations in the magnetic field of the Earth as a function of longitude and latitude.

Pointing reconstruction for data analysis relies on the position of a reference star in one of two boresight Cohu 4910 CCD cameras. The camera used during daytime observations was filtered with a 695 nm Schott glass filter and fitted with a 500 mm Promaster Spectrum 7 reflective lens that provided a 0.72° by 0.55° field-of-view; the unfiltered nighttime camera used a 50 mm Fujinon lens that provided a 7.17° by 5.50° field-of-view. Pixel size for the daytime and nighttime cameras was $0.084'$ by $0.069'$ and $0.84'$ by $0.69'$, respectively. The small field-of-view and the filter on the daytime camera were necessary to improve the ratio of star to sky brightness. With the combination, we detected stars of apparent visual magnitude 2 at balloon altitude. The two cameras and the telescope were aligned before flight to within a quarter of a degree.

Bolometer data and housekeeping signals were multiplexed into a single data stream that was telemetered to fixed ground stations during flight. These signals were monitored in real time to ensure nominal operation of the instrument and because the cryogenic system needed to be manually cycled.

A new on-board data recorder was added to the experiment for the MAXIPOL-1 flight after a NASA data transmitter failed during MAXIPOL-0. The data recorder, which was custom designed and built by the Weizmann Institute of Science in Israel, consists of NIM modules each containing an Altera FPGA chip and up to 128 Intel 16 MB flash memory chips. With an uncompressed serial data rate of 160 kbps each module is capable of storing 28.4 hours of data. Individual modules can be daisy-chained to each other to increase the total recording capacity. The FPGA chip reads the incoming data stream and when it detects a pre-programmed frame structure it controls the storage of the data on the memory chips. It also controls the post-flight export of the data from the memory chips into a computer through a standard parallel port. Power consumption during steady-state data recording is less than 0.25 Watt (at 5 V), and modules that are idle require only

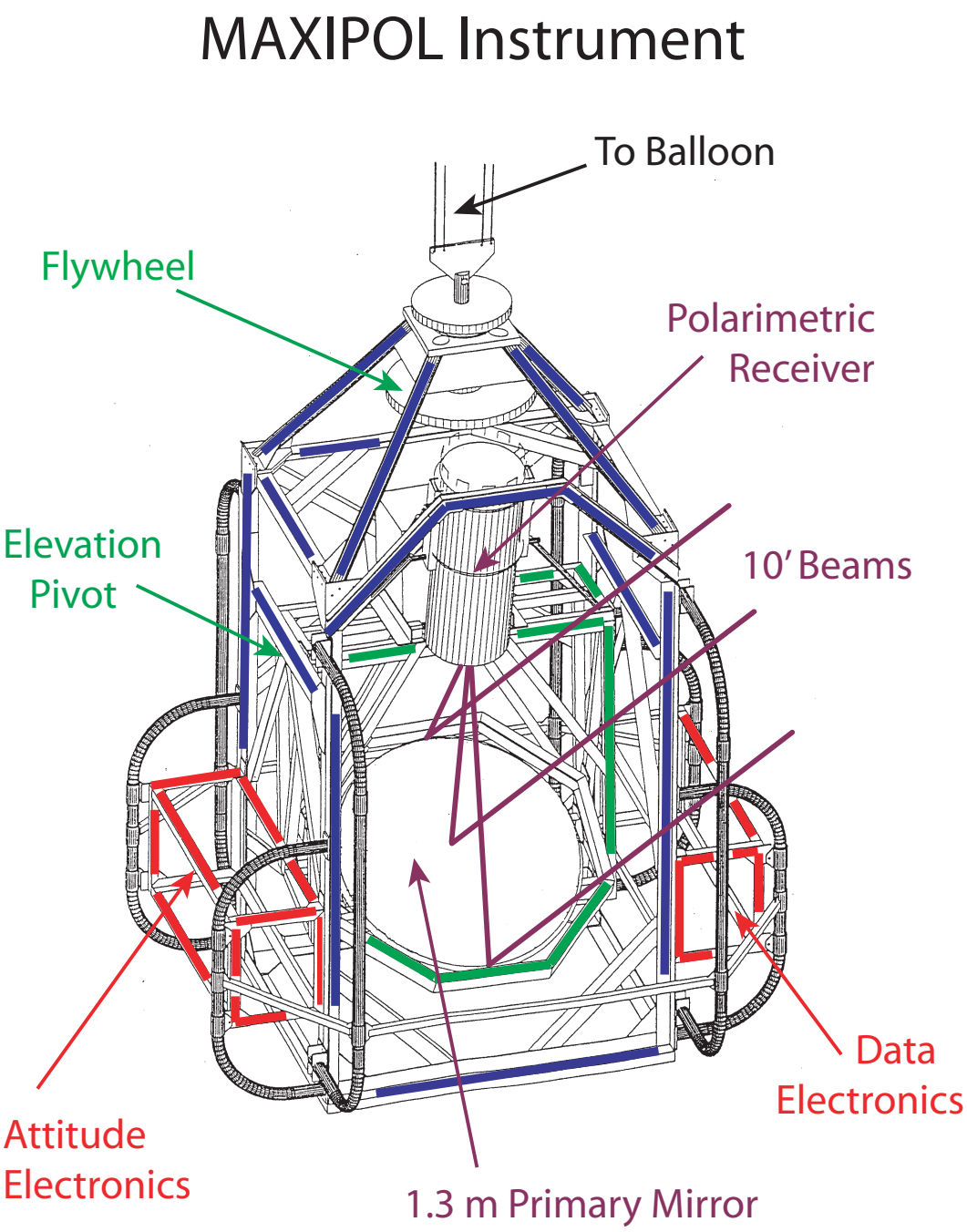

Figure 2.4: The MAXIPOL instrument without baffling (Section 2.2).

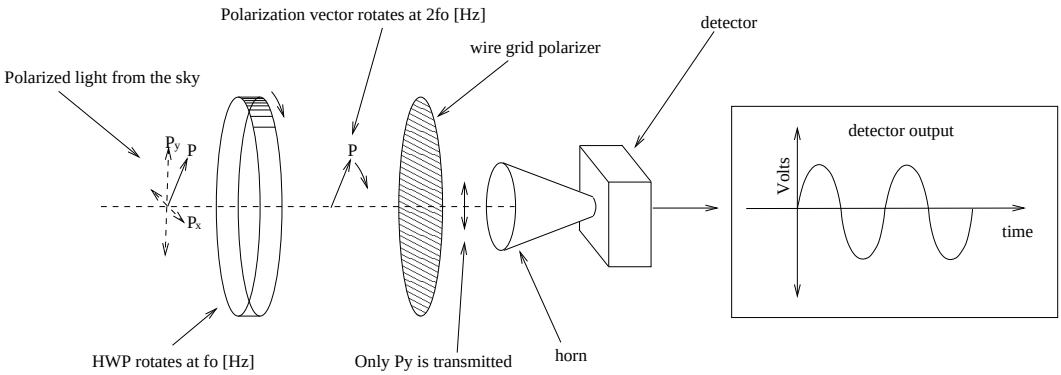

Figure 2.5: The polarimeter strategy employed by MAXIPOL (Section 2.2.2).

about 0.05 Watt. For MAXIPOL-1 two modules containing 96 memory chips provided a total recording capacity of 42.6 hours. Approximately 28 hours of pre-flight, ascent and at-float data were recorded.

2.2.2 Polarimeter Strategy

MAXIPOL analyzed the polarization of the millimeter-wave sky with a rotating HWP and fixed wire-grid polarizer. While this technique is a well-known standard in astronomy, it is the first implementation in a CMB experiment. The strategy is illustrated in Figure 2.5.

Monochromatic linearly polarized light that passes through a HWP rotating at a frequency f_0 emerges linearly polarized with its orientation rotating at $2f_0$. If this light then propagates through a fixed polarizer and its intensity is subsequently measured, the resulting data stream will exhibit sinusoidal modulation at $4f_0$. The amplitude of this modulation depends on the level of polarization of the incident radiation. Perfectly polarized light will maximize the amplitude and perfectly unpolarized light will yield no modulation.

The advantage of HWP polarimetry is that each detector in the array makes an independent measurement of the Stokes parameters of the incoming radiation. In addition, this technique rejects systematic errors. Spatial polarization variations on the sky translate to temporal amplitude variations in the $4f_0$ signal because the telescope is scanning. Therefore, the polarization anisotropy data will reside in the sidebands of the $4f_0$ signal in Fourier space. Any spurious or systematic signals appearing in the data stream outside of this $4f_0$ frequency band can be filtered away with software during data analysis (see Section 2.3).

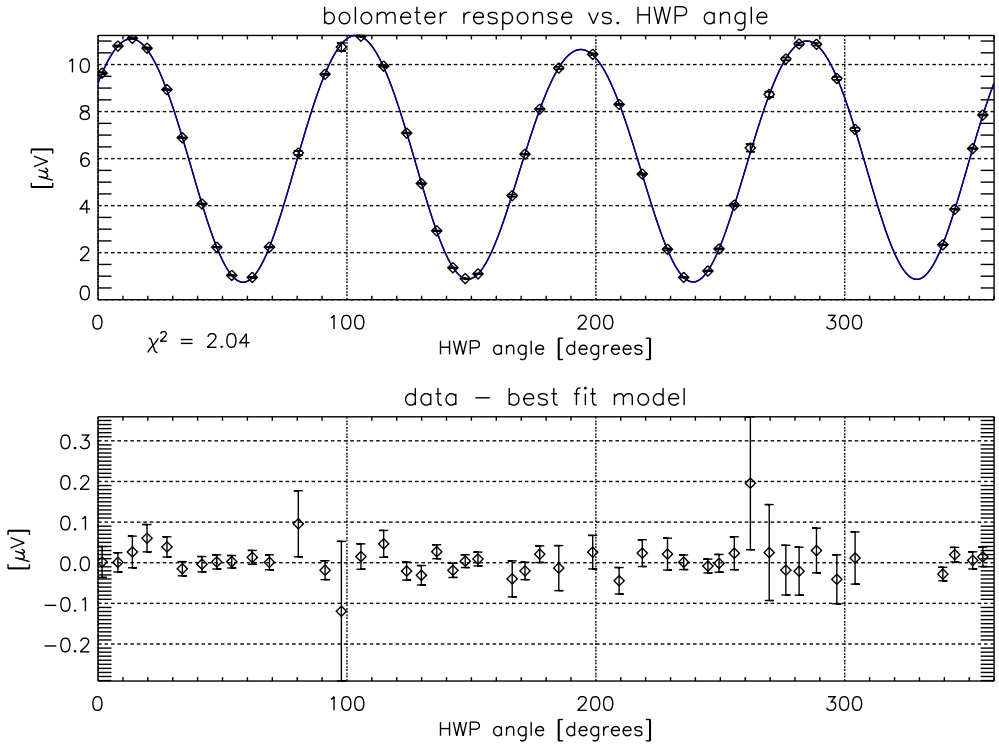

Figure 2.6: A lab measurement of a polarized load. The setup for this measurement is described in Section 2.2.2 and a more detailed discussion is presented in Section 3.3. The solid curve plotted is the best fit model comprised of nf_0 sine waves where $n = 1, 2, \ldots, 8$; the seventeen free parameters used in the fit include the amplitude and phase of each sine wave and an overall offset. For this model, $\chi^2 = 2.04$ for 45-17 degrees of freedom. The data minus the best fit model is plotted in the bottom panel to elucidate the measurement error. From the fit parameters, we calculated the polarimeter efficiency to be 89%.

The HWP is inherently a monochromatic device so the behavior described above applies only to the frequencies $\nu = mc/2t\Delta n$ where Δn is the difference between the ordinary and extraordinary indicies of refraction in the birefringent crystal, t is the propagation length through the crystal, m is an odd integer and c is the speed of light. Linearly polarized light at other frequencies emerges from the crystal elliptically polarized. We calculated the HWP thickness that would minimize the fraction of elliptically polarized intensity and thereby optimize the overall polarimeter efficiency. To do this, we found the maximum of the product of the expected efficiencies for the 140 and 420 GHz photometers as a function of crystal thickness. These expected efficiency curves incorporated the spectral breadth of the photometers and the convergence of rays as they propagate through the HWP. The HWP design that resulted from this calculation is discussed in Section 2.2.3.

To ascertain the polarimeter efficiency, a polarized load was analyzed in the lab before flight. For this measurement, a wire-grid polarizer was mounted on the cryostat window with its transmission axis oriented parallel to that of the focal plane polarizer. Thermal radiation from a 273 K ice

bath was chopped at ∼6.5 Hz with a 300 K aluminum chopper blade covered with 0.25 inch thick Eccosorb LS-14 foam. The HWP was then discretely stepped by hand in ∼5° intervals. Twenty seconds of data were collected at each HWP orientation. The amplitude of the chopped signal in the bolometer time stream for one typical photometer was measured with a software lock-in analysis and then plotted in Figure 2.6. A nine parameter model consisting of sine waves for the first eight harmonics of f_0 was then fit to the data (solid curve); fit parameters included the amplitudes and phases of each sine wave and an overall offset. The level of polarization was then calculated from the fit parameters using the standard definition $P = (A_{max} - A_{min})/(A_{max} + A_{min})$ where A is the amplitude of the $4f_o$ signal. This calibrated load was measured to be 86% polarized. This corresponds to an overall polarimeter efficiency of 89% which is in agreement with predictions that take into account the HWP thickness, the known spectral response of the 140 GHz photometers, the convergence of rays at the aperature stop of the telescope and the wire-grid polarizer efficiency (more details in Section 3.3).

Incident unpolarized light can become partially polarized inside the instrument if it reflects off of the telescope mirrors at oblique angles. In addition, emission from the mirrors may also be partially polarized. To assess the level of instrumental polarization the procedure outlined above was repeated with unpolarized light. We found the instrumental polarization to be 1% for a typical 140 GHz channel.

2.2.3 Half-Wave Plate and Wire-Grid Polarizer

The 3.4 mm thick A-cut sapphire HWP was AR coated with a 0.013 inch thick wafer of Herasil to maximize transmission. The Herasil was bonded to the sapphire with Eccobond 24, an unfilled, low viscosity epoxy that was used to achieve glue layers as thin as 0.0005 inches. For MAXIPOL-0 we AR coated the HWP with a 0.010 inch thick layer of Stycast 2850FT. The switch from Stycast to Herasil was made because Herasil thermally contracts in a way that is more compatible with sapphire.

Since the AR coating was not birefringent, the two incident polarization orientations had different coefficients of reflection; this differential reflection gave rise to a rotation synchronous signal at a frequency of $2f_0$. To minimize this effect, we calculated the AR coating thickness that would minimize the difference in reflection coefficients given the spectral breadth of the 140 GHz photometers, the thickness of the eccobond 24 layer and the oblique incidence of rays. Because the $2f_0$ signal resides out of the polarization signal bandwith around $4f_0$ it is not a source of systematic error (see Section 2.3).

The focal plane wire-grid polarizer, made by Buckbee-Mears, was constructed from electroformed 0.0002 inch diameter gold wires bonded to 0.0015 inch thick Mylar film at 250 lines per inch. This flexible material was mounted to a rigid "roof-shaped" frame that was positioned over the horn openings. This "roof-shaped" polarizer reflected the unwanted polarization orientation out of the optical path and into blocks of millimeter-wave absorbing material [25] mounted on either side of the focal plane. This design reduced spurious signals due to reflections.

2.2.4 HWP Drivetrain

The HWP rotated at ∼2 Hz during both MAXIPOL flights. This speed was selected because it provided eight measurements of the of Stokes parameters for one beam resolution element per scan period while avoiding any significant $4f_0$ signal attenuation from the ∼10 ms bolometer time constant. During operation, this rotation speed proved to be vibrationally gentle; it did not excite any detectable microphonic signals in the bolometer data.

The HWP was center turned near the Lyot stop of the telescope by a 0.078 inch diameter driveshaft (see Figure 2.7). This driveshaft penetrated the tertiary mirror and the cryostat shell and was turned through a low-temperature ferrofluid rotary vacuum feedthrough (Ferrofluidics FE51-122190A) by a feedback controlled Kollmorgen U9M4 Servo Disc DC motor with high-altitude brushes mounted outside the receiver. The orientation of the motor shaft, and therefore the HWP, was measured with a 16-bit Gurley A25S optical encoder.

The HWP was held in place near the Lyot stop with a Rulon-J sleeve bearing embedded in a 0.4 inch thick disk of Zote foam. A sapphire bearing was used in MAXIPOL-0 but was later found to exhibit less favorable vibrational properties. This foam disk was mounted in the optical path perpendicular to the chief ray. A polished, hardened-steel sewing needle was passed through a center drilled hole in the HWP; the assembly resembled a toy top. One end of the needle was slipped into the Rulon-J sleeve and the other end was rigidly coupled to the driveshaft with 907 epoxy.

The driveshaft had three main parts. Between the HWP and the tertiary mirror, the driveshaft was made of thin wall G10 tubing (wall thickness $\simeq$ 0.005 in). The thin fiberglass G10 material minimized both the thermal load on the HWP and the optical cross-section of the exposed driveshaft, while retaining the desired torsional driveshaft stiffness. A bearing assembly was mounted at the back of the tertiary mirror to act as a thermal intercept and to provided necessary mechanical stability for the driveshaft. The bearing was made of Rulon-J (Vespel SP3) for MAXIPOL-1 (MAXIPOL-0). Inside this bearing, the driveshaft was made of polished steel, sputter coated

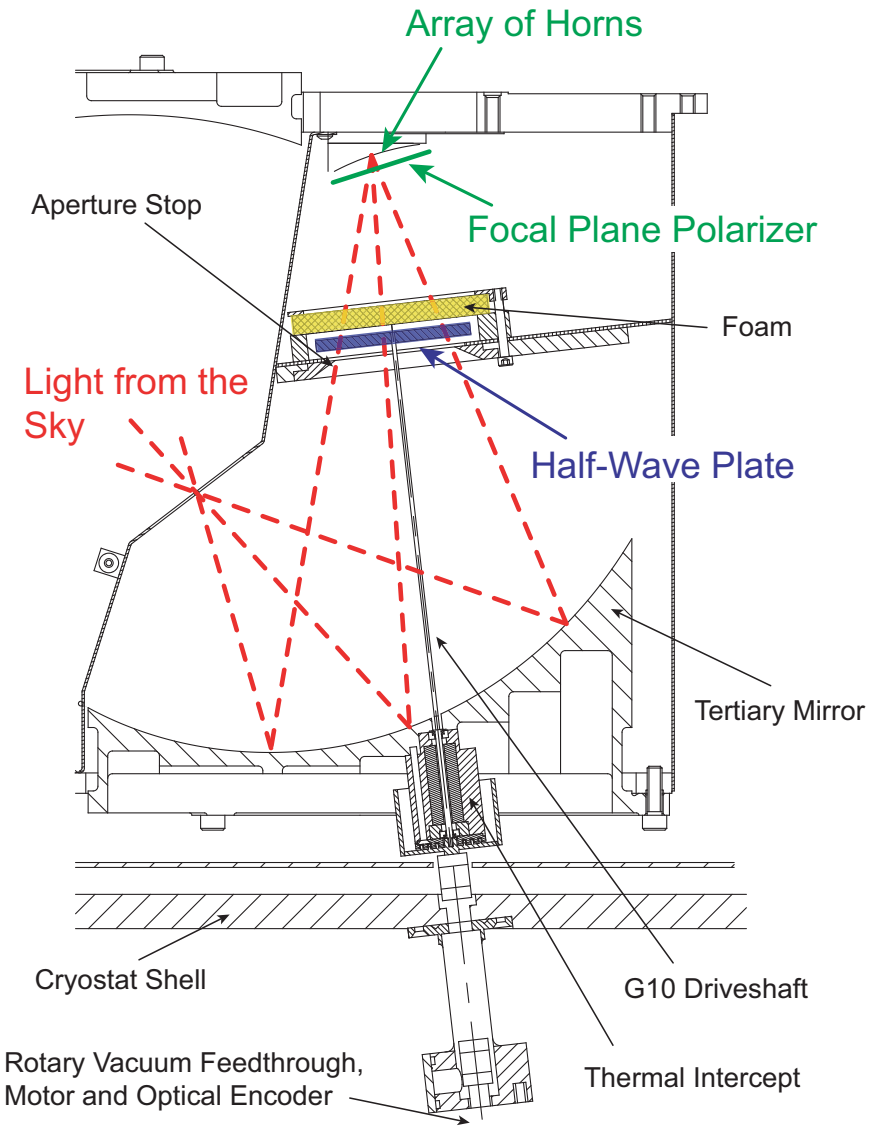

Figure 2.7: A cross-sectional view of the MAXIPOL polarimeter (Section 2.2.4).

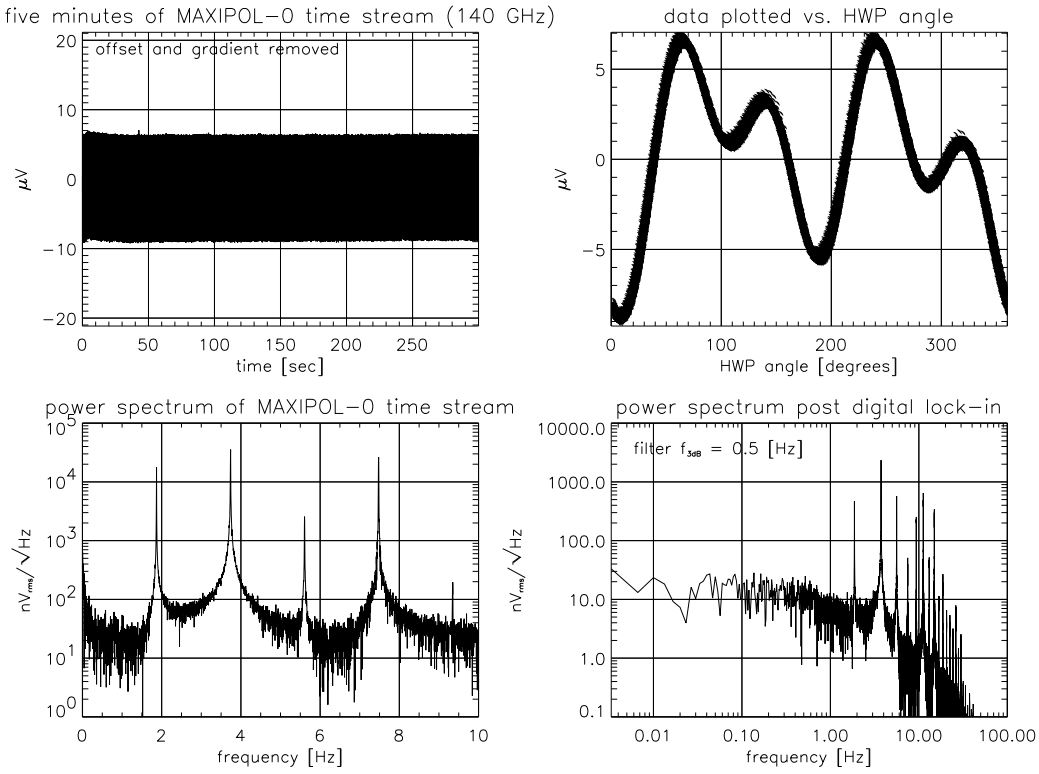

Figure 2.8: A software lock-in analysis of five minutes of MAXIPOL-0 data (See the discussion in Section 2.3).

with MoS_2; the shaft material was cromoly steel (titanium nitride coated tungsten carbide) for MAXIPOL-1 (MAXIPOL-0). Between the tertiary mirror and the rotary vacuum feedthrough at the cryostat shell the driveshaft was again made of G10 tubing to minimize the thermal load on the HWP and the liquid helium bath.

Laboratory testing was carried out to test the vibrational properties of the drivetrain assembly at liquid helium temperatures. A mock-up of the drivetrain was constructed and installed in a liquid helium cryostat. With this setup, two bearing materials, Rulon-J and Vespel SP3, were studied with microphones mounted near the bearings inside the cryostat. Rulon-J was chosen as the flight drivetrain bearing material because of the low noise performance it exhibited over several consecutive days of testing.

2.3 Flight Performance

The purpose of this section is to demonstrate the viability of the instrument. Five minutes of MAXIPOL-0 time stream data from one 140 GHz photometer are plotted in the upper left panel of Figure 2.8. When this data is replotted versus HWP angle, the systematic offsets become apparent (upper right panel).

Plotted in the lower left panel is the power spectrum of this data set. The first peak appears at f_0 and the subsequent peaks appear at the harmonics of f_0. Laboratory measurements show that the source of the f_0 signal is predominantly thermal emission from the G10 drivetrain. This thermal emission signal contributes at all harmonics in the plot though it is subdominant in the $2f_0$ and $4f_0$ peaks. The dominant $2f_0$ signal comes from the differential reflection effect discussed in Section 2.2.3; the dominant $4f_0$ signal comes from the instrumental polarization signal discussed in Section 2.2.2.

As discussed in Section 2.2.2, polarization anisotropy measurements will appear in the sidebands of the $4f_0$ signal. If the amplitude of the systematic offset at $4f_0$ varies, this modulation may mimic polarization signals from the sky. To measure its stability, we lock-in on the $4f_0$ offset with software using a reference created from the HWP optical encoder data stream. The time dependence of the locked-in data provides a measure of the stability of the amplitude of the $4f_0$ offset. The power spectrum of this locked-in data is plotted in the lower right panel of Figure 2.8. In the bandwidth of interest spanning 0 to 1.5 Hz we recovered the nominal instrument noise level of $\sim$10 $\mathrm{nV}_{rms}/\sqrt{\mathrm{Hz}}$; this bandwith was set by the scan speed of the telescope, the beam size and the angular size of the expected structure on the sky (Section 5.3). We therefore conclude that variations in the known systematic offsets will contribute less than the detector noise to the the MAXIPOL data.

Chapter 3

Polarimeter

In this chapter we discuss the MAXIPOL polarimeter. Sections 3.1 & 3.2 are devoted to presenting the theoretical framework used to design and model the performance of the instrument. In Section 3.3 we compare this theoretical performance to a preflight measurement made in May 2003.

For total power detectors it is most convenient to use the Mueller matrix formalism for calculations. In this formalism, the behavior of optical elements is described by a 4×4 Mueller matrix and the signal propagating through the optical system is described by a 4 element Stokes vector

$$\vec{S} = [I, Q, U, V] \tag{3.1}$$

with

$$I = \langle E_x^2 \rangle + \langle E_y^2 \rangle \tag{3.2}$$
$$Q = \langle E_x^2 \rangle - \langle E_y^2 \rangle \tag{3.3}$$
$$U = \langle E_x E_y \cos(\phi) \rangle \tag{3.4}$$
$$V = \langle E_x E_y \sin(\phi) \rangle \tag{3.5}$$

E_x and E_y are the amplitudes of the electric field in the x and y directions, respectively, ϕ is the phase difference between E_x and E_y and the brackets indicate time averaging. I describes the total intensity of the radiation while Q, U and V describe the polarized intensity. For linearly polarized light, $V = 0$ and Q and U are the parameters of interest. Note: the CMB community commonly refers to I as T because intensity is commonly quoted in brightness Temperature units. To be clear, I will mark Stokes vectors with a $\rightarrow$, Muller matrices with a $\wedge$ and scalars will have no symbol.

Figure 3.1 is a schematic representation of the optical elements in the MAXIPOL instrument. To fully model the experiment, one must ascertain the Mueller matrix for each element. The

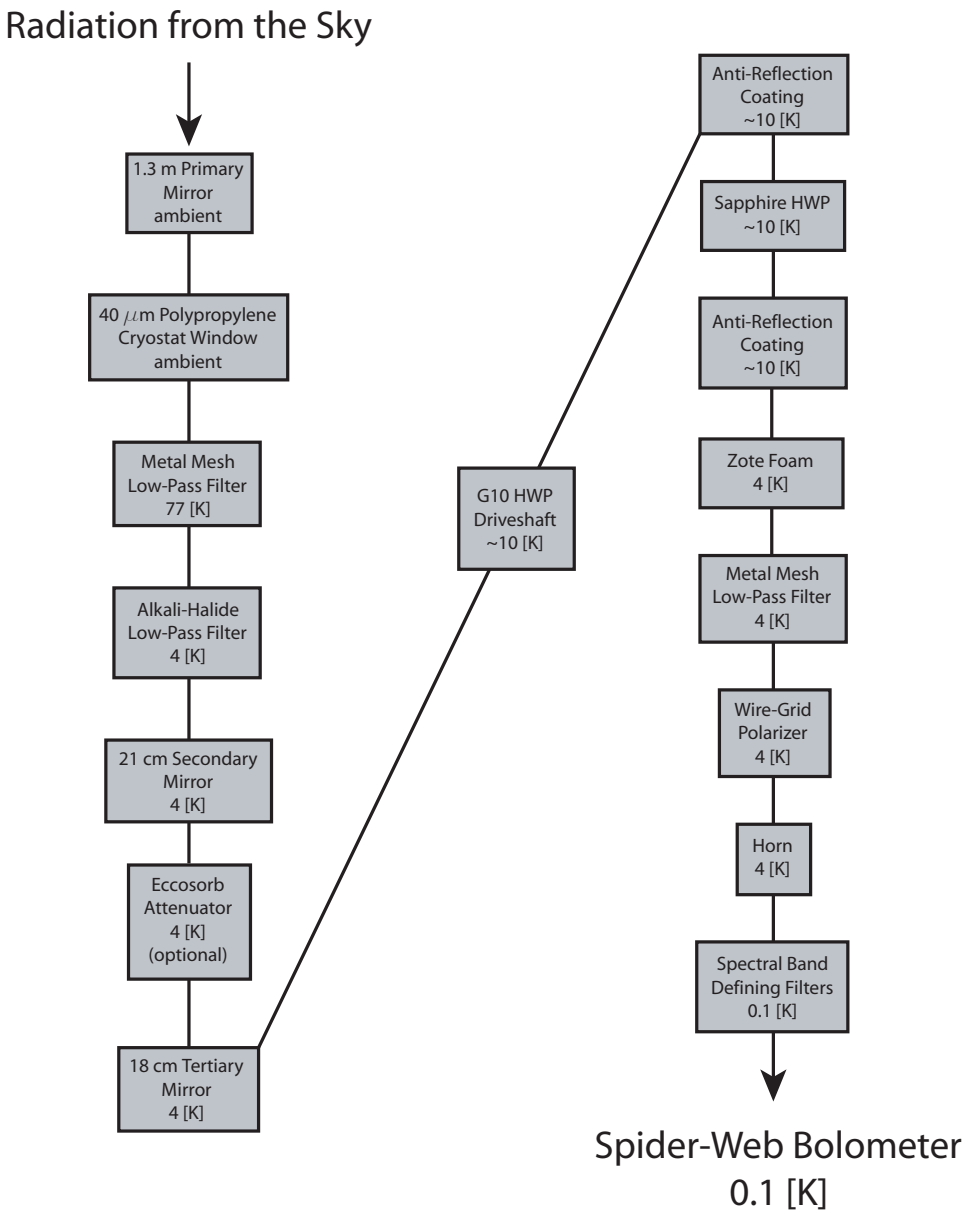

Figure 3.1: Schematic of the optical elements in the MAXIPOL instrument.

heart of the polarimeter is the HWP and the wire-grid polarizer. Before proceeding to the more complicated task of deriving the theoretical behavior of the system, we will present the calculations used to design the MAXIPOL HWP. In this chapter we will explore in detail the impact the HWP and wire-grid polarizer has on the polarimeter data stream but stop short of fully modeling the entire optical system.

3.1 HWP Design

The Mueller matrix for a homogeneous nonlinear retarder can be written

$$\hat{\mathcal{M}}_h = \begin{bmatrix} 1 & 0 & 0 & 0 \\ 0 & d^2 - e^2 - f^2 + g^2 & 2(de + fg) & -2(df + eg) \\ 0 & 2(de - fg) & e^2 - f^2 - d^2 + g^2 & 2(dg - ef) \\ 0 & -2(df - eg) & -2(dg + ef) & g^2 + f^2 - d^2 - e^2 \end{bmatrix} \tag{3.6}$$

with the matrix elements defined as

$$\begin{aligned} d &= Q_e \ \sin(\delta/2) \\ e &= U_e \ \sin(\delta/2) \\ f &= V_e \ \sin(\delta/2) \\ g &= \cos(\delta/2) \end{aligned}$$

This expression is completely general and can be simplified assuming MAXIPOL-specific constraints, namely $Q_e = \cos(2\rho)$, $U_e = \sin(2\rho)$ and $V_e = 0$ which is true for the retarders we use [21]. Here ρ is the orientation angle of the retarder. The parameter

$$\delta = \frac{2\, m\, \pi\, t\, \Delta n}{\lambda} \tag{3.7}$$

where $\Delta n = |n_e - n_o|$, n_e and n_o are the ordinary and extraordinary indicies of refraction, t is the thickness of the crystal, λ is the free-space wavelength of the electromagnetic wave propagating through the crystal and m is an odd integer. If $\delta = m\pi$ then the retarder is a HWP.

Sapphire, MgF_2 and quartz were considered as HWP materials for MAXIPOL. Of the three, we selected sapphire because it has the largest Δn at 140 GHz and therefore required the smallest t which was appealing because there was a tight space budget inside the receiver near the aperture stop where the HWP was mounted. In addition, the mass and moment of inertia of the sapphire crystal for our requisite dimensions proved to be acceptable given our drivetrain strategy.

From the literature we know only $n_o = 3.047$ for 140 GHz radiation at 5.8 K while at 300 K we know both $n_o = 3.065$ and $n_e = 3.404$ for the same frequency [29, 30]. Combining these measurements with others made at higher frequencies [31], we extrapolated that $n_e = 3.361$ at liquid helium temperatures making our $\Delta n = 0.314$. Figure 3.2 shows this extrapolation and gives results for 420 GHz as well.

The penalties associated with using a sapphire HWP include a large overall reflection at the crystal surfaces resulting from the large indices of refraction, an appreciable differential reflection arising from the fact that n_o and n_e are significantly different and a non-zero signal attentuation via absorption. The reflection problems can be managed by using an anti-reflection coating (Section 3.2) and the absorption effect should not be deleterious. The transmission through the crystal can be calculated using the expression

$$\left(\frac{I_{out}}{I_{in}}\right)_{o,e} = e^{-\alpha_{o,e}t} \tag{3.8}$$

From the literature, α_o and $\alpha_e = 0.05$ Neper/cm for 140 GHz radiation at 300 K with $\Delta\alpha$ negligible [30]. α_o was measured again by the same author in a different study to be 0.07 Neper/cm for 140 GHz radiation at 300 K and then 0.05 Neeper/cm at 5.8 K [29]. This result suggests that cooling the HWP improves the transmission by 1%. Considering all measurements, we calculate the signal loss to absorption to be 2% for the 140 GHz photometers. The 300 K absorption coefficients for 420 GHz radiation are $\alpha_o = 0.24$ and $\alpha_o = 0.21$ [30]; these values suggests we should have a differential transmission of 1% in this spectral band. A 1% modulation of the 2.7 K sky would be a detectable signal. However, the 5.8 K measurement of α_o only in [29] suggests this absorptive signal vanishes when the HWP is cooled to 5.8 K.

For a monochromatic experiment one can simply calculate the crystal thickness, t, required to create a HWP from equation 3.7 once the crystal material and therefore Δn is selected. MAXIPOL is not a monochromatic experiment, however, so a slightly more complicated calculation using the known spectral response of the photometers was needed to ascertain the crystal thickness that would produce the optimal overall polarimeter performance.

3.1.1 Modeling the Data Stream

The optical system illustrated in Figure 2.5 can be described mathematically as

$$\hat{\mathcal{M}}_{p_2}\ \hat{\mathcal{M}}_h\ \vec{S}_{in} = \vec{S}_{out} \tag{3.9}$$

The signal to be analyzed, $\vec{S}_{in}$, can modeled as $\hat{\mathcal{M}}_r\hat{\mathcal{M}}_{p_1}\vec{S}_{load}$ where $\vec{S}_{load} = [1, 0, 0, 0]$. This expression allows $\vec{S}_{in}$ to have an arbitrary level of linear polarization and an arbitrary orientation. The

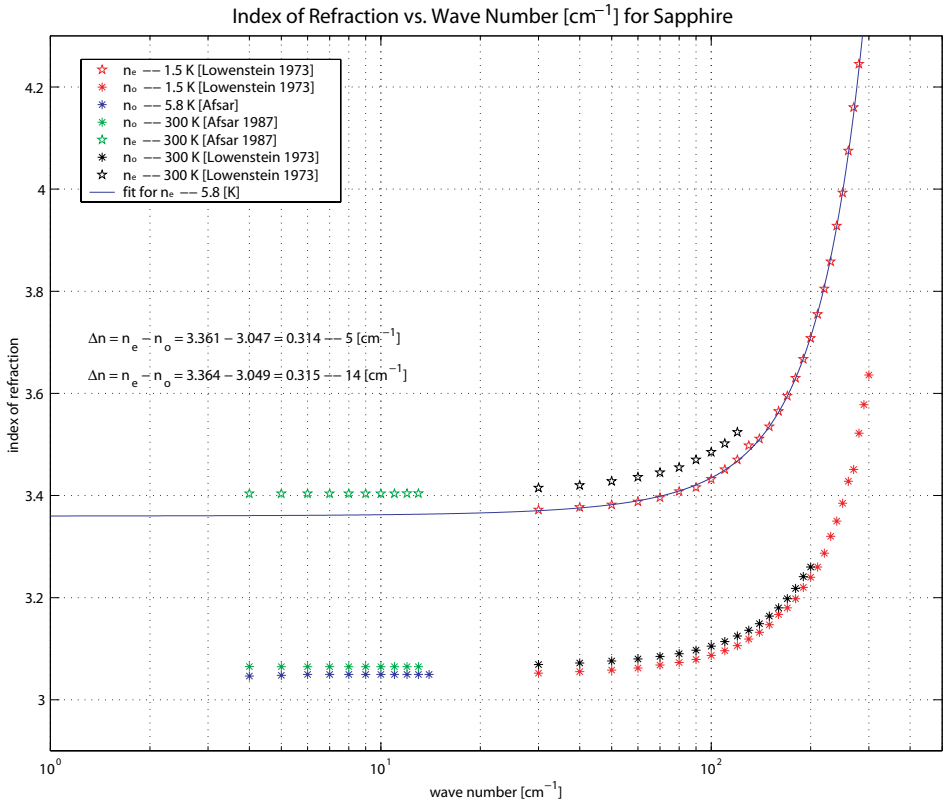

Figure 3.2: Index of refraction of sapphire between 4 and 300 cm^{-1} at liquid helium temperatures and 300 K.

orientation of $\vec{S}_{in}$ is set by a rotation matrix, $\hat{\mathcal{M}}_r$, which is a purely mathematical construct [22].

$$\hat{\mathcal{M}}_r = \begin{bmatrix} 1 & 0 & 0 & 0 \\ 0 & \cos(2\theta) & \pm\sin(2\theta) & 0 \\ 0 & \mp\sin(2\theta) & \cos(2\theta) & 0 \\ 0 & 0 & 0 & 1 \end{bmatrix} \tag{3.10}$$

The upper sign corresponds to clockwise rotation as observed by the detector and the lower sign, counter-clockwise rotation. Here the Mueller matrix for a polarizer is written

$$\hat{\mathcal{M}}_{p_i} = \frac{1}{2}\begin{bmatrix} p_{x_i}^2 + p_{y_i}^2 & p_{x_i}^2 - p_{y_i}^2 & 0 & 0 \\ p_{x_i}^2 - p_{y_i}^2 & p_{x_i}^2 + p_{y_i}^2 & 0 & 0 \\ 0 & 0 & 2p_{x_i}p_{y_i} & 0 \\ 0 & 0 & 0 & 2p_{x_i}p_{y_i} \end{bmatrix} \tag{3.11}$$

with the amplitude attenuation coefficients (p) indexed by i to allow for differentiation between the source polarizer, $\hat{\mathcal{M}}_{p_1}$, and polarizer at the detector, $\hat{\mathcal{M}}_{p_2}$. It is important to distinguish the two polarizers because it is not necessarily true that they will embrace the same orientation or amplitude attenuation coefficients. Using Equation 3.10 and 3.11,

$$\vec{S}_{in} = \frac{1}{2}\begin{bmatrix} p_{x_1}^2 + p_{y_1}^2 \\ (p_{x_1}^2 - p_{y_1}^2)\,\cos(2\theta) \\ (p_{x_1}^2 - p_{y_1}^2)\,\sin(2\theta) \\ 0 \end{bmatrix} \tag{3.12}$$

The bolometric detector is only sensitive to the Ith term of $\vec{S}_{out}$ so the resulting data stream can be written

$$\begin{aligned} \vec{S}_{out}^{I}(\rho,\theta,a,\delta) &= I_{out} = \frac{1}{4}[(p_{x_1}^2 + p_{y_1}^2)(p_{x_2}^2 + p_{y_2}^2) \\ &+ (p_{x_1}^2 - p_{y_1}^2)(p_{x_2}^2 - p_{y_2}^2)\cos(2\theta)((1+\cos(4\rho))\sin^2(\delta/2) + \cos^2(\delta/2)) \\ &+ (p_{x_1}^2 - p_{y_1}^2)(p_{x_2}^2 - p_{y_2}^2)\sin(2\theta)\sin(4\rho)\sin^2(\delta/2)] \end{aligned} \tag{3.13}$$

This equation is messy. In general, the level of polarization can be calculated using the expression

$$P = \frac{\sqrt{Q^2 + U^2 + V^2}}{I} \tag{3.14}$$

Using this expression on the elements of $\vec{S}_{in}$, we find

$$P_{in} = \frac{p_{x_1}^2 - p_{y_1}^2}{p_{x_1}^2 + p_{y_1}^2} \tag{3.15}$$

and the normalized input Stokes vector becomes

$$\vec{S}_{in} = \begin{bmatrix} 1 \\ P_{in}\,\cos(2\theta) \\ P_{in}\,\sin(2\theta) \\ 0 \end{bmatrix} \tag{3.16}$$

Using the normalized $\vec{S}_{in}$ and assuming $p_{x_2} = 1$ and $p_{y_2} = 0$, Equation 3.13 simplifies to

$$\begin{aligned} I_{out} = \frac{1}{2}\,[\,1 &+ P_{in}\cos(2\theta)\,\left(\cos(4\rho)\,\sin^2(\delta/2) + \cos^2(\delta/2)\right) \\ &+ P_{in}\sin(2\theta)\,\sin(4\rho)\,\sin^2(\delta/2)\,] \end{aligned} \tag{3.17}$$

3.1.2 Determining P_{in} from I_{out}

Since total power detectors only measure the Ith element of $\vec{S}_{out}$ it is impossible to use Equation 3.14 to ascertain P_{out}. Instead, we use the expression

$$P_{out} = \frac{I_{out}^{max} - I_{out}^{min}}{I_{out}^{max} + I_{out}^{min}} \tag{3.18}$$

to calculate the level of polarization. This expression will give the same result as Equation 3.14 for the ideal polarimeter with $\delta = \pi$. In this limit,

$$I_{out} = \frac{1}{2}\left[\, I_{in} + Q_{in}\cos(4\rho) + U_{in}\sin(4\rho) \,\right] \tag{3.19}$$

To find I_{out}^{max} and I_{out}^{min} we take the partial derivative of I_{out} with respect to ρ and set it equal to 0.

$$\frac{\partial I_{out}}{\partial \rho} = 2U_{in}\cos(4\rho) - 2Q_{in}\sin(4\rho) = 0 \tag{3.20}$$

By solving this equation, we find the maxima and minima in the data stream will appear at the HWP orientation angles

$$\rho_{max} = \tfrac{1}{4}\tan^{-1}\left(\tfrac{U_{in}}{Q_{in}}\right) \quad \text{and} \quad \rho_{min} = \tfrac{1}{4}\tan^{-1}\left(\tfrac{U_{in}}{Q_{in}}\right) + \tfrac{\pi}{4} \tag{3.21}$$

Substituting Equation 3.21 into Equation 3.19 yields

$$I_{out}^{max} = \tfrac{1}{2}\left(\, I_{in} + \sqrt{Q_{in}^2 + U_{in}^2} \,\right) \quad \text{and} \quad I_{out}^{min} = \tfrac{1}{2}\left(\, I_{in} - \sqrt{Q_{in}^2 + U_{in}^2} \,\right) \tag{3.22}$$

Finally, inserting Equation 3.22 into Equation 3.18 yields

$$P_{out} = \frac{I_{out}^{max} - I_{out}^{min}}{I_{out}^{max} + I_{out}^{min}} = \frac{\sqrt{Q_{in}^2 + U_{in}^2}}{I_{in}} = P_{in} \tag{3.23}$$

3.1.3 Interpreting P_{out} Measured by a Non-ideal Polarimeter

Now that we have demonstrated that Equation 3.18 is a tool that can be used to ascertain P_{in} given I_{out} for an ideal polarimeter, we apply the method to the more realistic and slightly more complicated expression, Equation 3.17, to determine the dependence of P_{out} on δ. Now we take the derivative of Equation 3.17, set it equal to zero

$$\frac{\partial I_{out}}{\partial \rho} = 2P_{in}\,\sin^2(\delta/2)\,[\cos(4\rho)\,\sin(2\theta) - \sin(4\rho)\,\cos(2\theta)\,] = 0 \tag{3.24}$$

and find the complete solution set for ρ to be

$$\tan(4\rho) = \tan(2\theta) \rightarrow \rho = \frac{\theta}{2} + \frac{n\pi}{4} \tag{3.25}$$

The first maxima will appear when $n = 0$ and the first minima when $n = 1$. Substituting these ρ values into Equation 3.17 we find

$$I_{out}^{max} = I_{out}\left(\rho = \frac{\theta}{2}\right) = \frac{1}{2}\left[\,1 + P_{in}\cos(2\theta)\cos^2(\delta/2) + P_{in}\sin^2(\delta/2)\,\right] \tag{3.26}$$

$$I_{out}^{min} = I_{out}\left(\rho = \left(\frac{\theta}{2} + \frac{\pi}{4}\right)\right) = \frac{1}{2}\left[\,1 + P_{in}\cos(2\theta)\cos^2(\delta/2) - P_{in}\sin^2(\delta/2)\,\right]$$

Substituting Equation 3.26 into Equation 3.18 yields the expression.

$$P_{out} = \frac{I_{out}^{max} - I_{out}^{min}}{I_{out}^{max} + I_{out}^{min}} = \frac{P_{in}\sin^2(\delta/2)}{1 + P_{in}\cos(2\theta)\cos^2(\delta/2)} \tag{3.27}$$

In the limit were $\delta = n\pi$, $P_{out} = P_{in}$. In all other cases $P_{out} \neq P_{in}$ and the polarimeter is therefore inefficient or non-ideal. We conclude that if Equation 3.18 is used on data produced by any real instrument, the result will contain some systematic error. This error can be accounted for if δ is known.

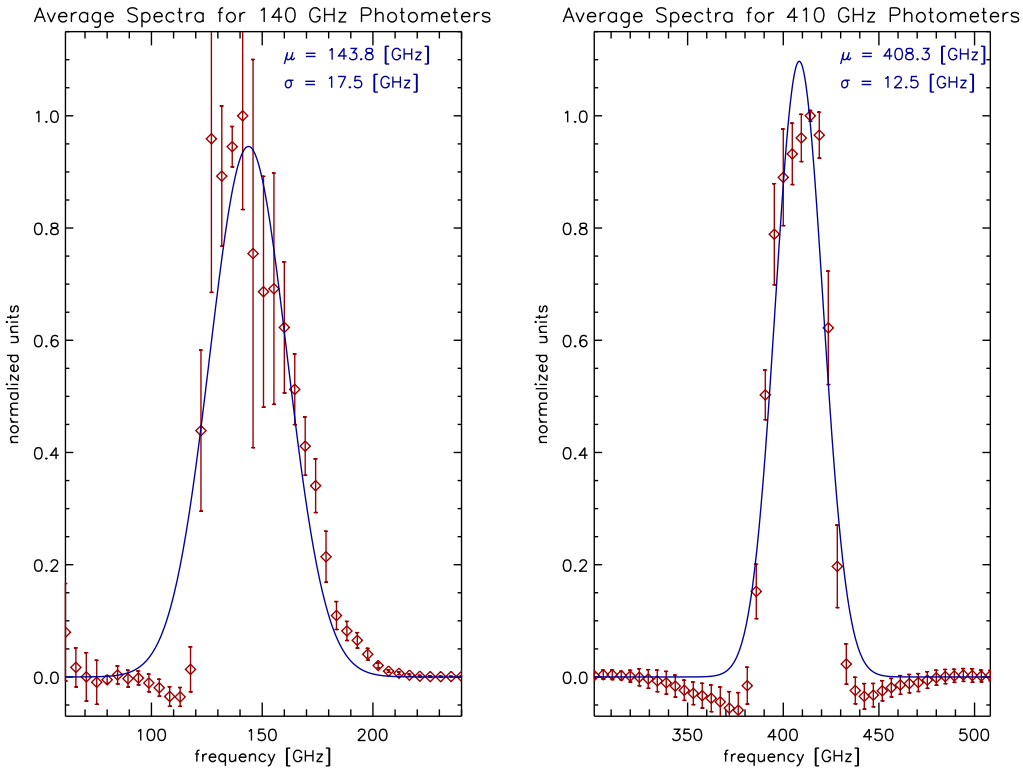

Figure 3.3: Average spectra for the 140 and 420 GHz photometers.

In fact, the MAXIPOL photometers have significant spectral breadth so δ is not single valued – it varies appreciably for one detector element. Figure 3.3 shows the combined spectra for six 140

GHz and four 420 GHz photometers. These spectra were measured with with a Fourier transform spectrometer at the University of California, Berkeley when the receiver was used for MAXIMA. Four additional 140 GHz photometers were added to the receiver for MAXIPOL. The spectra of these new photometers and the spectra of two inherited MAXIMA photometers have not been measured. All devices employ identical horns and filters so the performance of the unstudied photometers is expected to be very similar to the displayed measurements. When computing the combined spectrum, the individual spectra were normalized to their individual maximum, averaged together and then this combination was normalized. The 1-σ error in each bin illustrates the variance in the performace of the photometers at a given frequency. A Gaussian was fit to the average spectrum using a non-linear least-squares routine with no weighting so each band could be characterized completely with just two parameters, μ and σ. Clearly this fit is an approximation.

Using the Gaussian fit, P_{out} becomes

$$P_{out} = \frac{\frac{1}{\sigma_x\sqrt{2\pi}}\int_0^\infty e^{\frac{-(\nu-\mu_x)^2}{2\sigma_x^2}} P_{in}\sin^2\left(\delta(\nu)/2\right)\, d\nu}{\frac{1}{\sigma_x\sqrt{2\pi}}\int_0^\infty e^{\frac{-(\nu-\mu_x)^2}{2\sigma_x^2}} \left[1 + P_{in}\cos(2\theta)\cos^2\left(\delta(\nu)/2\right)\right]\, d\nu} \tag{3.28}$$

The subscript, x, can be valued 140 or 420. Notice δ is a function of the radiation frequency, ν, the spectral band term acts as a probability density, appropriately weighting the contribution of every frequency and the result is a function of crystal thickness, t. To elucidate the behavior of the solution, we set $P_{in} = 1$, $\theta = 0$ and μ and σ to the values gleaned by the Gaussian fits, and then we solved the integral numerically for the 140 and 420 GHz spectral bands. The results are plotted in Figure 3.4. The red dash and green dash-dot curves correspond to the solution of the integral for the 140 and 420 GHz spectral bands, respectively; the blue solid curve results from the multiplication of 140 and 420 GHz results. The optimal HWP thickness was chosen to be the the thickness value where the blue curve is maximized, 3.5 mm. The adjusted final thickness value of 3.4 mm resulted from fine corrections to the presented calculation that take into account the convergence of the incident radiation as it propagates through the sapphire crystal [34] (see Figure 2.7).

3.2 Anti-Reflection Coating and HWP Absorption

The HWP design calculations presented in Section 3.1 are somewhat idealized because they assume the transmission through the HWP is unity. In reality, as mentioned previously, there are significant secondary effects – reflections and absorption – that reduce the overall transmission and produce systematic errors that are large compared to the random error arising from the detector noise if

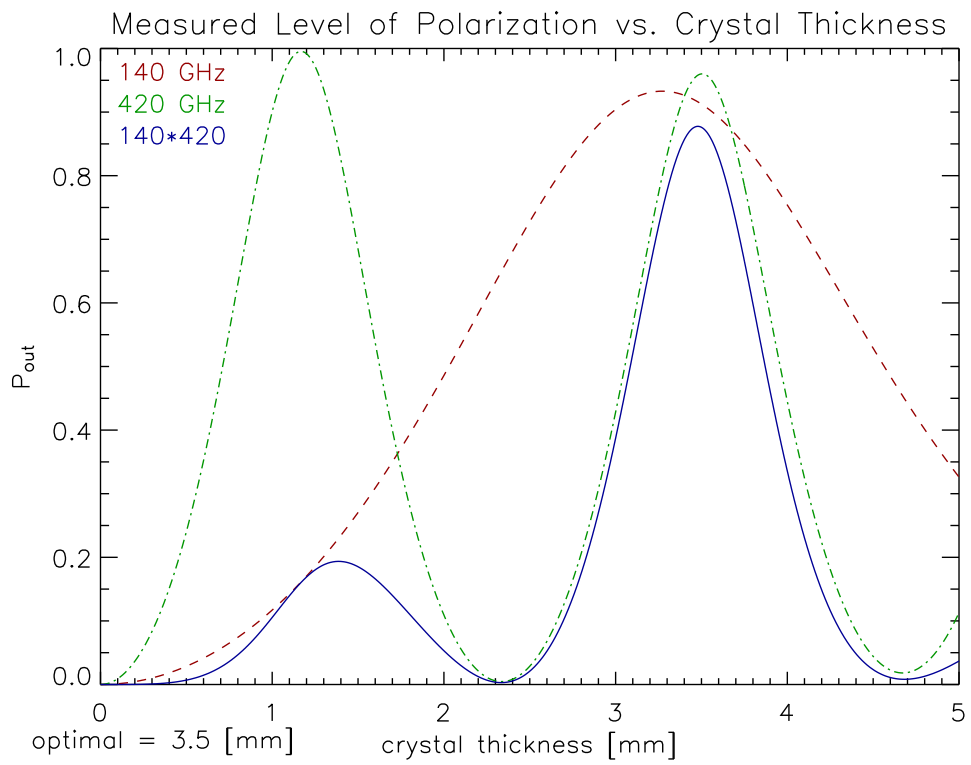

Figure 3.4: Expected polarimeter performance as a function of crystal thickness for the 140 (red dash) and 420 (green dash-dot) GHz MAXIPOL spectral bands. The blue solid curve results when the 140 and 420 GHz curves are multiplied. The optimal HWP thickness for the two frequency band experiment was computed to be 3.5 mm by finding the maximum of the blue solid curve.

Equation 3.18 is used to measure P_{in}. To assess the level of systematic error these secondary effects produce, we add more Mueller matrices to the calculations to make the resulting data stream model more accurate.

3.2.1 AR Coatings

Anti-reflection (AR) coatings are added at the HWP surfaces and modeled as non-ideal polarizers that rotate synchronously with the HWP. The transmission coefficients for these polarizers are set to $T^{ar}_{o,e} = 1 - R_{o,e}$ where

$$R_{o,e} = \frac{n_a^2(n - n_{o,e})^2 \cos^2(kh) + (nn_{o,e} - n_a^2)^2 \sin^2(kh)}{n_a^2(n + n_{o,e})^2 \cos^2(kh) + (nn_{o,e} + n_a^2)^2 \sin^2(kh)} \tag{3.29}$$

Here, k is the free space propagation number for the radiation, $k = 2\pi/\lambda$, n, n_a and $n_{o,e}$ are the indices of refraction for free space, the AR coating material and sapphire, respectively and $h = n_a d$

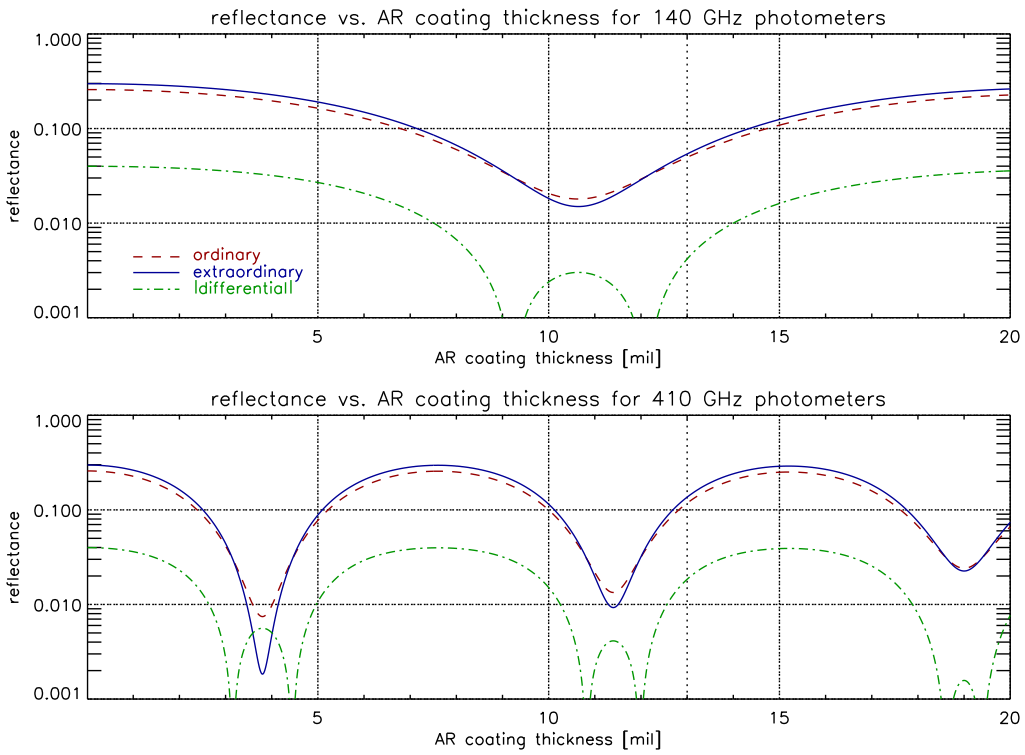

Figure 3.5: Total reflectance and differential reflectance for sapphire AR coated with Herasil assuming the Gaussian spectral bands plotted in Figure 3.3. The reflectance is plotted versus AR coating thickness in mil (thousandths of an inch). Results for the 140 and 420 GHz photometers are plotted in the top and bottom panel, respectively.

where d is the thickness of the AR coating [32]. This expression is completely general. If d is set to 0 then R simplifies to

$$R_{o,e} = \frac{(n - n_{o,e})^2}{(n + n_{o,e})^2} \tag{3.30}$$

and we are purely considering reflections produced at the free space/sapphire interface. Conversely, if d is set to $\lambda/4$ and $n_a^2 = n n_{o,e}$ then R vanishes and $T = 1$ – the added AR coating completely eliminates all reflections. To make this AR prescription work for the HWP however, one needs to use a birefringent material for the AR coating because the sapphire is birefringent. This material must have $n_{ao} = \sqrt{n_o}$ and $n_{ae} = \sqrt{n_e}$. A material with birefringent characteristics that match sapphire in this way is not known to exist .

The thickness of a single layer AR coating is tuned to perform perfectly for only one frequency and its harmonics – so inside a typical MAXIPOL photometer band, the coating acts like a monochromatic device. Broadband AR coating technologies are known to exist [35]. However, designing a device that survives physically in the the 4 K environment while performing effectively in both frequency bands proved to be be a longer time scale endeavor than the MAXIPOL program itself.

Future CMB polarization experiments will likely employ broadband AR coatings. For MAXIPOL we decided to use a single layer non-birefringent AR coating constructed from 0.013 inch thick Herasil, which is made from fused quartz. To calculate the total and differential reflectance, we computed numerically the integral

$$R_{o,e}^{total} = \frac{1}{\sigma_x\sqrt{2\pi}} \int_0^\infty e^{\frac{-(\nu-\mu_x)^2}{2\sigma_x^2}} R_{o,e}(\nu)\, d\nu \tag{3.31}$$

where x again is either 140 or 420 and μ_x and σ_x are taken from the fits in Figure 3.3. The result, which is plotted in Figure 3.5, is a function of AR coating thickness. The blue solid curve and the red dash curve in both panels illustrate the total reflectance from the extraordinary and ordinary axes, respectively. The green dash-dot curve is the absolute value of the difference of the o and e curves. A vertical dotted line plotted at 13 thousandths of an inch marks the MAXIPOL AR coating thickness. This thickness was selected to match the intersection where $R_o^{total} = R_e^{total}$ in the 140 GHz plot. Figure 3.5 suggests the intersection occurs closer to 0.012 inches. The decision to use a 0.013 inch thick coating instead of 0.012 inch was based on a correction to this calculation that takes into account the convergence of the radiation as it passes through the HWP [34].

3.2.2 Absorption

The differential absorption in the sapphire can be modeled similarly. Here,

$$T_{o,e}^a = e^{-\alpha_{o,e} t} \tag{3.32}$$

$\alpha_{o,e}$ is the absorption coefficient and t is the thickness of the HWP. The Mueller matrix for both phenomena is defined as

$$\hat{\mathcal{M}}_x = \frac{1}{2} \begin{bmatrix} r_{00} & r_{01} & r_{02} & r_{03} \\ r_{10} & r_{11} & r_{13} & r_{14} \\ r_{20} & r_{21} & r_{21} & r_{23} \\ r_{30} & r_{31} & r_{32} & r_{33} \end{bmatrix} \tag{3.33}$$

where x is a generic subscript/superscript that can be replaced with either a for HWP absorption or ar for AR coating. The matrix elements are defined

$$\begin{aligned} r_{00} &= (T_o^x + T_e^x) \\ r_{01} &= (T_o^x - T_e^x)\ \cos(2\rho) \\ r_{02} &= (T_o^x - T_e^x)\ \sin(2\rho) \\ r_{03} &= 0 \\ r_{10} &= (T_o^x - T_e^x)\ \cos(2\rho) \end{aligned}$$

$$
\begin{aligned}
r_{11} &= (T_o^x + T_e^x)\ \cos^2(2\rho) + 2\sqrt{T_o^x T_e^x}\ \sin^2(2\rho) \\
r_{12} &= \left((T_o^x + T_e^x) - 2\sqrt{T_o^x T_e^x} \right)\ \cos(2\rho)\ \sin(2\rho) \\
r_{13} &= 0 \\
r_{20} &= (T_o^x - T_e^x)\ \sin(2\rho) \\
r_{21} &= \left((T_o^x + T_e^x) - 2\sqrt{T_o^x T_e^x} \right)\ \cos(2\rho)\ \sin(2\rho) \\
r_{22} &= (T_o^x + T_e^x)\ \sin^2(2\rho) + 2\cos^2(2\rho)\ \sqrt{T_o^x T_e^x} \\
r_{23} &= 0 \\
r_{30} &= 0 \\
r_{31} &= 0 \\
r_{32} &= 0 \\
r_{33} &= 2\sqrt{T_o^x T_e^x}
\end{aligned}
$$

3.2.3 Data Stream Model with Absorption and Reflection

Again, the data stream is the Ith element of $\vec{S}_{out}$

$$\hat{\mathcal{M}}_p\ \hat{\mathcal{M}}_{ar}\ \hat{\mathcal{M}}_a\ \hat{\mathcal{M}}_h\ \hat{\mathcal{M}}_{ar}\ \vec{S}_{in} = \vec{S}_{out} \tag{3.34}$$

Here the Mueller matrix for the polarizer is defined

$$\hat{\mathcal{M}}_p = \frac{1}{2}\begin{bmatrix} p_x^2 + p_y^2 & p_x^2 - p_y^2 & 0 & 0 \\ p_x^2 - p_y^2 & p_x^2 + p_y^2 & 0 & 0 \\ 0 & 0 & 2p_x p_y & 0 \\ 0 & 0 & 0 & 2p_x p_y \end{bmatrix} \tag{3.35}$$

If we have the ideal case where $T_{o,e}^x = 1$, $\delta = \pi$, $p_x = 1$ and $p_y = 0$ then it is easy to show that $\vec{S}_{out}^1$ equals Equation 3.19. However, any real system is non-ideal so it is beneficial to understand analytically how the known realistic phenomena impact the overall polarimeter inefficiency. The analytical calculation is quite tedious. Since we know *a priori* that the differential absorption is negligibly small, we will ignore its contribution going forward. As a result, consider this expression instead.

$$\hat{\mathcal{M}}_p\ \hat{\mathcal{M}}_{ar}\ \hat{\mathcal{M}}_h\ \hat{\mathcal{M}}_{ar}\ \vec{S}_{in} = \vec{S}_{out} \tag{3.36}$$

Omitting several intermediate steps, the result emerges

$$I_{out} = I_{out}^o + I_{out}^{2\rho} + I_{out}^{4\rho} \tag{3.37}$$

$$
\begin{aligned}
I^{o}_{out} &= \frac{I_{in}}{4}(p_x^2+p_y^2)(T_o^2+T_e^2)+\frac{Q_{in}}{8}(p_x^2-p_y^2)\left[\ (T_o^2+T_e^2)+2T_oT_e\cos(\delta)\ \right] \qquad (3.38)\\
I^{2\rho}_{out} &= \frac{1}{4}\,(T_o^2-T_e^2)\left[\ \left(I_{in}\,(p_x^2-p_y^2)+Q_{in}\,(px^2+p_y^2)\right)\cos(2\rho)+U_{in}\,(p_x^2-p_y^2)\sin(2\rho)\ \right]\\
I^{4\rho}_{out} &= \frac{1}{8}\,(p_x^2-p_y^2)\left[\ (T_o^2+T_e^2)-2T_oT_e\cos(\delta)\ \right]\left(\ Q_{in}\cos(4\rho)+U_{in}\sin(4\rho)\ \right)
\end{aligned}
$$

3.3 Polarimeter Efficiency

To ascertain the polarimeter performance, we measured a linearly polarized load in the lab before flight. This load was comprised of a container lined with 2 inch thick Eccosorb LS-14 “egg crate” foam and filled with ice water. Thermal radiation emanating from this source was then chopped with an ambient temperature aluminum chopper blade coated with 0.25 inch thick Eccosorb LS-14 foam sheets; the chop frequency was set to ∼6.5 Hz. The signal was then linearly polarized with a wire-grid polarizer mounted to the cryostat window with hardware specifically designed to allow polarizer rotation and prohibit by-pass leakage. The polarizer was fabricated by Buckbee-Mears and constructed from electroformed 0.0002 inch diameter gold wires bonded to 0.0015 inch thick Mylar film at 250 lines per inch. Using Equation 3.15 and the results in Table 3.3 we determined these grids produce 96.6% polarized radiation at 140 GHz (Section 3.4). The transmission axis of the window polarizer was aligned to within three degrees of the the transmission axis of the focal plane polarizer. This alignment was difficult because it was impossible to manipulate both pieces of hardware concurrently as the focal plane polarizer was sealed inside the receiver and cooled to 4 K long before the window polarizer was installed. To solve this problem we aligned both elements to within one degree of the symmetry plane of the receiver knowing that any movement of the focal plane polarizer arising from thermal contraction as the innards of the receiver cooled to 4 K would produce an error in this measurement – the three degree uncertainty mentioned above represents a conservative estimate and not a measurement. During data collection, the HWP orientation was then discretely stepped by hand in ∼5° intervals. Roughly twenty seconds of data were collected at each HWP position.

The source was chopped for two primary reasons. First, the photometer output has significant 1/f noise so the I term in Equation 3.19 is corrupted by noise drifts. Second, the primary detector outputs are AC coupled so the gain before the ADC can be maximized. As a result, the I term is in fact discarded. Photometer output that is not AC coupled is available however it suffers from the aforementioned low frequency noise and the gain before the ADC is smaller by a factor of ∼36 so the voltages recorded are not as precise. The upshot is the chopped source adds a tractable layer of complexity to the data analysis but produces the most accurate results.

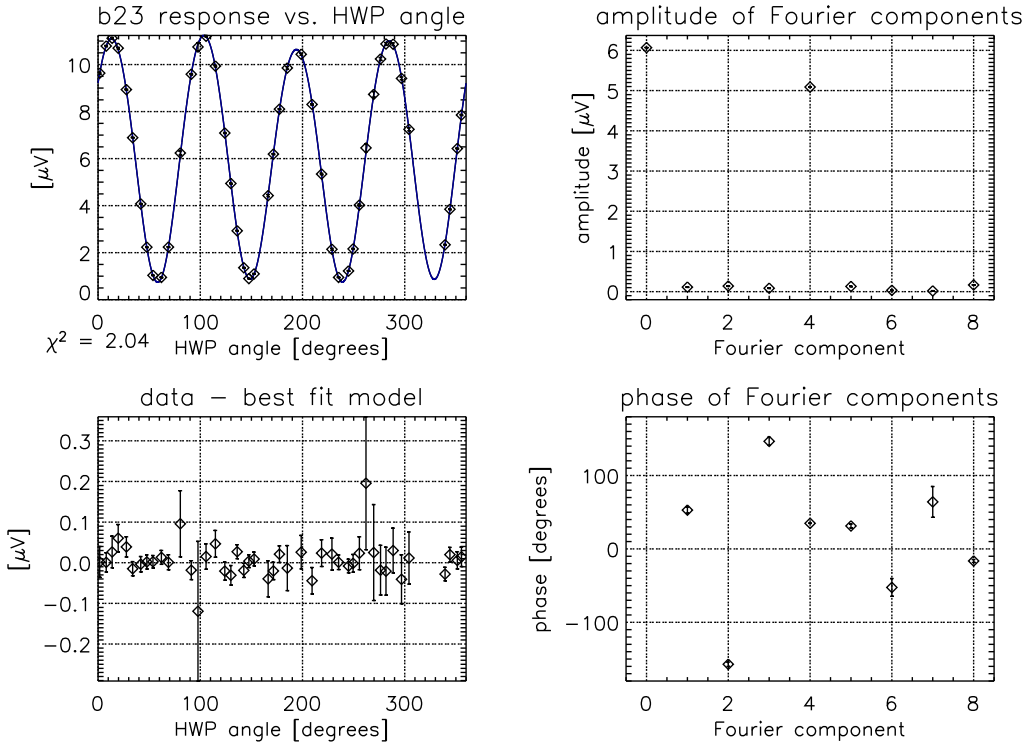

Figure 3.6: A lab measurement of a 96.6% linealy polarized load. This measurement was made to assess the polarimeter performance (see Section 3.3).

3.3.1 Chopped Source

Assuming we are analyzing the detector output from an ideal HWP polarimeter (Equation 3.19), the extremum of the amplitude of the chopped signal equals

$$A_{chop}^{max} = \frac{1}{2}\left[\frac{1}{2}\left(I_{300} + \sqrt{Q_{300}^2 + U_{300}^2} \right) - \frac{1}{2}\left(I_{273} + \sqrt{Q_{273}^2 + U_{273}^2} \right)\right]$$
$$A_{chop}^{min} = \frac{1}{2}\left[\frac{1}{2}\left(I_{300} - \sqrt{Q_{300}^2 + U_{300}^2} \right) - \frac{1}{2}\left(I_{273} - \sqrt{Q_{273}^2 + U_{273}^2} \right)\right] \tag{3.39}$$

The subscripts 300 and 273 correspond to the ∼300 K chopper blade and the 273 K ice bath, respectively. Applying these terms to Equation 3.18 yields

$$\frac{A_{chop}^{max} - A_{chop}^{min}}{A_{chop}^{max} + A_{chop}^{min}} = \frac{\sqrt{Q_{300}^2 + U_{300}^2} - \sqrt{Q_{273}^2 + U_{273}^2}}{I_{300} - I_{273}} \tag{3.40}$$

This expression can be simplified using the knowledge that both temperatures are polarized equally

$$P = \frac{\sqrt{Q_{300}^2 + U_{300}^2}}{I_{300}} = \frac{\sqrt{Q_{273}^2 + U_{273}^2}}{I_{273}} \qquad \rightarrow \qquad I_{300} = I_{273}\frac{\sqrt{Q_{300}^2 + U_{300}^2}}{\sqrt{Q_{273}^2 + U_{273}^2}} \tag{3.41}$$

By substituting Equation 3.41 into Equation 3.40 we show that it is possible to measure P_{in} with the chopped source.

$$P_{out} = \frac{A_{chop}^{max} - A_{chop}^{min}}{A_{chop}^{max} + A_{chop}^{min}} = \frac{\sqrt{Q_{273}^2 + U_{273}^2}}{I_{273}} = P_{in} \tag{3.42}$$

3.3.2 Data Analysis

To glean the amplitude of the chopped signal from the data, we used an analysis technique inspired by the lock-in amplifier. The time ordered data associated with one HWP orientation were extracted from the full data set and a third degree polynomial was fit to this subset and subtracted to remove any drifts in the data stream. Here we used a least-square polynomial fit with no weighting. This subtraction is not necessary for the lock-in operation itself. However, because this is a finite, discretely sampled data set, the offset and drift subtraction becomes important because the endpoints of the data stream must be compatible to reduce ringing when the data is Fourier transformed to the frequency domain for low-pass filtering and because the data will be used to create the lock-in reference so it must have mean zero. Now we create this lock-in reference.

$$r_i = \begin{cases} 1 & \text{for} \quad \{i : d_i \geq 0\} \\ -1 & \text{for} \quad \{i : d_i < 0\} \end{cases} \tag{3.43}$$

This prescription produces a square wave reference which will yield accurate results if the data is a square wave as well. In reality the chopper blade produces a quasi-square-wave signal because the transit time for the blade edge to cross the photometer beam is appreciable. As a result, the measured amplitude will be off by some small factor. This fact is insignificant because all amplitudes will be effected equally so the factor disappears when P_{out} is computed (see Equation 3.42). Now we forward FFT the data times the reference

$$\widetilde{d}_k = \frac{1}{N} \sum_{i=0}^{N-1} d_i \, r_i \, e^{-i2\pi ki/N} \tag{3.44}$$

filter and then reverse FFT back to the time domain

$$d_i^{\mathcal{F}} = \mathrm{Re} \left(\sum_{k=0}^{N-1} \widetilde{d}_k \, \mathcal{F}_k \, e^{i2\pi ki/N} \right) \tag{3.45}$$

The cutoff frequency of this square low-pass filter is designed to eliminate signals at harmonics of the chop frequency greater than the Nyquist frequency that get aliased to just over 2 Hz.

$$\mathcal{F}_k = \begin{cases} 1 & \text{for} \quad \{k : |f_k| \leq 2\} \\ 0 & \text{for} \quad \{k : |f_k| > 2\} \end{cases} \tag{3.46}$$

Here we use the FFT storage scheme where the frequency associated with any FFT bin indexed by k is

$$f_k = \frac{k}{N\,\Delta t} \quad \text{for} \quad k = 0, 1, \cdots, \frac{N}{2} \tag{3.47}$$

$$f_{N-k} = \frac{-k}{N\,\Delta t} \quad \text{for} \quad k = 1, 2, \cdots, \frac{N}{2} - 1 \tag{3.48}$$

The chop amplitude and its error is computed at each HWP orientation using the standard equations.

$$\mu_\rho = \frac{1}{N}\sum_{i=0}^{N-1} d_i^{\mathcal{F}} \qquad \text{and} \qquad \sigma_\rho = \sum_{i=0}^{N-1} \frac{(d_i^{\mathcal{F}} - \mu)^2}{N-1} \tag{3.49}$$

The results from one photometer are presented in Figure 3.6. The chop amplitude versus HWP orientation angle is plotted in the upper left panel. The blue curve overplotted is an eight sine wave model fit to the data using a non-linear least squares routine employing a gradient expansion algorithm with convergence criteria set to $\Delta\chi^2 = 10^{-6}$. The amplitude and phase of each of the eight Fourier components is plotted in the upper and lower right, respectively. Clearly the dominant signals are an offset and a $\cos(4\rho)$ signal – which is the result expected. The data minus the model is plotted in the lower left to elucidate the error bars and the goodness of fit of the model. The error bar resulting from this lock-in calculation is smaller than the nominal noise rms because the filter used rejects 98% of the bandwidth. The filtering process also strongly correlates the remaining noise so $d_i^{\mathcal{F}}$ is not simply an array of uncorrelated Gaussian random variables.

We computed P_{out} using the fit parameters and their associated errors. For this calculation,

$$\begin{aligned} A_{chop}^{max} &= \xi + A_{4\rho} \\ A_{chop}^{min} &= \xi - A_{4\rho} \\ P_{out} &= \frac{A_{chop}^{max} - A_{chop}^{min}}{A_{chop}^{max} + A_{chop}^{min}} = \frac{A_{4\rho}}{\xi} \end{aligned} \tag{3.50}$$

where $A_{4\rho}$ is the amplitude of the $\cos(4\rho)$ Fourier component and ξ is the offset. We calculated P_{out} with $A_{4\rho}$ only because in principle all other signals should be spurious. Assuming normal incidence, $P_{in} = 0.966$ and $T_x = 1$ and $T_y = 0.0174$ for the focal plane polarizer, P_{out} should equal 0.857 for this measurement for the 140 GHz photometers. This prediction was calculated using a rederivation of Equation 3.27 seeded by Equation 3.13 rather than Equation 3.17. In practice, a significant fraction of the radiation has a non-normal incidence angle so the expected P_{out} should be smaller than 0.857. The results computed from the data are presented in Table 3.1. The error reported is only statistical. A systematic error in the measurement expected to be much larger than the statistical error results from a responsivity variation that is synchronous with the HWP orientation. The results and predictions match closely given the uncertainties in both. Data analysis is ongoing.

Photometer	Amplitude of cos(4x)	Phase of cos(4x)	Offset	P_{out}
b13	5.517±0.006	-141.15±0.08	6.883±0.005	0.801±0.001
b14	3.236±0.005	36.61±0.10	3.915±0.004	0.827±0.002
b15	6.754±0.007	-146.28±0.07	8.597±0.005	0.786±0.001
b23	5.089±0.007	34.84±0.09	6.068±0.005	0.839±0.001
b24	3.860±0.005	34.15±0.11	4.815±0.004	0.802±0.001
b25	5.739±0.010	35.63±0.13	7.234±0.007	0.793±0.002
b33	6.138±0.008	33.13±0.08	7.410±0.006	0.828±0.001
b34	4.771±0.006	37.39±0.07	5.793±0.004	0.824±0.001
b35	5.291±0.008	41.17±0.09	6.491±0.005	0.815±0.001
b43	5.071±0.008	30.39±0.09	5.032±0.006	1.008±0.002
b44	3.562±0.012	35.53±0.24	4.329±0.010	0.823±0.003
b45	3.254±0.004	42.85±0.08	4.185±0.003	0.777±0.001

Table 3.1: P_{out} calculated from the fit parameters measured using the technique illustrated in Figure 3.6. Only statistical error is reported. P_{out} is expected to be 0.857 assuming normal incidence, $P_{in} = 0.966$ and $T_x = 1$ and $T_y = 0.0174$ for the focal plane polarizer.

3.4 Wire Grid Polarizers

We characterized the Buckbee-Mears wire-grid polarizers with a measurement using the MAXIPOL receiver. For this test, a rotating polarizer was mounted in the optical path at the cryostat window and the chopped load described in Section 3.3 was placed just outside the cryostat window near the prime focus of the telescope; the thermal radiation from this source completely filled the beam. No HWP was present for this measurement. The linearly polarized signal produced by the combination of these two devices was analyzed with the nominal focal plane polarizer. The rotating polarizer was stepped discretely in 11.4° steps; 2 seconds of data were collected at each orinetation. The amplitude of the chopped signal was ascertained using the software lock-in amplifier technique described in Equations 3.43 to 3.46.

Using Mueller matrix algebra, we calculated that the anticipated signal for this test should be the Ith term of $\vec{S}_{out}$.

$$\hat{\mathcal{M}}_p^{fp}\ \hat{\mathcal{M}}_p^{w}\ \vec{S}_{in} = \vec{S}_{out} \tag{3.51}$$

The static focal plane polarizer is described by the matrix

$$\hat{\mathcal{M}}_p^{fp} = \frac{1}{2}\begin{bmatrix} T_x + T_y & T_x - T_y & 0 & 0 \\ T_x - T_y & T_x + T_y & 0 & 0 \\ 0 & 0 & 2\sqrt{T_x T_y} & 0 \\ 0 & 0 & 0 & 2\sqrt{T_x T_y} \end{bmatrix} \tag{3.52}$$

while the rotating polarizer at the cryostat window, $\hat{\mathcal{M}}_p^w$, is described by

$$\hat{\mathcal{M}}_p^w = \frac{1}{2}\begin{bmatrix} r_{00} & r_{01} & r_{02} & r_{03} \\ r_{10} & r_{11} & r_{13} & r_{14} \\ r_{20} & r_{21} & r_{21} & r_{23} \\ r_{30} & r_{31} & r_{32} & r_{33} \end{bmatrix} \tag{3.53}$$

with the matrix elements defined

$$\begin{aligned}
r_{00} &= (T_x + T_y) \\
r_{01} &= (T_x - T_y)\ \cos(2\alpha) \\
r_{02} &= (T_x - T_y)\ \sin(2\alpha) \\
r_{03} &= 0 \\
r_{10} &= (T_x - T_y)\ \cos(2\alpha) \\
r_{11} &= (T_x + T_y)\ \cos^2(2\alpha) + 2\sqrt{T_x T_y}\ \sin^2(2\alpha) \\
r_{12} &= \left((T_x + T_y) - 2\sqrt{T_x T_y} \right)\ \cos(2\alpha)\ \sin(2\alpha) \\
r_{13} &= 0 \\
r_{20} &= (T_x - T_y)\ \sin(2\alpha) \\
r_{21} &= \left((T_x + T_y) - 2\sqrt{T_x T_y} \right)\ \cos(2\alpha)\ \sin(2\alpha) \\
r_{22} &= (T_x + T_y)\ \sin^2(2\alpha) + 2\cos^2(2\alpha)\ \sqrt{T_x T_y} \\
r_{23} &= 0 \\
r_{30} &= 0 \\
r_{31} &= 0 \\
r_{32} &= 0 \\
r_{33} &= 2\sqrt{T_x T_y}
\end{aligned}$$

Setting $\vec{S}_{in} = [\ \Delta I_{in},\ 0,\ 0,\ 0\ ]$, the Ith element of $\vec{S}_{out}$ becomes

$$I_{out} = \frac{1}{4}\Delta I_{in}\left[(T_x + T_y)^2 + (T_x - T_y)^2\cos(2\alpha)\right] \tag{3.54}$$

ΔI_{in} is the intensity difference between the two thermal sources in the chopped signal, T_x and T_y are the intensity transmission coefficients for the polarizer and α is the rotating polarizer orientation angle. Notice Equation 3.53 is the same as Equation 3.35 if $T_x = p_x^2$ and $T_y = p_y^2$. Clearly there should only be a $\cos(2\alpha)$ signal in the data. If the raw data is analyzed however, we find a small but detectable amount of $\cos(4\alpha)$ signal in addition to the large $\cos(2\alpha)$ signal. This harmonic distortion results from the fact that the responsivity of the bolometers varies as the radiative load varies with α. Using our knowledge of the thermal properties of the detectors, we can back out the

$\overline{G}$	Δ	R_o	R_{load}	V_{bias}	T_b	δ	g
70 [pW/K]	14.4 [K]	120 [Ω]	160 [MΩ]	70 [mV]	0.105 [K]	-0.201 [V]	1800

Table 3.2: Bolometer parameter values used to correct the wire-grid polarizer measurements.

varying responsivity effect and obtain a more accurate result. Using these equations, we can solve for the bolometer absorber temperature, T.

$$\frac{V_{bolo} - \delta}{g} = I_{bias}\ R_o\ e^{\sqrt{\frac{\Delta}{T}}} \qquad \text{where} \qquad I_{bias} = \frac{V_{bias}}{R_{load} + R_o\ e^{\sqrt{\frac{\Delta}{T}}}} \tag{3.55}$$

V_{bolo} is the detector output, δ is a small offset introduced by the amplifiers in the readout electronics, g is a gain factor, R_o and Δ are parameters that define the shape of the temperature dependence of the thermistor resistance, V_{bias} is the rms of the AC bias voltage and R_{load} is a load resistance in series with the bolometer. $R_{load} \gg R_{bolo}$ so the bias current, I_{bias}, is constant. Once we have the absorber temperature, we can calculate the absolute power absorbed by the detector.

$$P_o = \overline{G}\,(T - T_b) - I_{bias}^2\, R_o\, e^{\sqrt{\frac{\Delta}{T}}} \tag{3.56}$$

$\overline{G}$ is the average thermal conductance between the absorber and the bath and T_b is the bath temperature. The parameter values used in this calculation are displayed in Table 3.2. The corrected and normalized results are plotted in the upper left panel of Figure 3.7. Each bin value represents the average of the data stream collected at each polarizer orientation post lock-in and the error bar (smaller than the symbol) represents the standard deviation. Lock-in details are discussed in Section 3.3.2. The error bars in the bins are smaller than the nominal detector noise rms because the low-pass filter in the software lock-in removes 99.6% of the bandwidth (sample period, Δt = 0.98 ms, $f_{Nyquist}$ = 510 Hz and the square, low-pass filter cutoff = 2 Hz). The filtering process also strongly correlates the remaining noise so $d_i^{\mathcal{F}}$ is not simply an array of uncorrelated Gaussian random variables.

A model comprised of eight sine waves and an offset was fit to the data using a non-linear least-squares routine. The fit was weighted by the standard deviation in each bin and the convergence criteria was set to $\Delta\chi^2 = 1 \times 10^{-6}$. For the model, the angular frequency of the eight sine waves was fixed to the first eight harmonics of the angular frequency of the polarizer and the amplitude and phase for each sine wave was allowed to vary so overall there were 17 free parameters. The fit amplitudes and phases are plotted in the upper right and lower right panels of Figure 3.7, respectively, while the binned data minus the best fit model is plotted in the lower left. The amplitudes of the $\sin(\rho)$, $\sin(3\rho)$, $\sin(5\rho)$, $\sin(6\rho)$, $\sin(7\rho)$ and $\sin(8\rho)$ components are consistent with zero to 1-σ. The $\sin(4\rho)$ component has a residual amplitude after the correction of 0.005 $\pm$

0.001 in normalized units – which is inconsistent with zero. However, this signal is three orders of magnitude smaller than the $cos(2\rho)$ component so it doesn't effect the result significantly.

Plugging Equation 3.54 into Equation 3.18 we see that

$$P_{out} = \frac{(T_x - T_y)^2}{(T_x + T_y)^2} \tag{3.57}$$

Assuming that the transmission along the principal transmission axis of the polarizer, $T_x = 1$ then

$$T_y = \frac{1 - \sqrt{P_{out}}}{1 + \sqrt{P_{out}}} \tag{3.58}$$

P_{out} was determined from the data to be 0.933 ± 0.003 which means one grid produces 96.6% linearly polarized radiation. The resulting measured transmission parameters for 140 GHz radiation are listed in Table 3.3.

	x	y
amplitude attenuation coefficients, p	1	0.132 ± 0.003
intensity transmission coefficients, T	1	0.0174 ± 0.0007

Table 3.3: Amplitude attenuation and intensity transmisson coefficiense for the Buckbee-Mears wire-grid polarizers ascertained by measurements at 140 GHz.

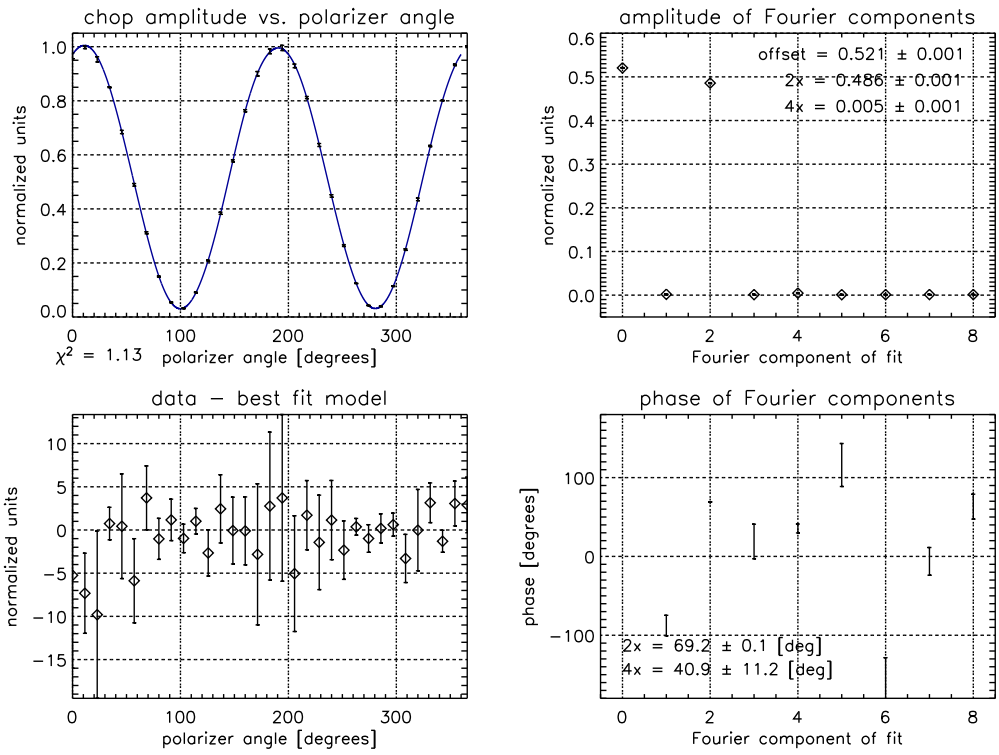

Figure 3.7: A characterization of the wire-grid polarizer used in the MAXIPOL receiver.

Chapter 4

The MAXIPOL Flights

Figure 4.1: The MAXIPOL payload on the launch pad at the National Scientific Ballooning Facility in Ft. Sumner, New Mexico in September 2002.

4.1 MAXIPOL-0

During the ∼22 hour MAXIPOL-0 flight the NASA data transmitter failed sporadically because of a broken solder connection. As a result, only a few ∼10 minute sections of bolometer data were successfully recorded; we did not realize enough integration time for CMB measurements. The flight did provide us with the opportunity to check the in-flight polarimeter performance and to test the new daytime pointing camera, the sun shielding strategy and the HWP driveshaft motor and encoder. The flight trajectories and altitude profiles for MAXIPOL-0 and MAXIPOL-1 are illustrated in Figure 4.2.

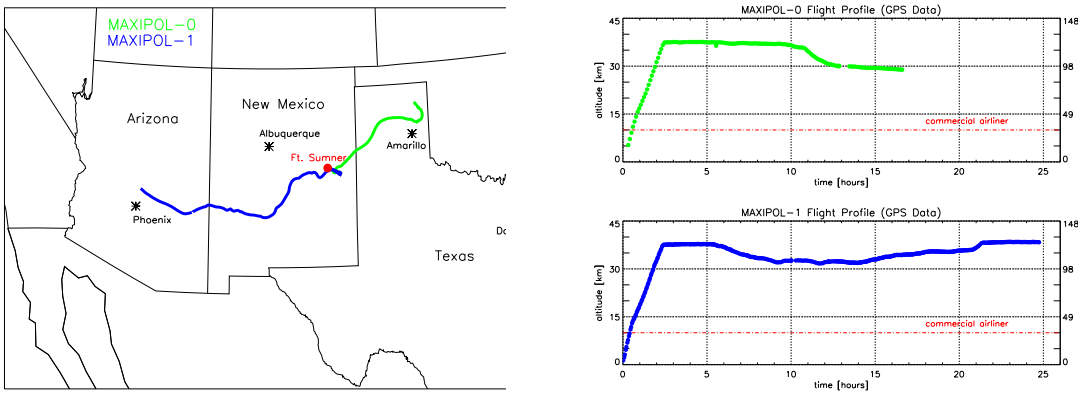

Figure 4.2: MAXIPOL-0 and MAXIPOL-1 flight trajectories and altitude profiles.

4.2 MAXIPOL-1

During the MAXIPOL-1 flight, we executed four different types of telescope scans: a planet scan, a dipole scan, a CMB scan and a foreground dust scan.

During the planet scan, the gondola yawed sinusoidally 2.5° peak-to-peak in azimuth at a slowly-rising elevation for ∼1 hour. The scan period was 18 seconds. During this time, Jupiter passed through the field-of-view of the instrument and was detected by the bolometers. This data set will be used to map the beam shape of each photometer and calibrate the bolometer time streams given the known millimeter-wave intensity of Jupiter. We performed both daytime and nighttime observations of Jupiter.

The CMB dipole was scanned by rotating the gondola 360° in azimuth while holding the telescope at a constant elevation of 36° for 22 minutes. A second ∼10 minute scan was performed at an elevation of 50°. The period of a single rotation was 18 seconds. With this data set we will calibrate the bolometer time streams given the large, known CMB dipole signal.

For the CMB and dust scans, the telescope tracked a guide star as it swept across the sky. Simultaneously, the gondola yawed 2° peak-to-peak in azimuth with a period of 10 seconds. This telescope motion combined with the inherent sky rotation produced bow tie shaped maps. To improve cross-linking, the telescope elevation dithered periodically about the elevation of the guide star by ± 0.2° with an elevation change occurring every 10 minutes. Table 4.1 summarizes the scan length and the expected dust contribution for the five regions observed during MAXIPOL-1. Regions with strong dust contamination will be used to characterize this foreground signal.

	Observation Length in [hours]	Average Dust Level [μK]	RMS Dust Level [μK]
Beta Ursae Minoris	7.5	20	3.2
Polaris	2.25	173	23
Gamma Urase Majoris	2.5	11	2.5
Gamma Virgo	0.5	22	3.2
Arcturus	2.0	27	5.1

Table 4.1: MAXIPOL-1 scan regions. Five bow tie shaped regions of the sky were mapped during MAXIPOL-1 by tracking five different guide stars. The observation length and the expected dust contribution for each region [26] is presented.

To monitor the bolometer temperature dependence of the calibration, a fixed intensity millimeter-wave lamp mounted near the focal plane was switched on for 10 seconds every 22 minutes. The relationship between the magnitude of the subsequent bolometer response and the known bolometer temperature will be ascertained during data analysis. The responsivity of each bolometer sample will be interpolated given this relative calibration and the absolute Jupiter and CMB dipole calibrations.

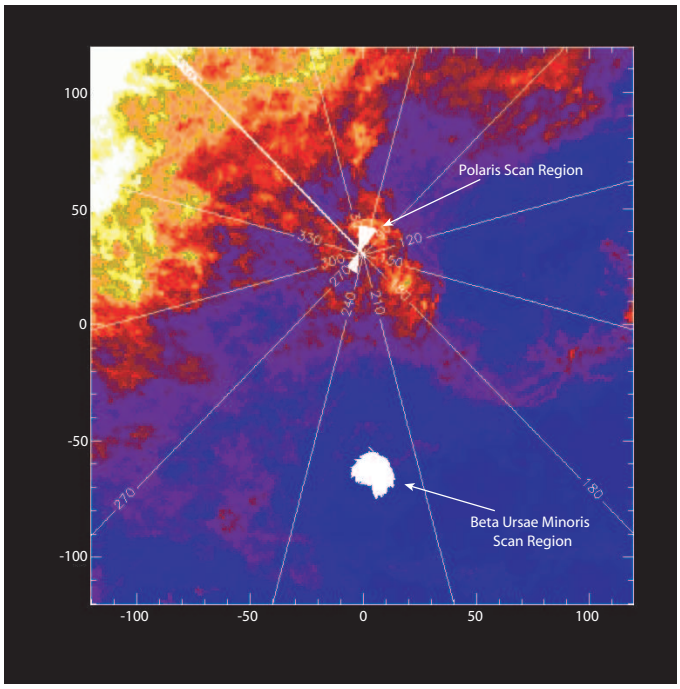

Figure 4.3: 150 GHz SFD dust map with primary MAXIPOL scan regions overplotted.

Chapter 5

Data Analysis

5.1 Introduction

The raw data stream emerging from the MAXIPOL instrument can be written

$$d_i = s_i + n_i + h_i + g_i \tag{5.1}$$

where s is the sky signal we are in search of, n is Gaussian random noise, h is a HWP-synchronous instrumental signal, g is a spurious signal produced by transients and i is the index number of the discretely sampled data. Ultimately we want to unambiguously distinguish s from n, h and g. Transients are easily identifiable so they are masked from the data stream using the procedure detailed in Section 5.2. The instrumental signal is estimated using the procedure described in Section 5.4 and then this estimate is subtracted from the data stream yielding

$$d_i = s_i + n_i + h_i - \hat{h}_i = s_i + n_i \tag{5.2}$$

if $h = \hat{h}$ where $\hat{h}$ is the estimated instrumental signal. In practice, $h \neq \hat{h}$ exactly. Therefore, Section 5.4 will also discuss the systematic error the $\hat{h}$ estimator introduces. Once Equation 5.2 is obtained, the data is binned to form a pixelized sky map where the pixel value,

$$m_p = \frac{1}{N'} \sum_{i'=0}^{N'-1} d_{i'} \tag{5.3}$$

the pixel variance,

$$v_p = \sum_{i'=0}^{N'-1} \frac{(d_{i'} - m_p)^2}{N' - 1} \tag{5.4}$$

and the pixel error,

$$\sigma_p = \sqrt{\frac{v_p}{N'}} \tag{5.5}$$

Here, $i' \subset i$. The addresses associated with a particular pixel (i') are ascertained using the telescope pointing data, $\vec{\theta}(r_i, \delta_i)$.

$$i' = \{i : r_p^{min} \leq r_i < r_p^{max}\} \cap \{i : \delta_p^{min} \leq \delta_i < \delta_p^{max}\} \tag{5.6}$$

This method does not account for noise correlations in the time domain or the pixel domain. One way to account for these effects is to calculate the maximum likelihood map.

$$m_p = \left(\mathcal{A}^T \mathcal{N}_t^{-1} \mathcal{A}\right)^{-1} \mathcal{A}^T \mathcal{N}_t^{-1} d_i \tag{5.7}$$

$$\mathcal{N}_p = \left(\mathcal{A}^T \mathcal{N}_t^{-1} \mathcal{A}\right)^{-1} \tag{5.8}$$

where $\mathcal{N}_p$ is the $N_p \times N_p$ pixel domain noise correlation matrix, $\mathcal{N}_t$ is the $N_t \times N_t$ time domain noise correlation matrix defined

$$\mathcal{N}_t \equiv \langle n_i n_i^T \rangle \tag{5.9}$$

and A is the $N_p \times N_t$ pointing matrix with pth column defined

$$\mathcal{A}_p = \begin{cases} 1 & \text{for} \quad i \cap i' \\ 0 & \text{for} \quad i \setminus i' \end{cases} \tag{5.10}$$

The matrix inversion and multiplication associated with the maximum likelihood map computation requires parallel processing and therefore represents a problem that lies beyond the scope of this thesis. The map computed using Equations 5.3 & 5.5 is the status quo circa July 2004. Subsequent more sophisticated MAXIPOL analyses will account for all relevant correlations. The reader should interpret all pixel domain results presented here as a rough first estimate.

5.2 Transient Removal

To remove the g_i term from Equation 5.1 we use the method schematically illustrated in Figure 5.1. The ultimate goal is to catalog the index values of sampled data containing signal from cosmic rays or other transient signals. The data elements cataloged are not used in the pixelized sky map.

The raw MAXIPOL data is nominally stored in binary data files with 9600 data frames per file and 192 16-bit data words per frame. Each frame has a unique frame number recorded as a 2 digit base

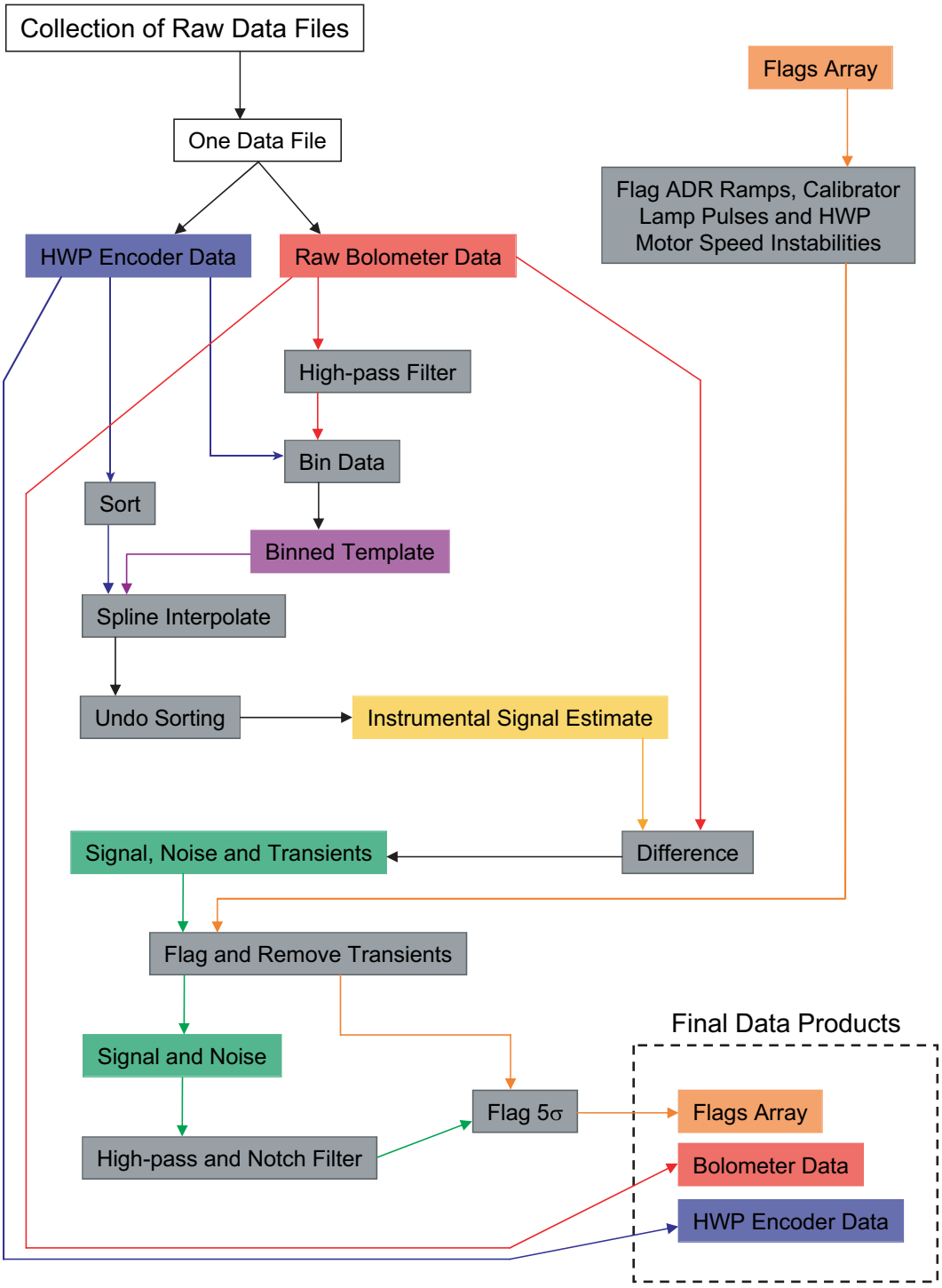

Figure 5.1: Schematic representation of the algorithm used to flag transient signals.

2^{16} number. The frame numbers of frames containing data corrupted by calibrator lamp pulses, ADR current ramps and HWP motor speed instabilities were cataloged; using this lookup table, the data rendered useless by the aforementioned phenomena are flagged as bad out of hand by this procedure.

Each bolometer is sampled four times per frame yielding 38,400 bolometer samples per file. In total, each bolometer was sampled 5,778,432 times during the primary CMB scan centered on Beta Ursae Minoris. Working with several arrays containing five million elements each is a cumbersome task because the transient signal removal software requires several transforms to the frequency domain. As a result, the decision was made when designing this algorithm to work with one file of data at a time.

Usually the magnitude of the transient signals we are searching for is smaller than the magnitude of the instrumental signal so it is necessary to remove the instrumental signal in order to simply locate the transients. To do this subtraction we use the following algorithm. First, the data is high-pass filtered in the frequency domain to remove any $1/f$ noise.

$$d_i^{\mathcal{F}} = \mathrm{Re}\left(\sum_{k=0}^{N-1} \widetilde{d}_k \, \mathcal{F}_k \, e^{i2\pi ki/N}\right) \tag{5.11}$$

where the $\sim$ indicates the discrete forward Fourier transform

$$\widetilde{d}_k = \frac{1}{N}\sum_{i=0}^{N-1} d_i \, e^{-i2\pi ki/N} \tag{5.12}$$

and $\mathcal{F}_k$ is a simple square high-pass filter defined as

$$\mathcal{F}_k = \begin{cases} 1 & \text{for} \quad \{k : |f_k| \geq 1\} \\ 0 & \text{for} \quad \{k : |f_k| < 1\} \end{cases} \tag{5.13}$$

The filter cutoff is designed to match the typical $1/f_{knee}$ of $\sim$0.5 Hz. Here we use the FFT storage scheme where the frequency associated with any FFT bin indexed by k is

$$f_k = \frac{k}{N\,\Delta t} \quad \text{for} \quad k = 0, 1, \cdots, \frac{N}{2} \tag{5.14}$$

$$f_{N-k} = \frac{-k}{N\,\Delta t} \quad \text{for} \quad k = 1, 2, \cdots, \frac{N}{2} - 1 \tag{5.15}$$

The filtered data is then binned in HWP angle where the samples in any bin superscripted by α are

$$b_j^{\alpha} = d_{i'}^{\mathcal{F}} \quad \text{where} \quad i' = \{i : \alpha \leq \rho_i < \alpha + 1\} \quad \text{and} \quad \alpha = 0, 1, \cdots, 359 \tag{5.16}$$

Clearly $b_j^{\alpha} \subset d_i^{\mathcal{F}}$. The quantity ρ_i is the HWP orientation measured by the optical encoder coupled to the HWP drivetrain. The bin size for this template is set to 1°. Given our 1.9 Hz HWP rotation

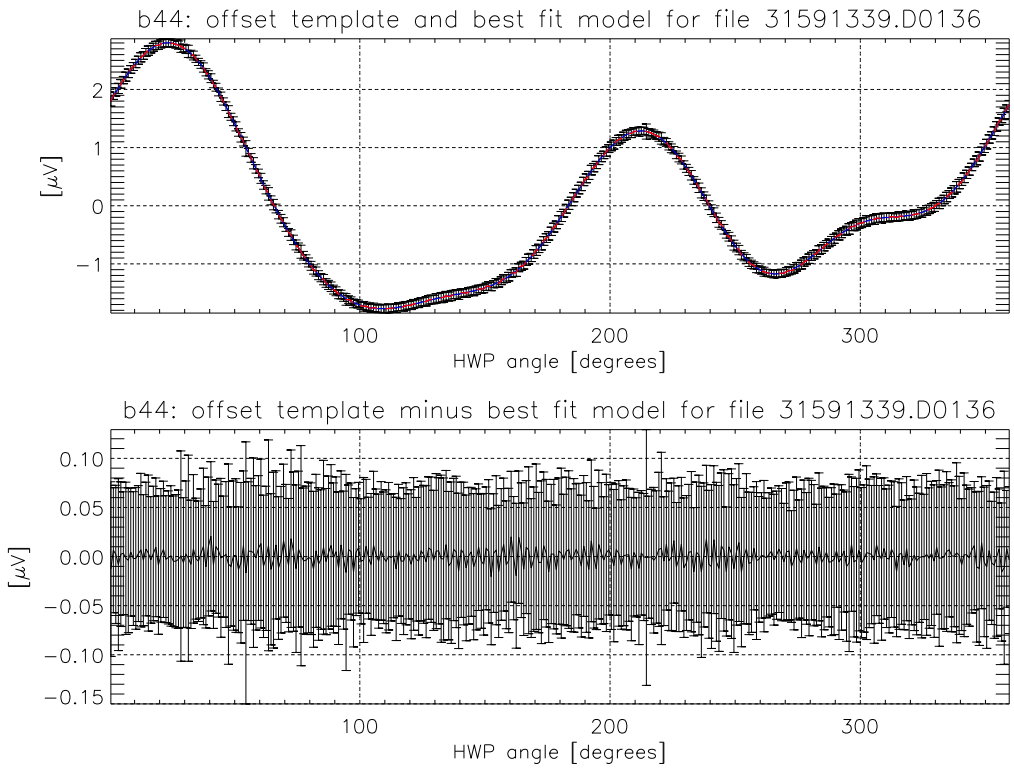

Figure 5.2: Binned HWP synchronous signal template. The binned data are plotted in the top panel and this template minus an eight sine wave model is plotted in the bottom panel to show the magnitude of the error per bin, which is equivalent to the noise *rms*.

frequency, the HWP moves 3.3° every 4.8 ms. Therefore if the bin size is set to a value $> 3.3°$, adjacent samples in the data set will have the same template value and the estimated instrumental signal will appear staircase instead of smooth and continuous. The 1° bin size will produce 107 samples per bin on average for a file with 38,400 total samples. If the the bin size is much less than 1° there may not be enough samples in the bin to meaningfully compute the bin average and standard deviation. The 1° bin size falls comfortably inside the window of viable bin sizes so we use it.

Next we create an average instrumental signal template for one HWP rotation, which will ultimately be subtracted from each HWP rotation in the data stream. Inside every bin, it is essential that all outliers be rejected so the average bin value is not erroneously biased. Any spurious signals injected into this template will be periodically added to the data stream thereby producing a systematic error. To reject the outliers, we histogram b_j^α. To maximize the usefulness of this histogram, we compute it iteratively increasing the bin size until the most populated bin has at least 20 samples in it. Since our noise is Gaussian, this histogram is typically Gaussian and outliers are defined as data

points in histogram bins that fall outside of this Gaussian envelope – specifically $\mu \pm 3\sigma$. In some bins however, the histogram is not Gaussian because the instrumental signal change across the bin is $\gg$ than the noise rms. To accommodate both scenarios, we compute the standard deviation about the *mode* rather than the mean. Here the *mode* is estimated from the the histogram as the bin value of the bin that has the most samples in it – the bin value of the bin with the most samples in it ($\pm$ the bin half width) is the most probable signal. The standard deviation about the *mode* statistic used to define the outlier cutoff criteria is computed using the histogram bin values, considering only bins that have at least one sample in them. The cutoff criteria was set to $mode \pm 1.5\,\sigma_{mode}$, which was empirically determined to be equivalent to be $\mu \pm 3\sigma$ in the pure Gaussian noise limit. Once the outliers are rejected, the bin average and standard deviation are computed.

$$\mu_\alpha = \frac{1}{N'} \sum_{j'=0}^{N'-1} b_{j'} \qquad \text{and} \qquad \sigma_\alpha = \sqrt{\sum_{j'=0}^{N'-1} \frac{(b_{j'} - \mu_\alpha)^2}{N' - 1}} \tag{5.17}$$

where $j' = \{j : mode - 1.5\,\sigma_{mode} \leq b_j^\alpha \leq mode + 1.5\,\sigma_{mode}\}$. The binned template is plotted in the top panel of Figure 5.2.

The entire HWP encoder data set, ρ_i, is then sorted so the measurements followed ascending order between 0 and 360 degrees. A template value is computed for each HWP orientation measurement using the binned template, μ_α, via spline interpolation. This interpolated HWP angle domain template is then unsorted thereby producing a time domain template data array that contains an estimate of the average instrumental signal at each bolometer sample. When this template stream is subtracted from the raw data, using the convention established in Equation 5.1, we are left with

$$d_i = s_i + n_i + g_i + h_i - \hat{h}_i \simeq s_i + n_i + g_i \tag{5.18}$$

Now the g_i signal is visible and can therefore be masked out.

The HWP synchronous instrumental signal subtraction is demonstrated in Figure 5.3. Three minutes of BUM scan data from one 140 GHz photometer is plotted versus HWP orientation angle in the upper left panel. For clarity, this patch of data contains no transients, so for this example

$$d_i = s_i + n_i + h_i \tag{5.19}$$

The power spectrum of this time ordered data is plotted in the upper right panel. The estimated template stream and its companion power spectrum are plotted in the middle left and right, respectively. The data minus the template stream and the power spectrum of the difference are plotted in the bottom two panels. Notice the instrumental signals (h_i) that produce the peaks in the upper right panel subtract out to at least the nominal white noise level of the photometer. Therefore,

$$d_i = s_i + n_i + h_i - \hat{h}_i \simeq s_i + n_i \tag{5.20}$$

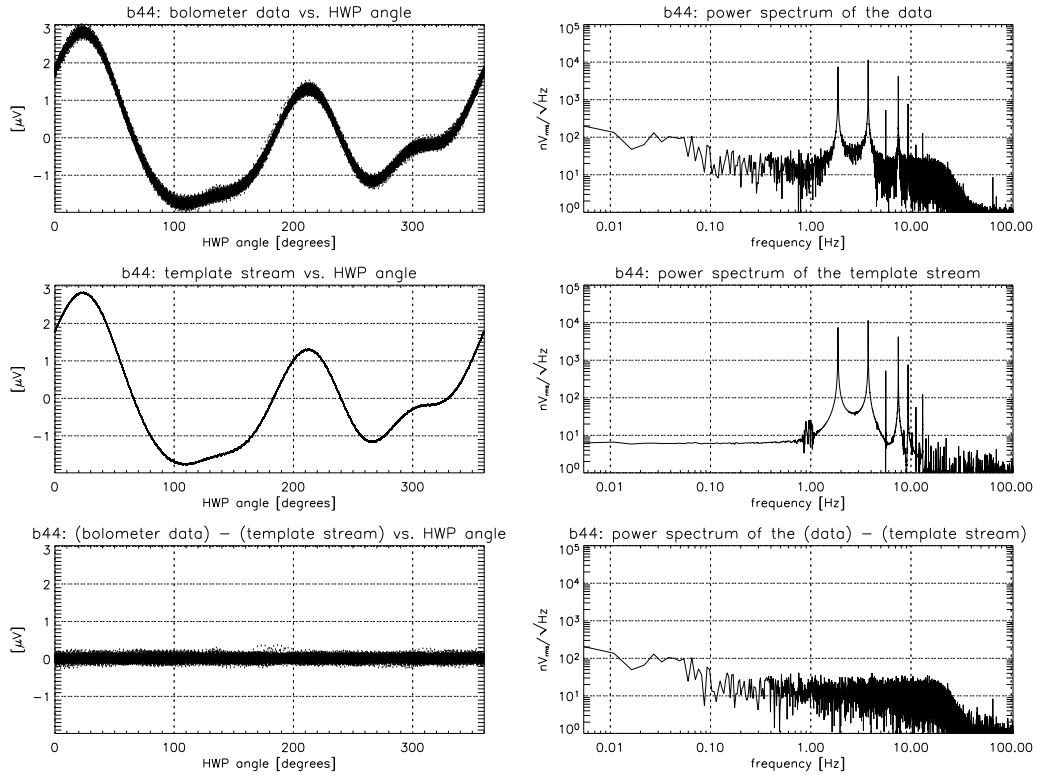

Figure 5.3: Demonstration of the HWP synchronous instrumental signal removal (see Section 5.2).

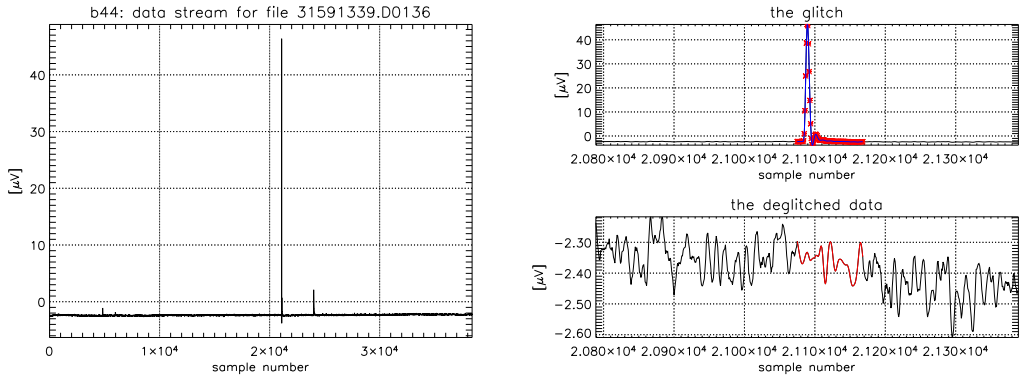

(*a*) (*b*)

Figure 5.4: Demonstration of transient removal and gap filling.

A set containing 5,778,432 Gaussian random variables should have only 3.3 samples outside the window $\mu \pm 5\,\sigma$. Since our noise is Gaussian, a naive approach for removing g_i from d_i leaving only n_i and s_i would be to reject all samples greater than 5-σ away from the mean[1]. In fact, there are two issues that complicate this operation. First, large transients erroneously bias the estimate of μ and σ. Second, a simple application of the 5-σ exclusion criteria assumes the data stream is noise dominated ($s_i \ll n_i$). If this assumption is wrong, this blind rejection would remove viable and interesting signal from the data stream. Our solution to the second problem also solves the first problem.

To eliminate the possibility of discarding viable sky signal, we filter the raw data minus the template stream in the frequency domain before applying the 5-σ rejection criteria. Here we use the transforms described in Equations 5.11 and 5.12, and a filter that removes all signals in the frequency bands where the sky signals may reside.

$$\mathcal{F}_k = \begin{cases} 1 & \text{for} \quad \{k : 2 < |f_k| < 6\} \cup \{k : |f_k| > 10\} \\ 0 & \text{for} \quad \{k : |f_k| \leq 2\} \cup \{k : 6 \leq |f_k| \leq 10\} \end{cases} \tag{5.21}$$

This filter is a square high-pass filter with a 2 Hz cutoff plus a square notch filter between 6 and 10 Hz. Data containing short timescale transients larger than $\sim$1 μV (typical noise $rms = 0.1$ μV) will produce pathological ringing in the filtered data. Therefore, before filtering we remove these large signals by hand and fill the generated gaps. An example of this operation is illustrated in Figure 5.4. The raw data minus the template stream is lotted in (*a*). A close-up of the largest

[1]Chauvenet's criteria states that it is reasonable to discard data if $N \times PTE < 0.5$. As mentioned above, 5,778,432 $\times$ $PTE_{5\sigma} = 3.3$, which means we slightly violate this rule. To faithfully follow Chauvenet's criteria we would need to use between 5.3 and 5.4-σ as a cutoff.

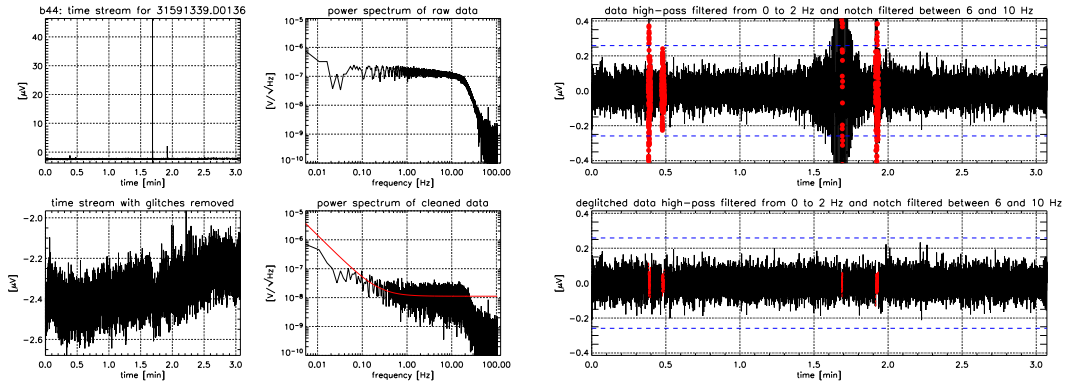

Figure 5.5: Demonstration of the need for transient removal before high-pass and notch filtering. The top row of plots shows the raw, uncleaned data, the power spectrum of this data stream and the data post filtering. The bottom row of plots shows the same sequence using the same data set but with the transients removed and the gaps filled.

transient in (a) is plotted in the top panel of (b). The blue curve marks the region where the data is flagged as bad. The bottom panel of (b) shows the same data minus the transient; in its place, a straight line whose endpoints match the gap endpoints plus a simulated noise realization. This gap filler is colored red. The noise realization is generated in the frequency domain according to the prescription outlined in Appendix B so the power spectrum of the gap filler closely matches the power spectrum of the actual data.

To elucidate the need for transient removal before filtering, we show in Figure 5.5 (a), the time stream and power spectrum of the uncleaned (top left and right, respectively) and cleaned (bottom left and right, respectively) data. By looking at the power spectrum one can see which power $\mathcal{F}_k$ removes and which power it does not remove. The top panel of portion (b) of the same figure clearly shows the ringing caused by filtering the uncleaned data, and how cleaning before filtering eliminates this pathology, in the bottom panel. The horizontal blue-dash demarcations in both panels illustrate the 5-σ cutoff limit. The large red dots in the top panel are plotted over points flagged as bad by the clean-then-filter method. Clearly, not removing the transients before filtering causes excessive and erroneous data flagging.

5.3 Demodulation

The data stream produced by an ideal HWP and wire-grid polarizer polarimeter observing a stationary sky can be modeled

$$s_i = \frac{1}{2}\left[I_{sky}(\vec{\theta_i}) + Q_{sky}(\vec{\theta_i})\cos(4\rho_i) + U_{sky}(\vec{\theta_i})\sin(4\rho_i) \right] \tag{5.22}$$

where I_{sky}, Q_{sky} and U_{sky} are the Stokes parameters of the sky, ρ is the HWP orientation angle and $\vec{\theta}$ is the telescope pointing. The HWP orientation and the telescope pointing are time varying quantities that are discretely sampled and indexed by i. Ultimately, we would like to make separate maps of I_{sky}, Q_{sky} and U_{sky}. To untangle these quantities, we use a method inspired by the lock-in amplifier. Multiplying the data by a reference created from the HWP optical encoder data stream

$$\begin{aligned} r_i^Q &= \cos(4\rho_i) \\ r_i^U &= \sin(4\rho_i) \end{aligned} \tag{5.23}$$

the time stream becomes

$$\begin{aligned} s_i r_i^Q &= \frac{1}{4}\left[Q_{sky}(\vec{\theta_i}) + Q_{sky}(\vec{\theta_i})\cos(8\rho_i) + U_{sky}(\vec{\theta_i})\sin(8\rho_i) + 2I_{sky}(\vec{\theta_i})\cos(4\rho_i) \right] \\ s_i r_i^U &= \frac{1}{4}\left[U_{sky}(\vec{\theta_i}) - U_{sky}(\vec{\theta_i})\cos(8\rho_i) + Q_{sky}(\vec{\theta_i})\sin(8\rho_i) + 2I_{sky}(\vec{\theta_i})\sin(4\rho_i) \right] \end{aligned} \tag{5.24}$$

The trigonometric terms in Equations 5.22 & 5.24 can be filtered away in the frequency domain.

$$\begin{aligned} s_i^T &= 2\,\mathrm{Re}\left(\sum_{k=0}^{N-1} \widetilde{(s_i)}_k\, \mathcal{F}_k\, e^{i2\pi ki/N} \right) \\ s_i^Q &= 2\,\mathrm{Re}\left(\sum_{k=0}^{N-1} \widetilde{(s_i r_i^Q)}_k\, \mathcal{F}_k\, e^{i2\pi ki/N} \right) \\ s_i^U &= 2\,\mathrm{Re}\left(\sum_{k=0}^{N-1} \widetilde{(s_i r_i^U)}_k\, \mathcal{F}_k\, e^{i2\pi ki/N} \right) \end{aligned} \tag{5.25}$$

The $\sim$ indicates forward transform

$$\widetilde{s}_k = \frac{1}{N}\sum_{i=0}^{N-1} s_i\, e^{-i2\pi ki/N} \tag{5.26}$$

and the reverse transform is written explicitly. If the filter, $\mathcal{F}_k$, is ideally then

$$s_i^T = \frac{I_{sky}(\vec{\theta_i})}{2}, \qquad s_i^Q = \frac{Q_{sky}(\vec{\theta_i})}{2} \qquad \text{and} \qquad s_i^U = \frac{U_{sky}(\vec{\theta_i})}{2}. \tag{5.27}$$

I_{sky}, Q_{sky} and U_{sky} are in fact time varying quantities because the telescope is scanning and the sky signals are spatially anisotropic. As a result, the sky measurements in the frequency domain have bandwidth, so the filter used in Equation 5.25 needs to be carefully designed to minimally alter the recorded Stokes parameters and maximally remove the trigonometric terms in Equations 5.22 & 5.24. To design the appropriate filter, we simulated a MAXIPOL-like experiment by raster scanning pixelized T, Q and U map realizations [37] and then studied the resulting signal-only data streams in the frequency domain. The maps we used are illustrated in Figure 5.6. The raw simulations contain structure smaller than $10'$ so as a first step we convolved the maps with a $10'$ FWHM Gaussian beam in k-space using two dimensional FFTs. Without this convolution, our result is misleading because fine structure increases the bandwidth of I_{sky}, Q_{sky} and U_{sky} in the frequency domain. Stated differently, there is a direct relationship between the beam size and the cutoff frequency of the low-pass filter we are designing.

To generate the data stream, we first created the telescope pointing data, $\vec{\theta}_i^{sim}$, and the HWP orientation data, ρ_i^{sim}. Here we used a 0.1 Hz telescope scan frequency, a 2° peak-to-peak scan amplitude, a 1.9 Hz HWP rotation frequency and a 4.8 ms sample period, which were the values realized during the MAXIPOL-1 BUM scan. Since the scan throw is 2° and the map is 6.4° wide, we rastered only the leftmost 2° of the simulation. For every $\vec{\theta}_i^{sim}$ we created a Stokes vector using the T, Q and U maps and spline interpolation.

$$\vec{S}_{in}^{sim} = \left[\ T(\vec{\theta}_i^{sim}),\, Q(\vec{\theta}_i^{sim}),\, U(\vec{\theta}_i^{sim}),\, 0\ \right] \tag{5.28}$$

This vector was then operated on by the HWP and polarizer Mueller matrices given in Equations 3.6 and 3.35, respectively. Here $\delta = \pi$, $p_x = 1$ and $p_y = 0$. The simulated signal-only data stream, s_i^{sim}, is the Ith element of $\vec{S}_{out}^{sim} = \mathcal{M}_p\ \mathcal{M}_h\ \vec{S}_{in}^{sim}$.

The power spectrum of s_i^{sim}, $s_i^{sim} r_i^Q$ and $s_i^{sim} r_i^U$ are plotted in Figure 5.7 (a). Notice the plot is log-log. The evident peak structure arises from the fact that the structure on the sky is constructed of discrete modes; in the frequency domain these modes appear at the harmonics of the telescope scan frequency. Again, the filter we are designing needs to capture the information at low frequencies and reject the large features at 4×1.9 Hz in all panels and 8×1.9 Hz in the middle and bottom panels. The signal roll-off from the $10'$ FWHM Gaussian beam is evident between 1 and 2 Hz. Unfortunately there is no obvious cutoff frequency that will allow us perfectly harvest one signal and perfectly reject the other two.

To further elucidate the T, Q and U convolution, we performed the experiment three additional times using the following input stokes vectors.

$$\vec{S}_{in}^{sim} \quad = \quad \left[\ T(\vec{\theta}_i^{sim}),\, 0,\, 0,\, 0\ \right]$$

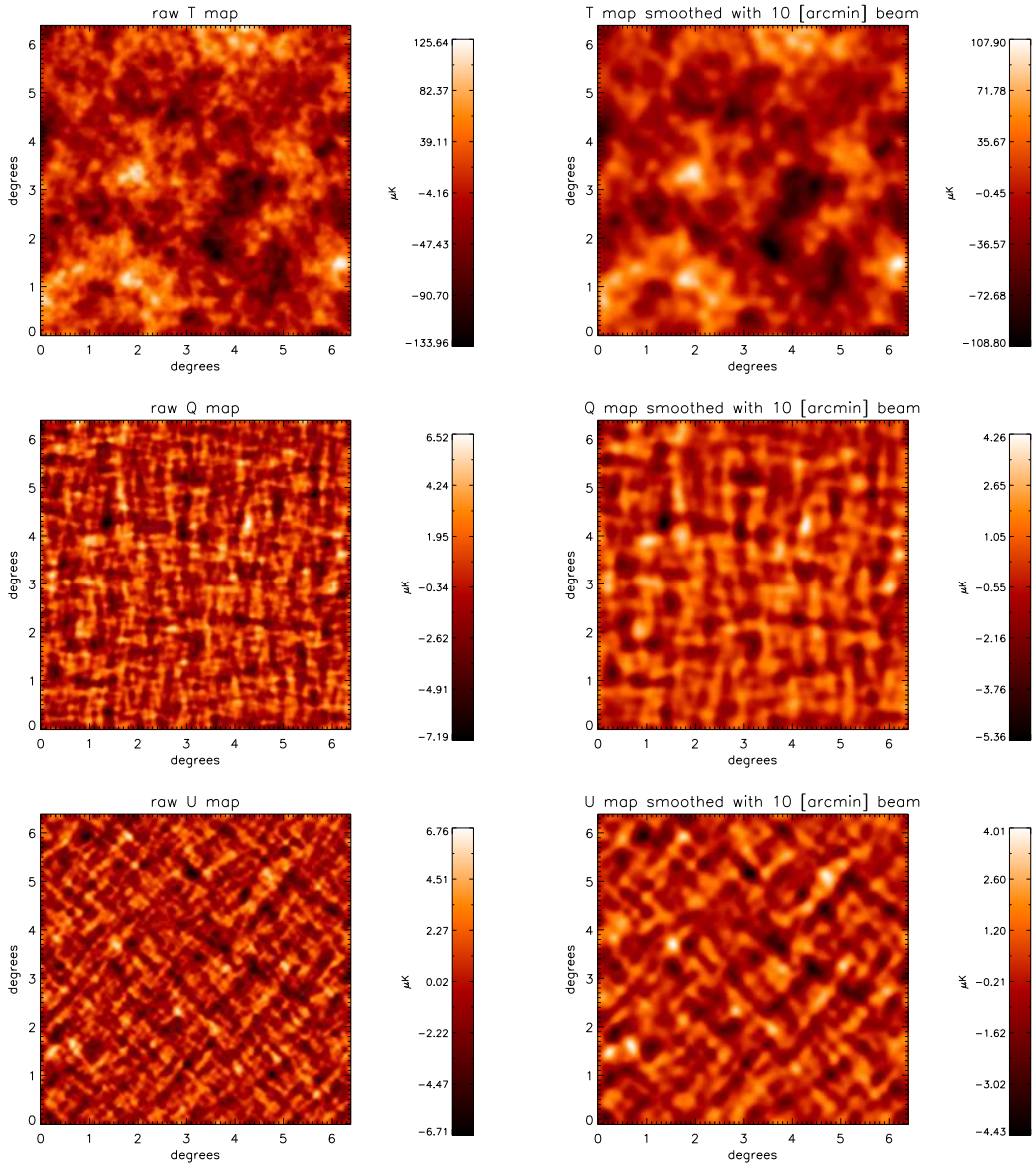

Figure 5.6: Sky realizations used to design the band-pass filter used in the signal demodulation software. The raw T, Q and U maps are displayed in the left column; these maps convolved with a $10'$ FWHM Gaussian beam are displayed in the right column.

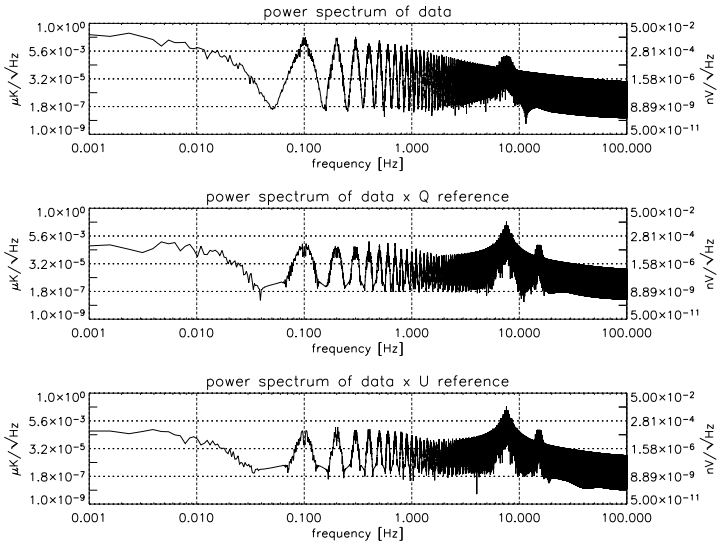

(*a*)

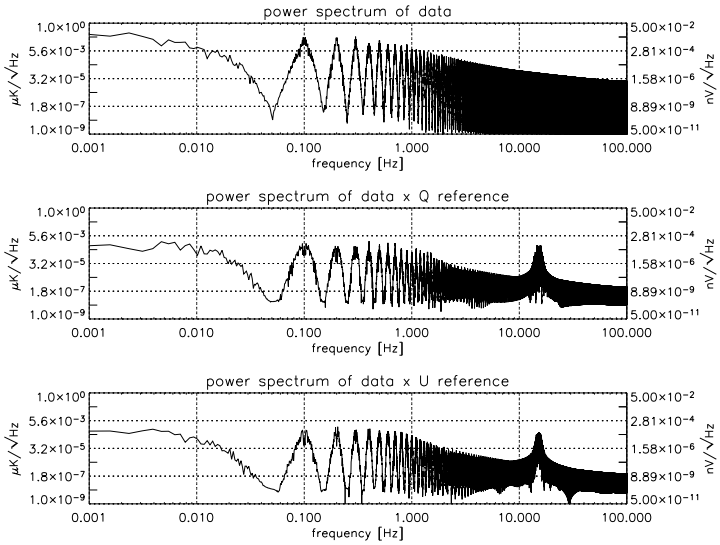

(*b*)

Figure 5.7: Power spectrum of signal-only time streams generated by scanning the sky realizations illustrated in Figure 5.6.

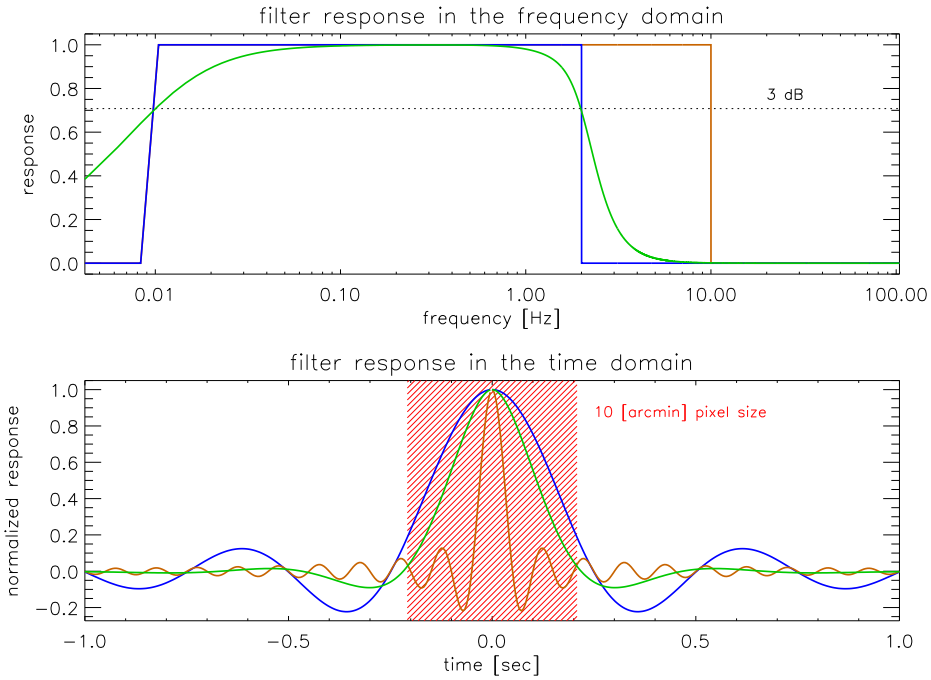

Figure 5.8: The band-pass filters considered for demodulation presented in the frequency and the time domain. The red, hashed region in the bottom panel represents the size of a $10'$ pixel given a scan speed of 0.4 deg/sec.

$$\begin{aligned} \vec{S}_{in}^{sim} &= \left[\, 0,\, Q(\vec{\theta}_i^{sim}),\, 0,\, 0 \,\right] \\ \vec{S}_{in}^{sim} &= \left[\, 0,\, 0,\, U(\vec{\theta}_i^{sim}),\, 0 \,\right] \end{aligned} \tag{5.29}$$

The power spectrum of s_i^{sim}, $s_i^{sim} r_i^Q$ and $s_i^{sim} r_i^U$ resulting from these new data streams are plotted in Figure 5.7 (b). Now it is more clear how the individual T, Q and U signals contribute to the power spectra though it is still not clear where we should set the filter cutoff frequency.

In fact, the optimal filter design is an ongoing topic of study. Two primary filters we are considering are illustrated as the blue and green curves in the top panel of Figure 5.8. Notice these filters are band-pass filters rather than simple low-pass filters. In the actual MAXIPOL-1 data, spurious signals contaminate the frequencies below ∼0.1 Hz. Specifically, at these low frequencies, the T measurements are mixed with detector $1/f$ noise and scan synchronous noise, while the Q and U measurements are mixed with instrumental polarization and other time stationary HWP synchronous signals. For T, Q and U, only map offsets and gradients exist below 0.1 Hz in the frequency domain anyway. Since MAXIPOL in an anisotropy experiment we have justification for filtering these sky signals out at this stage.

The blue curve is a square filter defined

$$\mathcal{F}_k = \begin{cases} 1 & \text{for} \quad \{k : |f_k| \geq 0.01\} \cap \{k : |f_k| \leq 2\} \\ 0 & \text{for} \quad \{k : |f_k| < 0.01\} \cup \{k : |f_k| > 2\} \end{cases} \tag{5.30}$$

while the green curve is a single pole high-pass filter and a four pole Butterworth low-pass filter defined

$$\begin{aligned} \mathcal{F}_{high} &= \frac{\frac{if_k}{f_{knee}^{high}}}{1 + \frac{if_k}{f_{knee}^{high}}} \\ \mathcal{F}_{low} &= \frac{1}{\left[1 + a_1 \left(\frac{if_k}{f_{knee}^{low}}\right) + b_1 \left(\frac{if_k}{f_{knee}^{low}}\right)^2\right] \left[1 + a_2 \left(\frac{if_k}{f_{knee}^{low}}\right) + b_2 \left(\frac{if_k}{f_{knee}^{low}}\right)^2\right]} \\ \mathcal{F}_k &= |\, \mathcal{F}_{low}\, \mathcal{F}_{high}\, | \end{aligned} \tag{5.31}$$

with $f_{knee}^{high} = 0.01$, $a_1 = 2.$, $a_2 = 0.7$, $b_1 = 1.35$, $b_2 = 0.9$ and $f_{knee}^{low} = 2$.

The time domain representation of these filters is plotted in the bottom panel of Figure 5.8. The red hashed region illustrates the size of a $10'$ sky pixel assuming a 4 deg/sec telescope scan speed. Clearly the square filter removes the unwanted signals at high frequencies completely, but causes complicated pixel-pixel noise and signal correlation. The Butterworth filter produces less correlation but allows more T signal to leak into the Q and U maps. A program to optimally solve this problem is underway.

For this discussion we choose to demonstrate the viability of the square filter using our simulation pipeline. Using Equation 5.30 and Equation 5.25 we computed s_i^T, s_i^Q and s_i^U. Using θ_i^{sim} we binned these data and formed pixelized maps with $5'$ pixels. The results are plotted in Figure 5.9. The raw T, Q and U data are plotted in the left column, maps produced from time streams generated by the demodulation pipeline are plotted in the middle column and their difference is plotted in the right column. The square filter preserves structure well but not perfectly in all maps. Clearly T loses power at the largest angular scales. The horizontal bands in the difference maps illustrate the correlation effect. The conclusion is the method is viable but needs to be optimized.

5.4 Instrumental Signal Estimator

The orange curves in the top and bottom panels of Figure 5.8 show the filter response of a square band-pass filter in the frequency and time domains, respectively; this filter has a 0.01 Hz high-pass

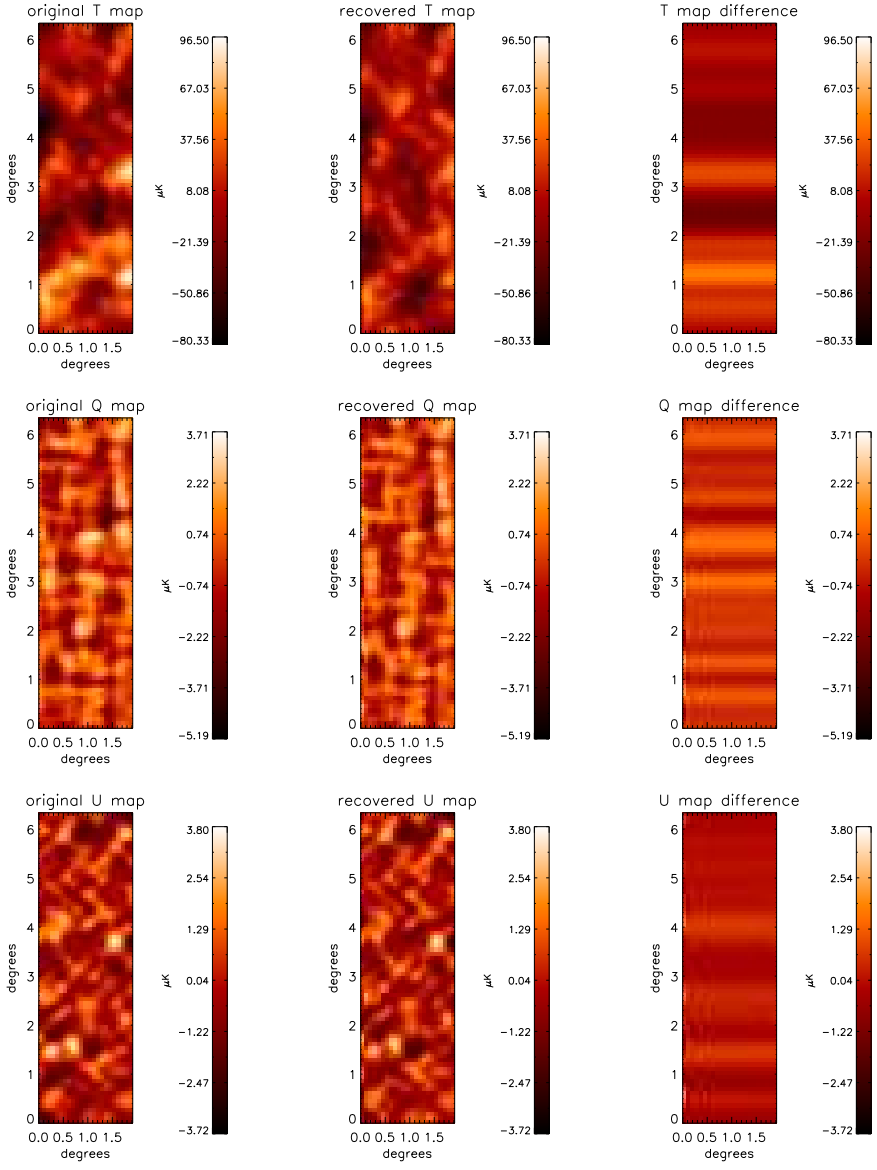

Figure 5.9: Demonstration of the demodulation software.

cutoff and a 10 Hz low-pass cutoff. Comparing the orange curve to the blue curve, it is apparent that by extending the low-pass filter cutoff to higher frequencies, the time-time and therefore the pixel-pixel correlations are reduced, which is favorable. We can use Equation 5.25 on

$$d_i = s_i + n_i + h_i \tag{5.32}$$

to ascertain s_i^T, s_i^Q and s_i^U but the h_i term prevents us from setting the low-pass cutoff much higher than ∼1.5 Hz. In order to extend the low-pass cutoff to 2 Hz or beyond to decrease correlations it is necessary to first subtract h_i from d_i before multiplying d_i by the Q or U reference signal. Without this subtraction, h_i will leak into the T, Q and U maps and produce systematic error. An algorithm for estimating h_i given 3.1 min of time ordered data was presented in Section 5.2. This procedure assumes the amplitude of each Fourier component in h_i is constant in time. In fact, the amplitudes of the Fourier components change on timescales much greater than 3.1 min. Ultimately an h_i estimator will be integrated into the map making pipeline that will be discussed in Section 5.5 so it is necessary to extend the usefulness of the existing algorithm so that it can be used to remove time varying signals as well. In the map making pipeline, data chunks are typically 20 min long with endpoints defined by the calibrator lamp pulses that occurred every ∼20 min during the MAXIPOL-1 flight. On these time scales, we have empirically determined that the model

$$\hat{h}_i = \xi + \sum_{x=1}^{8} (\beta_x t_i + \beta_x^o) \cos(x\,\rho_i + \phi_x) \tag{5.33}$$

accurately describes the time varying instrumental signals. Notice the amplitude of each Fourier component varies linearly with time. In sum the model has 25 free parameters that must be estimated.

As a first step toward estimating $\hat{h}_i$, the binned template is created according to

$$\mu_\alpha = \frac{1}{N'} \sum_{j'=0}^{N'-1} b_{j'} \qquad \text{and} \qquad \sigma_\alpha = \sqrt{\sum_{j'=0}^{N'-1} \frac{(b_{j'} - \mu_\alpha)^2}{N'(N'-1)}} \tag{5.34}$$

where $j' = \{j : mode - 1.5\,\sigma_{mode} \leq b_j^\alpha \leq mode + 1.5\,\sigma_{mode}\}$ and the time stationary model

$$\hat{h}_\alpha^o = \xi + \sum_{x=1}^{8} \beta_x^o \cos(x\,\rho_\alpha + \phi_x) \tag{5.35}$$

is fit to this template bins using a non-linear least squares gradient expansion algorithm with convergence criteria set to $\Delta\chi^2 = 10^{-6}$. The best fit model is plotted in blue over the binned template in the top panel of Figure 5.2 and the binned template minus the best fit model is plotted in the bottom panel. Using ϕ_x estimated by this fit, we construct a phase-locked sine wave reference for each Fourier component using the HWP encoder data.

$$r_i^x = cos(x\rho_i + \phi_x) \tag{5.36}$$

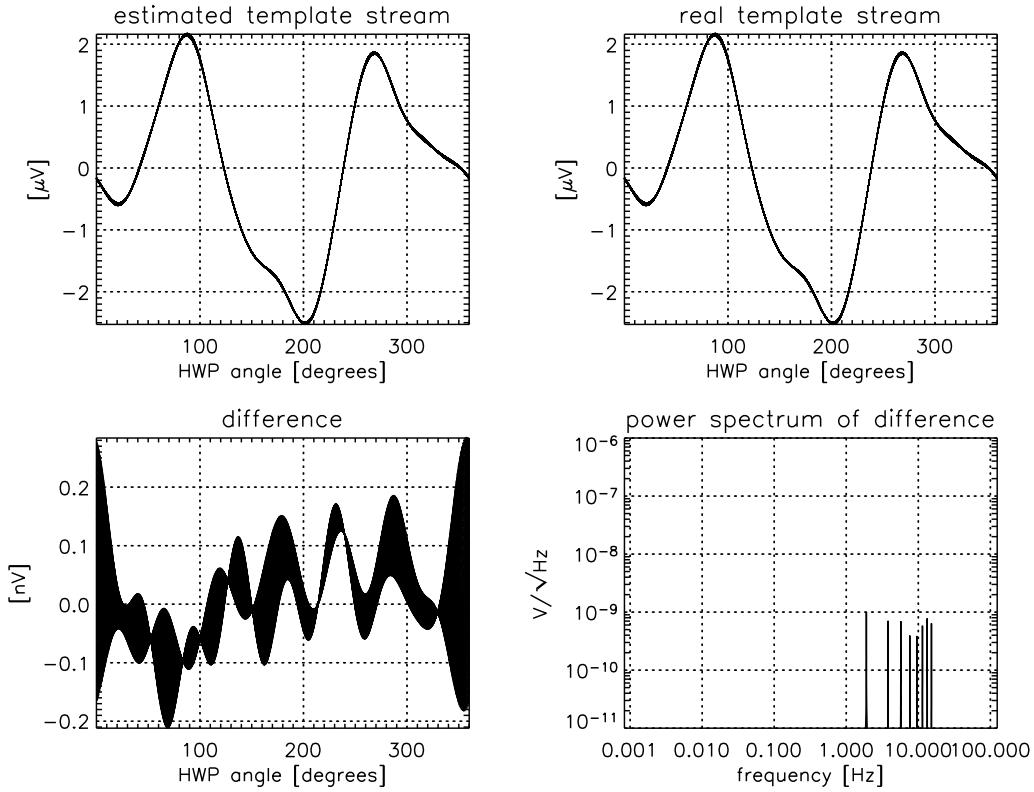

Figure 5.10: Demonstration of the time varying instrumental signal estimator. The estimate of the simulated instrumental signal is plotted in the upper left, while the simulation is plotted in the upper right. Their difference and the power spectrum of their difference are plotted in the lower panels (see Section 5.4).

Now we software lock-in on each Fourier component individually using r_i^x and this square low-pass filter

$$\mathcal{F}_k = \begin{cases} 1 & \text{for} \quad \{k : |f_k| > 1.5\} \\ 0 & \text{for} \quad \{k : |f_k| \leq 1.5\} \end{cases} \tag{5.37}$$

Post lock-in we fit a line to the data to ascertain β_x and β_x^o and then construct $\hat{h}_i$.

This operation is conducted in the presence of detector noise so $\hat{h}_i$ truly is an estimate.

$$d_i = s_i + n_i + h_i - \hat{h}_i \neq s_i + n_i \tag{5.38}$$

The h_i - $\hat{h}_i$ residual must be $\ll s_i^T$, s_i^Q and s_i^U in order to make a detection. To test the viability of the algorithm and to determine the magnitude of the residual, we simulated a MAXIPOL-like experiment with s_i equal to the Ith element of $\vec{S}_{out}^{sim} = \mathcal{M}_p \mathcal{M}_h \vec{S}_{in}^{sim}$ (see Section 5.3), h_i equal to Equation 5.33 employing realistic parameter values and n_i generated in the frequency domain according to the prescription outlined in Appendix B. Here the white noise level is 1 nV/$\sqrt{\text{Hz}}$ and the calibration is 2×10^4 K/V. The raw T, Q and U sky simulations are plotted in the left

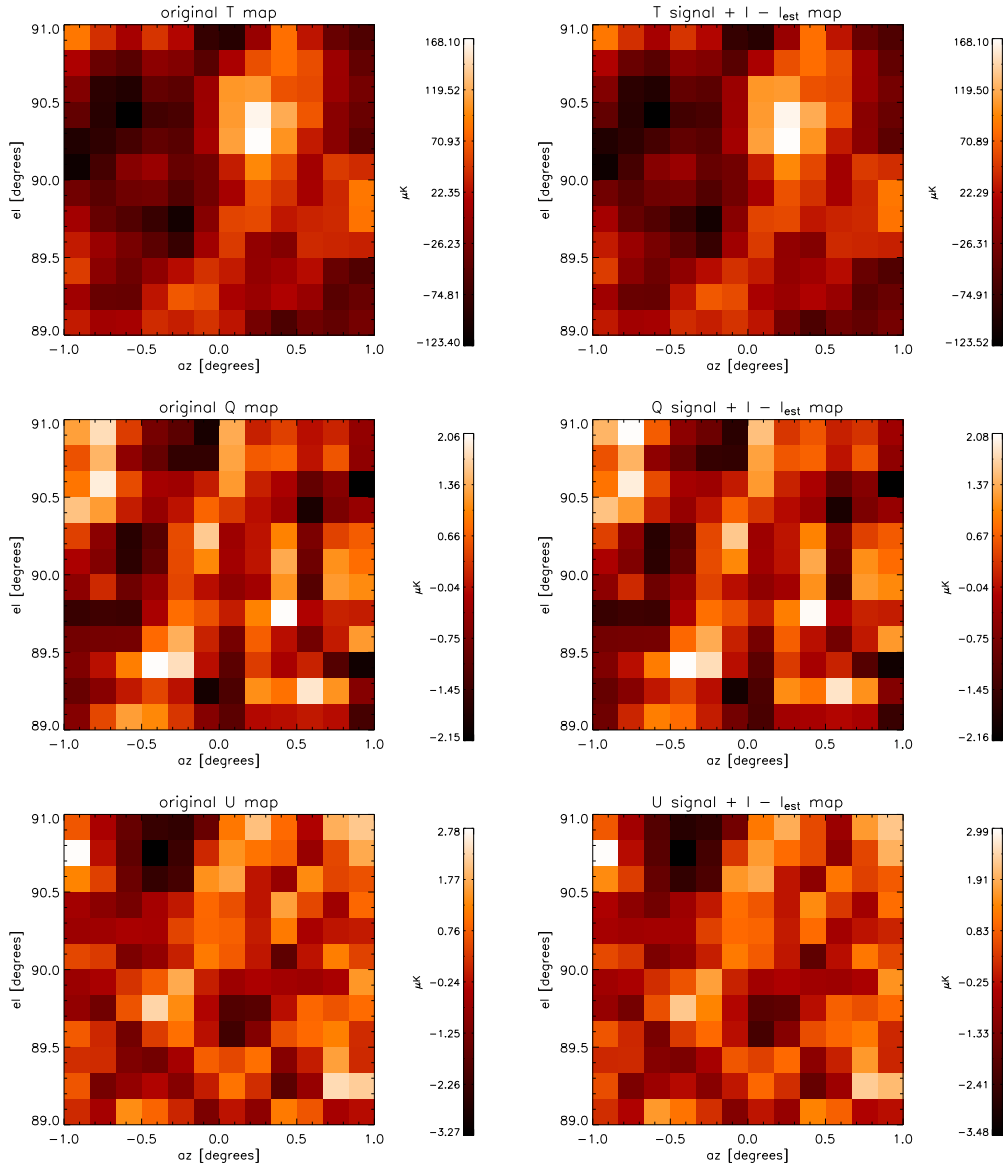

Figure 5.11: Demonstration of the viability of the time varying instrumental signal estimator. Simulated T, Q and U realizations are plotted in the left column. Maps of these signals output from the simulation pipeline are plotted in the right column. Using a white noise level of 1 nV/$\sqrt{\text{Hz}}$ and a responsivity of 2×10^4 K/V, the instrumental signal residual is smaller than the Q and U sky signals.

column of Figure 5.11 and the recovered signals plotted in the right column. Clearly the spatial structure is recovered nicely. In Figure 5.10, $\hat{h}_i$ and h_i are plotted in the upper left and upper right, respectively, while their difference is plotted in the lower left.

This test suggests the algorithm is viable. However, the noise level used in the simulation is lower than the nominal MAXIPOL noise level by a factor of 10. If the noise is increased to realistic levels, the h_i - $\hat{h}_i$ residual becomes the dominant signal in the recovered Q and U maps. Developing methods for more accurately estimating h_i is an ongoing area of research.

5.5 T, Q and U Maps

A schematic representation of the pipeline used to compute the T, Q and U maps presented in Figure 5.14 is illustrated in Figure 5.12. All of the tools discussed in this chapter contribute to this algorithm. Starting with the raw data from one photometer

$$d_i = s_i + n_i + h_i + g_i \tag{5.39}$$

the transient signals, g_i, are flagged using the procedure discussed in Section 5.2 and illustrated in Figure 5.1 on a file-by-file basis. Here the flag array is

$$f_i = \begin{cases} 1 & \text{for} \quad i \quad \text{with transients} \\ 0 & \text{for} \quad i \quad \text{without transients} \end{cases} \tag{5.40}$$

Post transient flagging the data arrays from all files are concatenated. These concatenated arrays are then broken into long data chunks with endpoints defined by calibrator lamp pulses, ADR current ramps or HWP motor speed instabilities; the typical chunk length is ∼20 min. For each chunk, a first estimate of h_i is subtracted from d_i

$$d_i = s_i + n_i + g_i + h_i - \hat{h}_i^1 \tag{5.41}$$

Using the flag array, g_i is removed from d_i and a straight line with endpoints matching the generated gap endpoints, plus a simulated noise realization is added. The $\hat{h}_i^1$ estimate is added back to the time stream to reproduce

$$d_i = s_i + n_i + h_i \qquad \text{for} \qquad \{\ i : f_i = 0\ \} \tag{5.42}$$

and create

$$d_i = s_i + n_i^{sim} + \hat{h}_i^1 \qquad \text{for} \qquad \{\ i : f_i = 1\ \} \tag{5.43}$$

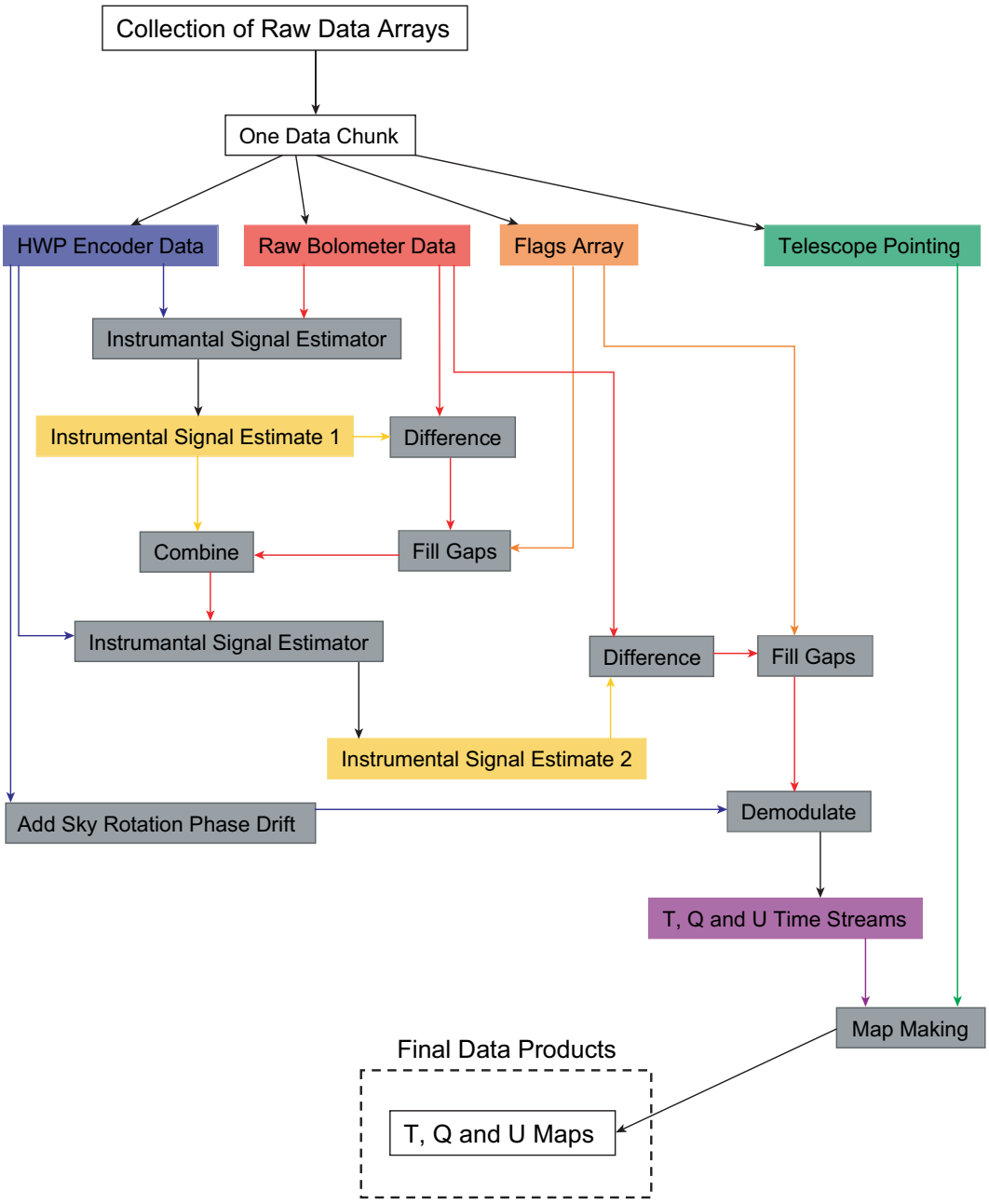

Figure 5.12: Schematic representation of the T, Q and U map making pipeline.

Now a more accurate h_i estimate is computed and then subtracted from this new clean d_i to produce

$$d_i = s_i + n_i + h_i - \hat{h}_i^2 \qquad \text{for} \qquad \{\ i : f_i = 0\ \} \tag{5.44}$$

$$d_i = s_i + n_i^{sim} + \hat{h}_i^1 - \hat{h}_i^2 \qquad \text{for} \qquad \{\ i : f_i = 1\ \} \tag{5.45}$$

The sky rotated significantly over the course of the MAXIPOL-1 BUM scan so we can not make the stationary sky assumption and model s_i as Equation 5.46 for this analysis. A more accurate model is the Ith element of $\vec{S}_{out} = \hat{\mathcal{M}}_p\ \hat{\mathcal{M}}_h\ \hat{\mathcal{M}}_r\ \vec{S}_{sky}$,

$$s_i = \frac{1}{2}\left[\, I_{sky}(\vec{\theta}_i) + Q_{sky}(\vec{\theta}_i)\cos(4\rho_i + 2\beta_i) + U_{sky}(\vec{\theta}_i)\sin(4\rho_i + 2\beta_i)\,\right] \tag{5.46}$$

where $\mathcal{M}_h$ and $\mathcal{M}_p$ are the Mueller matrices for the HWP (Equation 3.6) and focal plane polarizer (Equation 3.35), respectively, and $\mathcal{M}_r$ is the Mueller matrix for counter-clockwise rotation written

$$\hat{\mathcal{M}}_r = \begin{bmatrix} 1 & 0 & 0 & 0 \\ 0 & \cos(2\beta) & \sin(2\beta) & 0 \\ 0 & -\sin(2\beta) & \cos(2\beta) & 0 \\ 0 & 0 & 0 & 1 \end{bmatrix} \tag{5.47}$$

Here, $\delta = \pi$, $p_x = 1$, $p_y = 0$ and β is the rotation angle produced by the moving sky. β is referenced to a unit vector that points from a patch of sky in the observed region to the north celestial pole (NCP). This unit vector can be computed using the recorded telescope attitude.

$$\vec{n} = \vec{l} \times \frac{\vec{g} \times \vec{l}}{\sin(90 - \delta)} \qquad \vec{h} = \vec{l} \times \frac{\vec{z} \times \vec{l}}{\sin(90 - el)} \tag{5.48}$$

The unit vectors $\vec{l}$, $\vec{g}$ and $\vec{z}$ point from the telescope to the observation, NCP and zenith, respectively. The rotation angle of interest is subsequently computed $\beta = \cos^{-1}(\vec{n} \cdot \vec{h})$ [33, 34].

To produce s_i^T, s_i^Q and s_i^U we use Equation 5.25, the references

$$\begin{aligned} r_i^Q &= \cos(4\rho_i + 2\beta_i) \\ r_i^U &= \sin(4\rho_i + 2\beta_i) \end{aligned} \tag{5.49}$$

and the square band-pass filter

$$\mathcal{F}_k = \begin{cases} 1 & \text{for} \quad \{k : |f_k| \geq 0.01\} \cap \{k : |f_k| \leq 2\} \\ 0 & \text{for} \quad \{k : |f_k| < 0.01\} \cup \{k : |f_k| > 2\} \end{cases} \tag{5.50}$$

To eliminate the noise correlations this filter produces, we create frequency domain noise realizations, $\widetilde{n}_k^T$, $\widetilde{n}_k^Q$ and $\widetilde{n}_k^U$, according to Equations B.3 & B.4. The white noise level of these realizations,

σ, is matched to the white noise level of d_i. Now we transform d_i, $d_i r_i^Q$ and $d_i r_i^U$ to the frequency domain.

$$\begin{aligned} \widetilde{d}_k^T &= \frac{1}{N}\sum_{i=0}^{N-1} d_i\, e^{-i2\pi ki/N} \\ \widetilde{d}_k^Q &= \frac{1}{N}\sum_{i=0}^{N-1} d_i r_i^Q\, e^{-i2\pi ki/N} \\ \widetilde{d}_k^U &= \frac{1}{N}\sum_{i=0}^{N-1} d_i r_i^Q\, e^{-i2\pi ki/N} \end{aligned} \tag{5.51}$$

and then we redefine

$$\begin{aligned} \widetilde{n}_{k'}^T &= \widetilde{d}_{k'}^T \\ \widetilde{n}_{k'}^Q &= \widetilde{d}_{k'}^Q \\ \widetilde{n}_{k'}^U &= \widetilde{d}_{k'}^U \end{aligned} \tag{5.52}$$

$$k' = \{k : |f_k| \geq 0.01\} \cap \{k : |f_k| \leq 2\} \tag{5.53}$$

Now the T, Q and U time streams are computed by transforming the noise realizations doped with the actual sky signals back to the time domain.

$$\begin{aligned} d_i^T &= 2\,\mathrm{Re}\left(\sum_{k=0}^{N-1} \widetilde{n}_k^T\, \mathcal{F}_k\, e^{i2\pi ki/N}\right) \\ d_i^Q &= 2\,\mathrm{Re}\left(\sum_{k=0}^{N-1} \widetilde{n}_k^Q\, \mathcal{F}_k\, e^{i2\pi ki/N}\right) \\ d_i^U &= 2\,\mathrm{Re}\left(\sum_{k=0}^{N-1} \widetilde{n}_k^U\, \mathcal{F}_k\, e^{i2\pi ki/N}\right) \end{aligned} \tag{5.54}$$

Once we have d_i^T, d_i^Q and d_i^U, we create a pixelized map

$$m_p^T = \frac{1}{N'}\sum_{i'=0}^{N'-1} d_{i'}^T \qquad m_p^Q = \frac{1}{N'}\sum_{i'=0}^{N'-1} d_{i'}^Q \qquad m_p^U = \frac{1}{N'}\sum_{i'=0}^{N'-1} d_{i'}^U \tag{5.55}$$

with pixel variance,

$$v_p^T = \sum_{i'=0}^{N'-1} \frac{(d_{i'}^T - m_p^T)^2}{N'-1} \qquad v_p^Q = \sum_{i'=0}^{N'-1} \frac{(d_{i'}^Q - m_p^Q)^2}{N'-1} \qquad v_p^U = \sum_{i'=0}^{N'-1} \frac{(d_{i'}^U - m_p^U)^2}{N'-1} \tag{5.56}$$

and the pixel error,

$$\sigma_p^T = \sqrt{\frac{v_p^T}{N'}} \qquad \sigma_p^Q = \sqrt{\frac{v_p^Q}{N'}} \qquad \sigma_p^U = \sqrt{\frac{v_p^U}{N'}} \tag{5.57}$$

using the telescope pointing data, $\vec{\theta}(r_i, \delta_i)$.

$$i' = \{i : r_p^{min} \leq r_i < r_p^{max}\} \cap \{i : \delta_p^{min} \leq \delta_i < \delta_p^{max}\} \tag{5.58}$$

5.6 Combining Maps from Different Photometers

When combining the maps, we weighted the contribution of every photometer by the number of samples it contributed to any given pixel. The combine map therefore is

$$M_p^T = \frac{\sum_{x=1}^{12} \left(m_p^T\right)^x N_p^x}{\sum_{x=1}^{12} N_p^x} \qquad M_p^Q = \frac{\sum_{x=1}^{12} \left(m_p^Q\right)^x N_p^x}{\sum_{x=1}^{12} N_p^x} \qquad M_p^U = \frac{\sum_{x=1}^{12} \left(m_p^U\right)^x N_p^x}{\sum_{x=1}^{12} N_p^x} \tag{5.59}$$

with the pixel error

$$\sigma_p^T = \frac{\sqrt{\frac{\sum_{x=1}^{12} \left(\sum_{i'=0}^{N'-1} \left(d_{i'}^T\right)^2\right)^x}{\sum_{x=1}^{12} N_p^x} - M_p^T}}{\sqrt{\sum_{x=1}^{12} N_p^x}}$$

$$\sigma_p^Q = \frac{\sqrt{\frac{\sum_{x=1}^{12} \left(\sum_{i'=0}^{N'-1} \left(d_{i'}^Q\right)^2\right)^x}{\sum_{x=1}^{12} N_p^x} - M_p^Q}}{\sqrt{\sum_{x=1}^{12} N_p^x}} \tag{5.60}$$

$$\sigma_p^U = \frac{\sqrt{\dfrac{\sum_{x=1}^{12}\left(\sum_{i'=0}^{N'-1}\left(d_{i'}^U\right)^2\right)^x}{\sum_{x=1}^{12} N_p^x} - M_p^U}}{\sqrt{\sum_{x=1}^{12} N_p^x}}$$

Here, x is a label that links data elements to the photometer that produced that data. The M_p^T, M_p^Q and M_p^U maps are plotted in the left column of Figure 5.14 while M_p^T/σ_p^T, M_p^Q/σ_p^Q and M_p^U/σ_p^U are plotted in the right column. The value of the null buster statistic

$$\chi^2 = \frac{M_p^2}{N\,\sigma_p^2} \tag{5.61}$$

is printed in the lower left corner of the maps in the left column. Histograms of these maps are plotted in Figure 5.13.

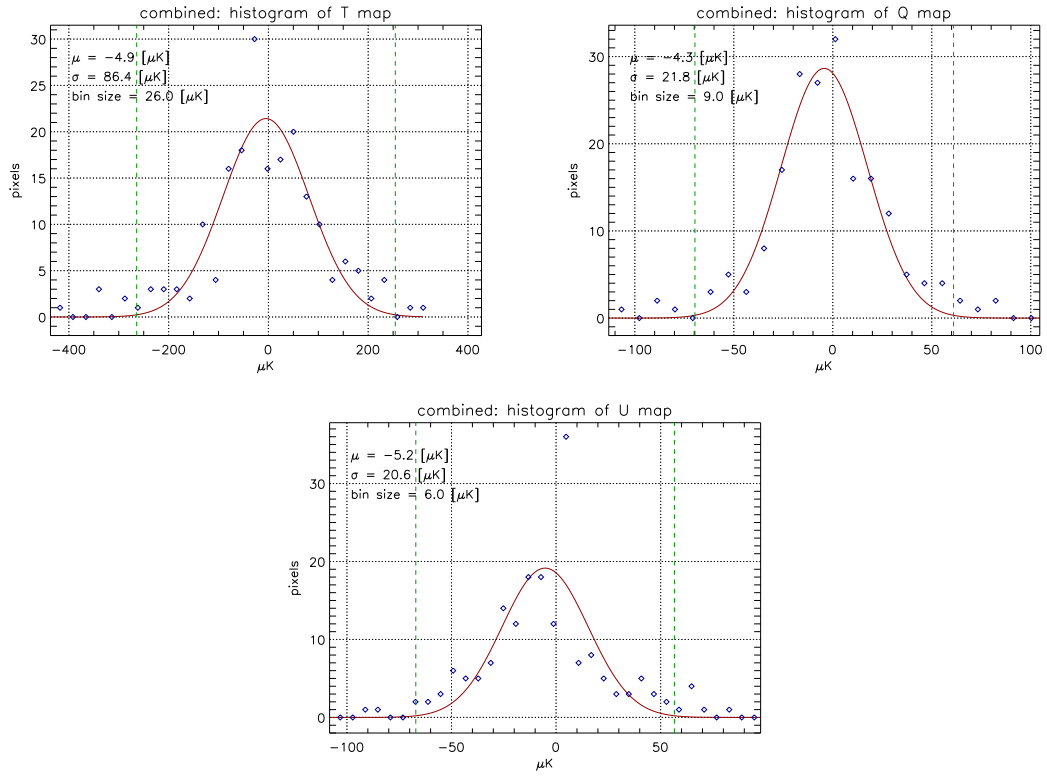

Figure 5.13: Histograms of the pixel values of the T, Q and U maps plotted in Figure 5.14.

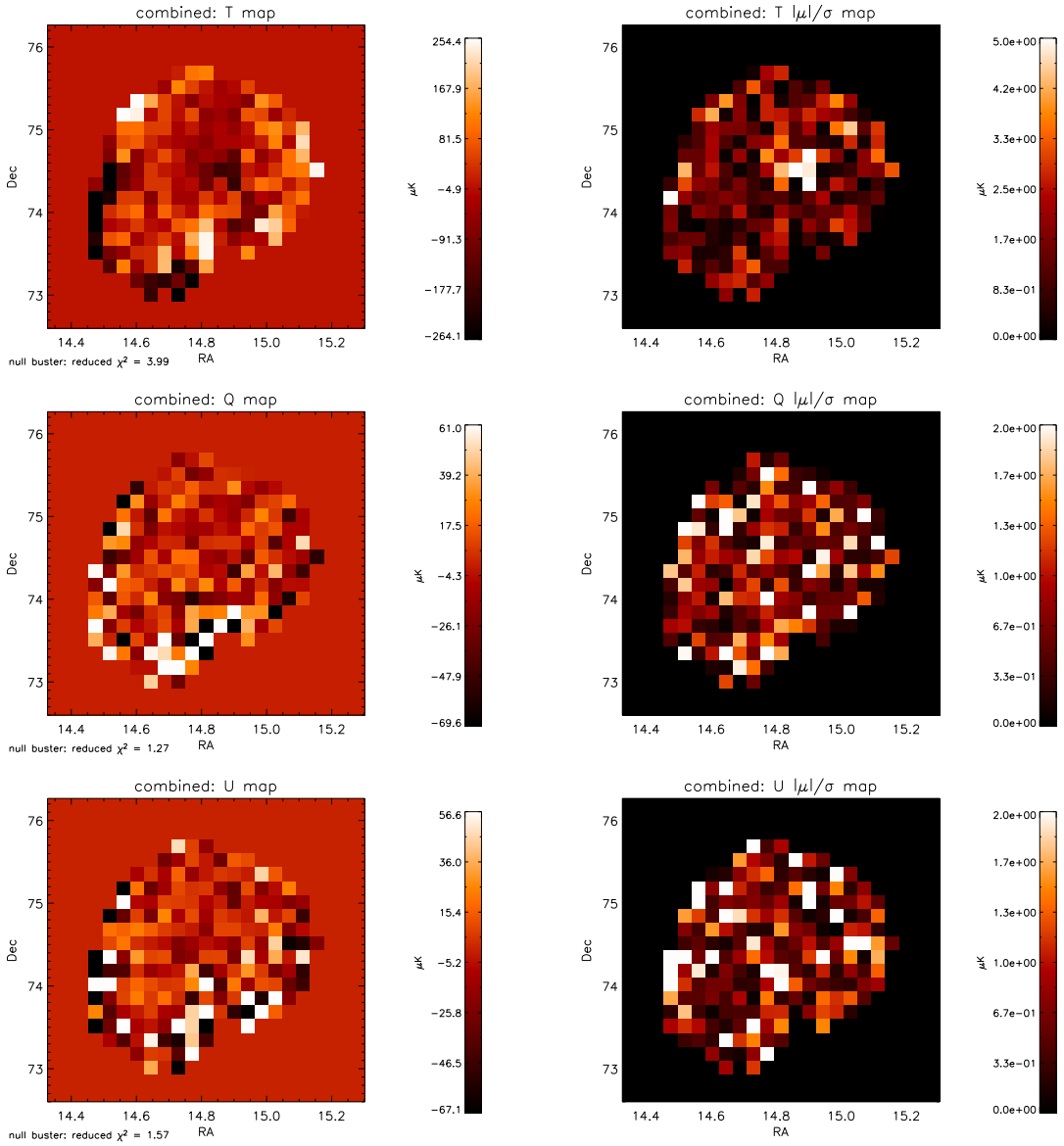

Figure 5.14: Preliminary maps from the MAXIPOL-1 observation near Beta Ursae Minoris. The T, Q and U maps are plotted in the left column while corresponding maps of the pixel mean divided by the pixel error are plotted in the right column (Section 5.6).

Chapter 6

The Future: B-Mode Characterization

6.1 Introduction

The recent detection of the E-mode and TE signals at the theoretically expected level justifies full characterization of the E-mode power spectrum and further exploration for the anticipated B-mode signals. This exploration calls for a new class of millimeter-wave polarimetric instrumentation to be developed with high receiver sensitivity and minimized, tractable systematic error. MAXIPOL has already made significant steps toward developing the necessary instrumentation by implementing polarimetry techniques that can be directly applied to a B-mode experiment.

6.2 B-mode Experiment Characteristics

At this stage B-mode instrument design is unconstrained; novel ideas aimed at increasing receiver sensitivity and reducing systematic error can and should be considered. However, for this discussion, I will assume the starting point pioneered by experiments like MAXIPOL and embraced by burgeoning experiments like QUaD and EBex: use of reflective telescope optics and a bolometric polarimeter employing a rotating half-wave plate and a fixed wire-grid polarizer. An instrument constructed following this prescription would be used to map the I, Q and U Stokes parameters of a two-dimensional patch of the sky by scanning the telescope appropriately in azimuth and elevation.

Clearly distinguishing primordial polarization from instrumental artifacts will require unprecedented control of systematic errors. Spurious instrumental signals will dominate the sky signals in

any B-mode experiment so all avoidable instrumental offsets should be preemptively identified and designed away, and all unavoidable instrumental offsets must be precisely known and designed to be tractable during data analysis. The principal issues associated with B-mode instrumentation are introduced and briefly described below. The following list outlines the topics that must be addressed during any instrument design process.

- **Increase Receiver Sensitivity**
  The noise equivalent power (NEP) of state-of-the-art millimeter-wave bolometers has reached a fundamental limit – the NEP is dominated by photon noise from the sky; therefore to achieve the necessary receiver sensitivity, we must extrapolate from the receiver status quo (MAXIPOL for example), increasing either the total number of detectors or the integration time per beam resolution element – or both. Future detector arrays will likely employ hundreds or even thousands of detector elements.

- **Minimize Systematic Errors from the Telescope Optics**
  Reflective telescope optics can create and/or modify partially polarized light through differential emission (create spurious Q and U signals), differential absorption (convert incoming T to Q or U) and cross-polarization (convert E to B). For typical systems, the emission and absorption effects produce signals that are roughly $\sim$1% polarized, which is large compared to the CMB signals. The telescope cross-polarization properties will need to be known to high accuracy to correctly measure the E- and B-mode power spectra. All of these effects can be minimized with careful optical design, such as use of an on-axis or Dragone system.

- **Monitor Foreground Signals**
  Beyond the gravitational lensing foreground mentioned in Chapter 1, atmospheric polarization [27] and polarized emission from galactic dust must also be carefully considered. Dust emission can be monitored with spectral discrimination while atmospheric signals may require implementation of polarimetric hardware tuned to the polarized 118 GHz oxygen lines. Circularly polarized atmospheric signals can be measured with a polarimeter utilizing a rotating quarter-wave plate, for instance.

- **Select Appropriate Beam Size and Symmetry**
  The beam size must be set to $\sim 5'$ to resolve the non-primordial B-mode signal at high ℓ; horns with symmetric beam patterns are essential as the mixture of sky rotation and asymmetric beams produces systematic error; and the horns must preserve the polarization properties of the sky signals precisely if polarization sensitive bolometers are to be used.

- **Reduce Systematic Errors from Polarimetry Hardware**
  The mechanism for rotating the 4 K HWP tends to induce spurious microphonic signals

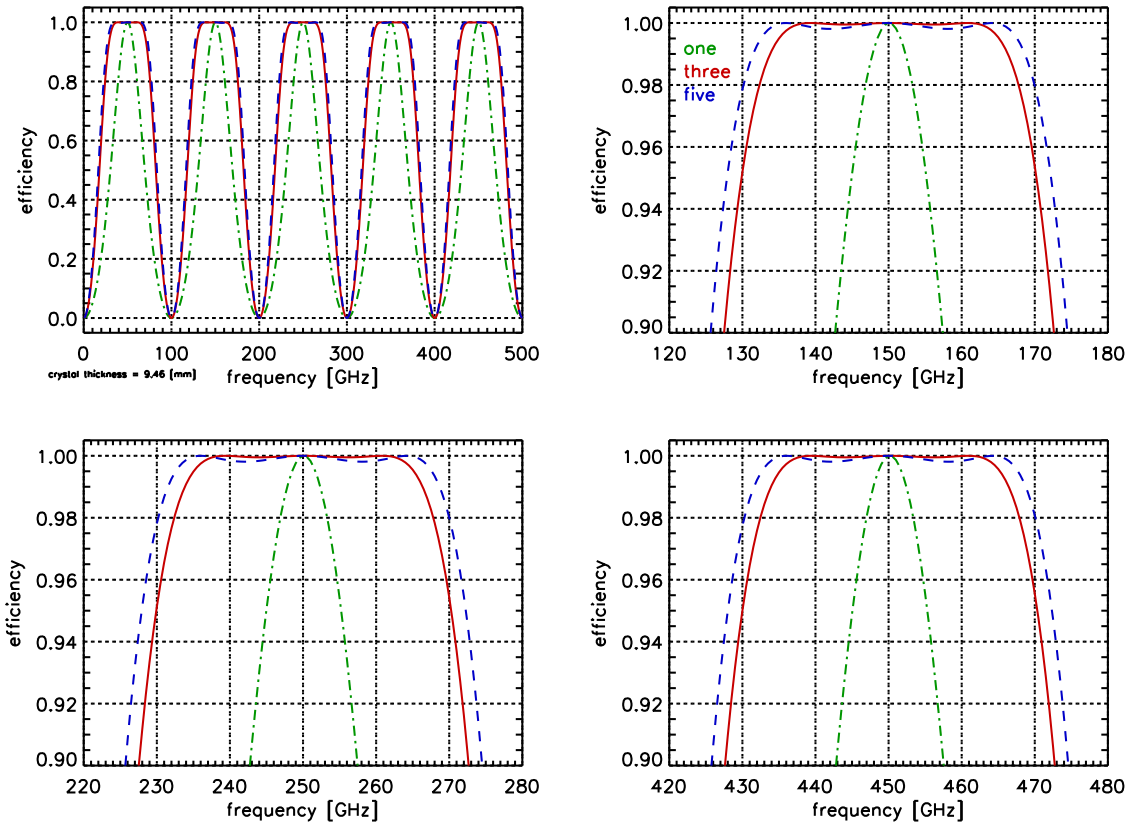

Figure 6.1: Expected polarimeter efficiency as a function of frequency for a HWP polarimeter and two AHWP polarimeters. The green, dash-dot curve illustrates the behavior of the HWP polarimeter, the red, solid curve the AHWP polarimeter employing three HWPs ($\delta_2 = 58^\circ$ and $\delta_3 = 0^\circ$) and the blue, dash curve an AHWP polarimeter employing five HWPs ($\delta_{2,4} = 70^\circ$ and $\delta_{3,5} = 0^\circ$).

through mechanical vibrations. The MAXIPOL example is one viable brute-force solution; another more elegant solution is a superconducting magnetic bearing, which promises fewer instrumental offsets and lower detector noise [28]. Optically, the overall polarimeter efficiency can be improved with the use of an achromatic HWP with achromatic anti-reflection coatings. Design and optimization of the achromatic HWP will be discussed in Section 6.3.

6.3 Achromatic Half-Wave Plate

In Chapter 3 we showed that the breadth of the spectra of the MAXIPOL 140 GHz photometers decreases the overall polarimeter efficiency to ∼90%. This inefficiency can be decreased by narrowing the band-pass filters. However, this action also decreases the number of photons reaching the detectors, which is unfavorable. A better solution is to keep the broad spectra and employ an achromatic HWP (AHWP).

The AHWP is made of a series of retarders, each tuned to be a HWP for the center frequency of the desired spectral band. The relative orientation of these crystals is appropriately set to one of many viable prescriptions. Specifically, we studied designs employing three and five HWPs and placed emphasis on optimizing the three HWP construction.

The Mueller matrix for a linear retarder as a function of orientation angle and frequency, $\hat{\mathcal{M}}_h(\rho,\nu)$, is given in Equation 3.6. In principal, the expected performance of the AHWP can be determined analytically by calculating the measured level polarization as a function of frequency

$$P_{out}(\nu) = \frac{\vec{S}_{out}^{I_{max}} - \vec{S}_{out}^{I_{min}}}{\vec{S}_{out}^{I_{max}} + \vec{S}_{out}^{I_{min}}} \tag{6.1}$$

by using the Ith term of the output Stokes vector

$$\hat{\mathcal{M}}_p \left[\hat{\mathcal{M}}_h(\rho+\delta_3,\nu)\ \hat{\mathcal{M}}_h(\rho+\delta_2,\nu)\ \hat{\mathcal{M}}_h(\rho,\nu) \right] \vec{S}_{in} = \vec{S}_{out} \tag{6.2}$$

Here, $\hat{\mathcal{M}}_p$ is the Mueller matrix for a polarizer given in Equation 3.35, S_{in} = [1,1,0,0] for all ν and $\delta_{2,3}$ are the orientation angles of the second and third HWPs in the stack with respect to the orientation of the first. $\vec{S}_{out}^{I_{max}}$ and $\vec{S}_{out}^{I_{min}}$ are determined with the derivative of $\vec{S}_{out}^{I}$

$$\frac{\partial \vec{S}_{out}^{I}(\rho,\nu)}{\partial \rho} = 0 \tag{6.3}$$

In practice, it is much easier to calculate $P_{out}(\nu)$ numerically. Figure 6.1 shows the result of a numerical calculation. For a given frequency, ν, ρ was stepped discretely between 0 and 180 degrees in 1 degree steps. $\vec{S}_{out}^{I_{max}}$ and $\vec{S}_{out}^{I_{min}}$ were determined by fitting the model

$$m = A\,\sin(4\rho+\phi) + B \tag{6.4}$$

to this data set. Here we used a gradient expansion algorithm to compute the non-linear least squares fit with no weighting – convergence criteria set to $\Delta\chi^2 = 1\times10^{-6}$. Now,

$$\vec{S}_{out}^{I_{max}} = B + A \quad \text{and} \quad \vec{S}_{out}^{I_{min}} = B - A \tag{6.5}$$

$P_{out}(\nu)$ is then calculated using Equation 6.1. Here the $\delta_2 = 58^\circ$ and $\delta_3 = 0^\circ$.

6.3.1 Optimize AHWP with Three Retarders

To explore how the performance of a polarimeter employing an AHWP comprised of three retarders depends on crystal orientation, we computed P_{out} vs. ν between 100 and 200 GHz for a grid of δ_2 and δ_3 angles. For this grid $0 \leq \delta_2 \leq 90$ and $0 \leq \delta_3 \leq 90$; step size was equal to 1°. At each grid point, the area under the P_{out} vs. ν curve was calculated numerically to quantitatively determine the breadth of the window, and the average deviation from $P_{out} = 1$ was determined in the band 150 ± 15 GHz. The results are plotted in Figure 6.2. Clearly there are many viable three-retarder AHWP prescriptions.

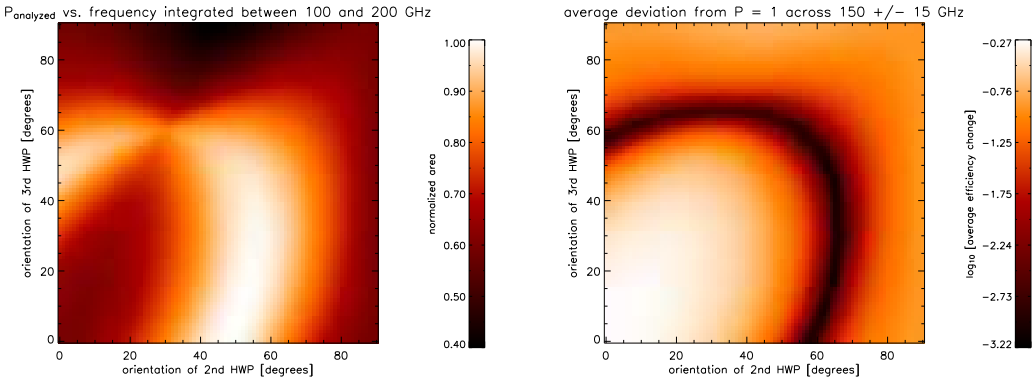

Figure 6.2: An optimization of an AHWP utilizing three retarders.

6.3.2 Optimize AHWP with Five Retarders

Optimizing a five retarder AHWP polarimeter in a similar way is more difficult because 65.6 million calculations are required rather than just the 8100 required for Figure 6.2. Applying the constraints $\delta_2 = \delta_4$ and $\delta_3 = \delta_5 = 0°$ simplifies the calculation considerably while still yielding useful results. $\delta_{2,4}$ was varied between 0 and 180° and the optimization statistics used as the figures of merit in Section 6.3.1 were computed. The results are plotted as the red curve in Figure 6.3. For comparison, the results from a three retarder analysis are also plotted as the blue curve. Here, δ_2 varies and δ_3 = 0°.

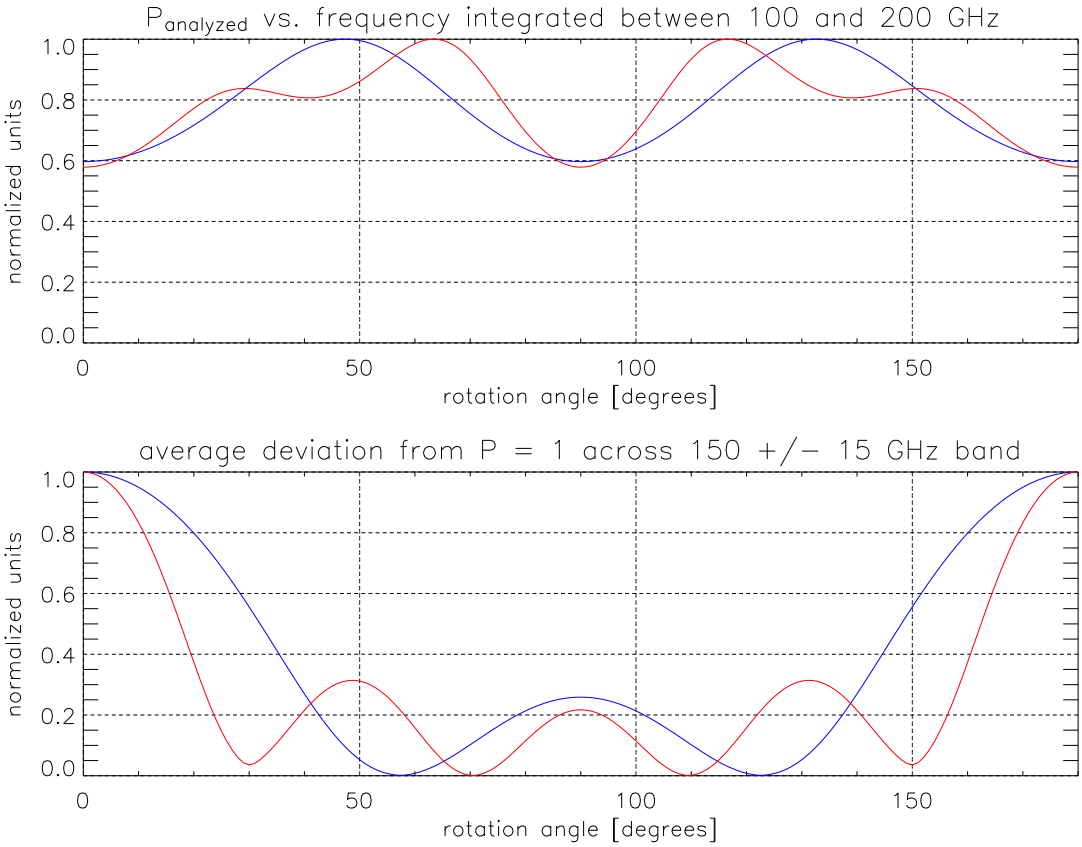

Figure 6.3: Optimization of a five retarder AHWP polarimeter (Section 6.3.2).

Appendix A

Computing the Power Spectrum of Time Ordered Data

A.1 Introduction

The power spectrum is a useful tool for analyzing time ordered data. Numerical methods for computing power spectra are covered extensively in the literature. However, distilling the relevant information from books like *Numerical Recipes in C* for MAXIPOL data analysis requires some effort. To date, there is no document publicly available within the MAXIPOL collaboration that comprehensively covers the MAXIPOL-specific details of actually computing the power spectrum of time ordered data correctly. Therefore, it is useful to form this document by compiling the collective knowledge of the collaboration into one concise record so the task of mining this information will not have to be repeated by future graduate students and postdocs.

I will assume the reader is familiar with both the IDL programming language and the text *Numerical Recipes in C*. These assumptions are fair for this discussion because IDL is the *de facto* programming standard in the collaboration today and copies of *Numerical Recipes in C* are commonly available. When it is useful, I will make reference to specific chapters and pages in *Numerical Recipes in C* or specific entries in the IDL documentation.

A.2 The FFT

At the heart of the power spectrum lies the FFT. IDL comes with an FFT function built in which is defined as

$$\widetilde{d}_k = \frac{1}{N}\sum_{t=0}^{N-1} d_t\, e^{-i2\pi kt/N} \tag{A.1}$$

$$d_t = \sum_{k=0}^{N-1} \widetilde{d}_k\, e^{i2\pi kt/N} \tag{A.2}$$

for the forward and reverse transform, respectively. Here d is the uniformly sampled time ordered data indexed by t, $\widetilde{d}$ is the FFT of d indexed by k and N is the total number of samples. The data vector in the time domain and its FFT will have the same number of elements; the time domain vector is real while the FFT is complex.

The FFT computation time is roughly proportional to N times the sum of the prime factors of N [38]. For example, if $N = 263$, the prime factors of N are 1 and 263 so the computation time is proportional to 263(1+263) = 69,432. If $N = 264$, the prime factors of N are 2, 2, 2, 3 and 11 so the computation time is proportional to 264(2+2+2+3+11) = 5,280. Notice the computation time for the **longer** 264 element array is 13.15 times **shorter** than the computation time for the 263 element array! In general, computing the FFT of arrays with a prime number of elements will require more computation time than other arrays with similar length. The number of elements in the time ordered data array must be considered when computing the power spectrum of long, MAXIPOL-like arrays because the computation time may become impractical (arrays can have over one million elements). If N = 1,048,583 (a prime number) one might choose to drop 7 samples so that N = 1,048,576 = 2^{20}. The computation time would be shorter by a factor of ∼26,000. In general, a good strategy is to make the data array have 2^x elements because the only prime factor of 2^x is 2 so the sum of the prime factors is $2x$, a relatively small number – even for large N. If making the data array have 2^x elements is too tedious, the next best strategy is to make the array have an even number of elements because prime numbers should be avoided and all prime numbers > 2 are odd numbers. The structure of the FFT array is different for N = even and N = odd. Since using an odd number of elements is so unfavorable, this discussion will assume that N will always be even. The storage scheme for $\widetilde{d}_k$ with N = even is illustrated in Figure A.1.

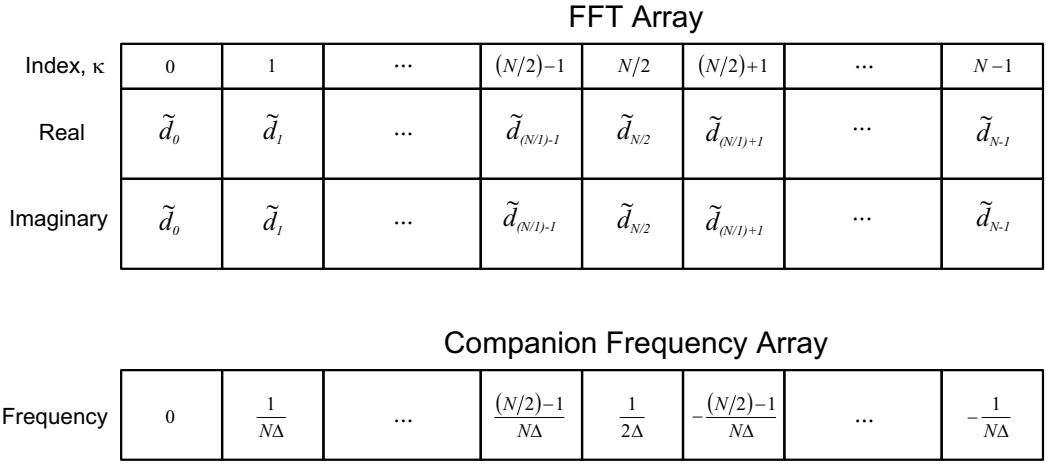

Figure A.1: The FFT storage scheme.

A.3 The Periodigram

The ultimate goal of this effort is to produce a periodigram estimate of the power spectrum between f=0 and f=$f_{Nyquist}$ which can be integrated to yield the mean squared amplitude of the time ordered data. The Nyquist frequency, $f_{Nyquist}$=$\frac{1}{2\Delta}$ where Δ is the sampling period. *Numerical Recipes in C* defines the periodigram estimate as

$$\begin{aligned} P_{k'=0} &= |\,\widetilde{d}_{k'=0}\,|^2 \\ P_{k'} &= [\,|\,\widetilde{d}_{k'}\,|^2 + |\,\widetilde{d}_{N-k'}\,|^2] \\ P_{k'=N/2} &= |\,\widetilde{d}_{k'=N/2}\,|^2 \end{aligned} \tag{A.3}$$

where $k' = 1, 2, ..., (\frac{N}{2} - 1)$ [39]. For clarity, the index k' runs from 0 to $\frac{N}{2}$ while k runs from 0 to N-1. From the storage scheme illustrated in Figure A.1 it is clear the $0th$ element of $P_{k'}$ corresponds to the frequency $f = 0$ and the $\frac{N}{2}th$ element corresponds to f=$f_{Nyquist}$.

A.4 Normalization

Truly, the central issue of this discussion is the power spectrum normalization. Again, the goal is to produce a power spectrum estimate that can be integrated to yield the mean squared amplitude

of the data. Expressed differently,

$$\Delta f \sum_{k'=0}^{N/2} \mathcal{P}_{k'} = \frac{1}{N} \sum_{t=0}^{N-1} |d_t|^2 \tag{A.4}$$

where $\mathcal{P}_{k'}$ is the power spectrum estimate we are searching for and $\Delta f = \frac{1}{N\Delta}$. Parseval's theorem states that

$$\frac{1}{N} \sum_{t=0}^{N-1} |d_t|^2 \quad = \quad \sum_{k=0}^{N-1} |\widetilde{d}_k|^2 \tag{A.5}$$

Equation A.3 is really just a different storage scheme for the squared modulus of $\widetilde{d}$ so

$$\sum_{k=0}^{N-1} |\widetilde{d}_k|^2 = \sum_{k'=0}^{N/2} P_{k'} \tag{A.6}$$

Combining EquationA.4, EquationA.5 and EquationA.6,

$$\Delta f \sum_{k'=0}^{N/2} \mathcal{P}_{k'} = \sum_{k'=0}^{N/2} P_{k'} \tag{A.7}$$

and

$$\mathcal{P}_{k'} = \frac{1}{\Delta f} P_{k'} \tag{A.8}$$

Example IDL Code

```
N = long(38400.)
delta_t = 4.8e-3 ; [sec]
delta_nu = 1./(double(N)*delta_t) ; [Hz]
f_nyquist = 1./(2.*delta_t) ; [Hz]
d = randomn(seed,N)

frequency = delta_nu*dindgen(N)
frequency[(N/2)+1:N-1] = (-1)*reverse(frequency[1:(N/2)-1])

d_tilde = fft(d,-1,double=1)
P = dblarr( (N/2)+1 )
P[0] = abs(d_tilde[0])^2
P[1:(N/2)-1] = abs(d_tilde[1:(N/2)-1])^2 +
```

```
                reverse( abs(d_tilde[(N/2)+1:N-1])^2 )
P[N/2] = abs(d_tilde[N/2])^2

P_script = sqrt(P/delta_nu)
f = frequency[0:N/2]
```

Appendix B

Noise Realization

To make meaningful simulations, often times it is necessary to include noise realizations with frequency domain properties that closely resemble the properties of the actual instrument noise. In general, the MAXIPOL detector noise can be described by the power spectrum

$$m_k = \sigma \left[1 + \left(\frac{f_{knee}}{f_k} \right)^{\alpha} \right] \tag{B.1}$$

for the frequencies

$$f_k = \frac{k}{N\,\Delta t} \qquad \text{where} \qquad k = 1, 2, \ldots, \frac{N}{2} \tag{B.2}$$

Here we have $1/f^{\alpha}$ and white noise with σ, the white noise level in $\mathrm{V}/\sqrt{\mathrm{Hz}}$, and f_{knee}, the frequency where the $1/f$ noise and the white noise are equivalent. N is the number of elements in the discretely sampled time ordered data and Δt is the sample period.

To create a noise realization that has the desired power spectrum, we build by hand its FFT in the frequency domain. For this prescription, we require that the number of samples, N, be an even number and we use the FFT storage scheme illustrated in Figure A.1.

$$\left.\begin{aligned} \mathrm{Re}\,(\widetilde{n}_k) &= \tfrac{\sqrt{\Delta f\, m_k^2}}{2}\, G_k^R \\ \mathrm{Im}\,(\widetilde{n}_k) &= \tfrac{\sqrt{\Delta f\, m_k^2}}{2}\, G_k^I \\ \widetilde{n}_{N-k} &= \widetilde{n}_k^* \end{aligned}\right\} \quad k = 1, 2, \ldots, \frac{N}{2} - 1 \tag{B.3}$$

Here, $\Delta f = \frac{1}{N\,\Delta t}$, while G_k^R, G_k^I and G are Gaussian random variables with standard deviation equal to 1. Now we set the $f = 0$ and $f = f_{Nyquist}$ elements individually. Notice they are real.

$$\widetilde{n}_{k=0} \;=\; \xi \tag{B.4}$$

$$\widetilde{n}_{k=N/2} \;=\; \frac{\sqrt{\Delta f}}{2}\,\sigma\,\left[1+\left(\frac{f_{knee}}{f_{Nyquist}}\right)^{\alpha}\right]\,G\,, \qquad f_{Nyquist} = \frac{1}{2\,\Delta t}$$

The DC offset, ξ, is typically chosen to be 0 though it can be arbitrarily set. Now the frequency domain FFT is complete. To generate the time domain noise realization we simply reverse FFT $\widetilde{n}_k$.

$$n_t = \mathrm{Re}\left(\sum_{k=0}^{N-1}\widetilde{d}_k\,e^{i2\pi kt/N}\right) \tag{B.5}$$

Sample IDL Code

```
;;;;;;;;;;;;;;;;;;;;;;;;;;;;;;;;;;;;;;;;;;;;;;;;;;;;;;;;;;;;;;;;;;;;;;;;;;;
;;;;;;;;;;;;;;;;;;;;;;;;;;;;;;;;;;;;;;;;;;;;;;;;;;;;;;;;;;;;;;;;;;;;;;;;;;;

function maxipol_noise, length

; AUTHOR: B. Johnson
; DATE: December 20, 2003
; This IDL code creates a simulated noise time stream composed
; of white noise and 1/f noise.  The white noise level, the 1/f
; knee and alpha are set to values that were realized by a
; typical channel in the MAXIPOL receiver.
; INPUT: length of time stream that will be created
; OUTPUT: vector containing a noise realization embracing the prescribed
; power spectrum.

; Define some necessary constants
length = long(length) ; length must be an even number
N = double(length)
delta_t = 4.8e-3 ; [sec] -- sample period
nyquist = 1./(2.*delta_t) ; [Hz] -- nyquist frequency
delta_nu = 1./(N*delta_t) ; [Hz] -- FFT frequency resolution
```

```
; Create a frequency array companion for the fft.
frequency = delta_nu*dindgen(length)
frequency[(length/2)+1:length-1] = (-1)*reverse(frequency[1:(length/2)-1])

; Define the noise model.
; NOTE: this is model of the noise power spectrum with familiar units.
white_noise = 10.e-9 ; [V/sqrt(Hz)]
fknee = 0.2 ; [Hz]
alpha = 1.4
dc_offset = 0.  ; [V]
model = white_noise*( 1.  + (fknee/frequency[1:(length/2)-1])âlpha )

; Create a complex array that will be populated with frequency domain noise.
fnoise = dcomplexarr(length)

; By hand create the real and imaginary parts of the fft array that
; will ultimately be reverse ffted to create the noise time stream.
; The delta_nu term converts the model into an array that is
; cosistent with Parseval's Theorem.  The sqrt(2) divides the power
; into the real and imaginary parts of the fft correctly.
real = sqrt(delta_nu*model2̂/2.)*randomn(seed,(length/2)-1)*(1./sqrt(2.))
imag = sqrt(delta_nu*model2̂/2.)*randomn(seed,(length/2)-1)*(1./sqrt(2.))

; Populate the fft array for both positive and negative frequencies.
; NOTE: real(fft[+f]) = real(fft[-f])
; imaginary(fft[+f]) = -imaginary(fft[-f])
fnoise[1:(length/2)-1] = dcomplex(real,imag)
fnoise[(length/2)+1:length-1] = dcomplex(reverse(real),(-1)*reverse(imag))

; Set the zero frequency and nyquist frequency elements of the fft by hand.
temp = (sqrt(delta_nu)*white_noise*(1.+(fknee/nyquist)âlpha))*$
randomn(seed,1)
fnoise[length/2] = dcomplex(temp,0.)
fnoise[0] = dcomplex(dc_offset,0.)

; Reverse fft the array and create the noise time stream.  Use only
; the real part of the reverse ffted array.
noise = double( fft(fnoise,1) )
```

```
return, noise

end

;;;;;;;;;;;;;;;;;;;;;;;;;;;;;;;;;;;;;;;;;;;;;;;;;;;;;;;;;;;;;;;;;;;;;;;;;;;
;;;;;;;;;;;;;;;;;;;;;;;;;;;;;;;;;;;;;;;;;;;;;;;;;;;;;;;;;;;;;;;;;;;;;;;;;;;
```

Appendix C

The MAXIPOL Collaboration

M. E. Abroe[1], P. Ade[3], J. Bock[4], J. Borrill[7,9], J. S. Collins[2], P. Ferreira[5], S. Hanany[1], A. H. Jaffe[8], B. R. Johnson[1], T. Jones[1], A. T. Lee[2,6], T. Matsumura[1], B. Rabii[2], T. Renbarger[1], P. L. Richards[2], G. F. Smoot[2,6], R. Stompor[7], H. T. Tran[2], C. D. Winant[2], J. H. P. Wu[10]

[1] *School of Physics and Astronomy, University of Minnesota, Minneapolis, MN, USA*

[2] *Department of Physics, University of California, Berkeley, CA, USA*

[3] *Department of Physics and Astronomy, University of Wales, Cardiff, UK*

[4] *Jet Propulsion Laboratory, Pasadena, CA, USA*

[5] *Astrophysics & Theoretical Physics, University of Oxford, Oxford, UK*

[6] *Physics Division, Lawrence Berkeley National Lab, Berkeley, CA, USA*

[7] *Computational Research Division, Lawrence Berkeley National Lab, Berkeley, CA, USA*

[8] *Astrophysics Group, Blackett Lab, Imperial College, London, UK*

[9] *Space Sciences Laboratory, University of California, Berkeley, CA, USA*

[10] *Department of Particle Physics, Weizmann Institute of Science, Rehovot, Israel*

[10] *Department of Physics, National Taiwan University, Taipei, Taiwan*

References

[1] Hu, W., & White, M. 1997. *New Astronomy.* 2, 323-344. astro-ph/9706147.

[2] Johnson, B. R., et al. 2003. *New Astronomy Reviews, "The Cosmic Microwave Background and its Polarization."* astro-ph/0308259.

[3] Hanany, S., et al. 2000. *ApJ.* 545:L5-L9.

[4] Lee, A. T., et al. 2001. *ApJ.* 561:L1-L5.

[5] Stompor, R., et al. 2001. *ApJ.* 561:L7-L10.

[6] Abroe, M. E., et al. 2004. *ApJ.* 605, 607-613.

[7] Benoit, A., et al. 2003. *Astronomy & Astrophysics.* 399, L19-L23.

[8] Hinshaw, G., et al. 2003. *ApJ Suppl.* 148, 135.

[9] This plot was prepared in collaboration with M. E. Abroe, Ph.D.

[10] Kovac, J.M., et al. 2002. *Nature.* 420, 772.

[11] Kogut, A., et al. 2003. *ApJ Suppl.* 148, 161.

[12] Knox, L., et al. 2002. *Phys. Rev. Lett.* 89, 011303.

[13] Wang, X., et al. 2002. *Phys. Rev. D.* 65, 123001.

[14] Seljak, U. & Hirata, C. M. 2004. *Phys. Rev. D.* 69, 043005.

[15] Hu, W., et al. 2003. *Phys. Rev. D.* 67, 043004. astro-ph/0210096.

[16] These models were computed using the publicly available CMBFAST software. *http://www.cmbfast.org*

[17] Lee, A. T., et al. 1998. *The Proceedings of the "3 K Cosmology" Conference*, ed. F. Melchiorri. astro-ph/9903249.

[18] Rabii, B., Winant, C. D., et al. 2003. *ApJ submitted.* astro-ph/0309414.

[19] Winant, C. D. 2003. Ph.D. Thesis. University of California, Berkeley.

[20] Rabii, B. 2002. Ph.D. Thesis. University of California, Berkeley.

[21] Shurcliff, W. A. 1962. *Polarized Light: Production and Use.*

[22] Collet, E. 1992. *Polarized Light: Fundamentals and Applications*

[23] Peterson, J. B. & Richards, P. L. 1984. *Int. J. Infrared Millimeterwaves*, vol. 5, no. 12, pp. 1507-1515.

[24] Hagmann C. & Richards, P.L. 1995. Cryogenics, vol. 35, no. 5, pp. 303-309.

[25] Bock, J. J. 1994. Ph.D. Thesis. University of California, Berkeley.

[26] Jaffe, A. H., et al. 1999. Invited review in *"Microwave Foregrounds"*, eds. A. de Oliveira-Costa & M. Tegmark. ASP, San Francisco. astro-ph/9903248.

[27] Hanany, S., et al. 2003. *New Astronomy Reviews, "The Cosmic Microwave Background and its Polarization."* astro-ph/0307052.

[28] Hanany, S., et al. 2002. *IEEE Transactions of Applied Superconductivity.* Vol. 13. astro-ph/0304312.

[29] Afsar, M. N. & Chi, H. 1991. *16th International Conference on Infrared and Millimeter Waves, Conference Digest, SPIE publication, Vol.1576, ISBN 0-8194-0707-0, M. R. Siegrist, M. Q. Tran and T. M. Tran, Lausanne, Switzerland, Aug 26-30, 1991*

[30] Afsar, M. N. 1987. *IEEE Transactions on Instrumentation and Measurement.* Vol. IM-36. No. 2.

[31] Lowenstein, E. V., Smith, D. R., & Morgan, R. L. 1973. *Applied Optics.* Vol. 12. No. 2.

[32] Hecht, E. 1997. *Optics 3rd Edition.*

[33] Hinshaw, G., et al. 2003. *ApJS.* 148, 63.

[34] Collins, J. S. 2005 expected. Ph.D. Thesis. University of California, Berkeley.

[35] Lowdermilk, W. H. & Milam, D. 1980. *Appl. Phys. Lett.* 36, 11.

[36] Southwell, W. H. 1983. *Optics Letters.* Vol.8, No.11, p.584.

[37] These maps were genertaed by Proty Wu using an FFT algorithm.

[38] IDL version 5.6 help entry for FFT function.

[39] *Numerical Recipes in C, Second Edition.* Section 13.4, equation (13.4.5).